Doping and Ion Substitution in Colloidal Metal Halide Perovskite Nanocrystals

Journal:	*Chemical Society Reviews*
Manuscript ID	CS-SYN-11-2019-000790.R3
Article Type:	Review Article
Date Submitted by the Author:	30-May-2020
Complete List of Authors:	Lu, Cheng-Hsin; Georgia Institute of Technology, School of Materials Science and Engineering Biesold-Mcgee, Gill; Georgia Institute of Technology, Materials Science and Engineering Liu, Yijiang; Institute of Chemistry Chinese Academy of Sciences, State Key Laboratory of Polymer Physics and Chemistry; Xiangtan University, College of Chemistry Kang, Zhitao; Georgia Institute of Technology, Lin, Zhiqun; Georgia Institute of Technology, Materials Science and Engineering

Doping and Ion Substitution in Colloidal Metal Halide Perovskite Nanocrystals

Cheng-Hsin Lu [a], *Gill Biesold-McGee* [a], *Yijiang Liu* [b*], *Zhitao Kang* [a,c], *Zhiqun Lin* [a,*]

[a] *School of Materials Science and Engineering, Georgia Institute of Technology, Atlanta, GA 30332, USA*

[b] *College of Chemistry, Xiangtan University, Xiangtan, Hunan Province, 411105, PR China*

[c] *Georgia Tech Research Institute, Georgia Institute of Technology, Atlanta, GA 30332, USA*

* Corresponding Authors: liuyijiang84@xtu.edu.cn and zhiqun.lin@mse.gatech.edu

Abstract

The past decade has witnessed tremendous advances in synthesis of metal halide perovskites and their use for a rich variety of optoelectornics applications. Metal halide perovskite has the general formula ABX_3, where A is a monovalent cation (which can be either organic (e.g., $CH_3NH_3^+$ (MA), $CH(NH_2)_2^+$ (FA)) or inorganic (e.g., Cs^+)), B is a divalent metal cation (usually Pb^{2+}), and X is a halogen anion (Cl^-, Br^-, I^-). Particularly, the photoluminescence (PL) properties of metal halide perovskites have garnered much attention due to the recent rapid development of perovskite nanocrystals. The introduction of capping ligands enables the synthesis of colloidal perovskite nanocrystals which offer new insight into dimension-dependent physical properties compared to their bulk counterparts. It is notable that doping and ion substitution represent effective strategies for tailoring the optoelectronic properties (e.g., absorption band gap, PL emission, and quantum yield (QY)) and stabilities of perovskite nanocrystals. The doping and ion substitution processes can be performed during or after the synthesis of colloidal nanocrystals by incorporating new A', B', or X' site ions to the A, B, or X sites of ABX_3 perovskites. Interestingly, both isovalent and heterovalent doping and ion substitution can be conducted on colloidal perovskite nanocrystals. In this review, the general background of perovskite nanocrystals synthesis is first introduced. The effects of A-site, B-site, and X-site ionic doping and substitution on the optoelectronic properties and stabilities of colloidal metal halide perovskite nanocrystals are then detailed. Finally, possible applications and future research directions of doped and ion-substituted colloidal perovskite nanocrystals are also discussed.

1. Introduction

Metal halide perovskites are materials with the general structure ABX_3, where A is a monovalent cation (which can be either organic (e.g., $CH_3NH_3^+$ (MA), $CH(NH_2)_2^+$ (FA)) or inorganic (e.g., Cs^+)), B is a divalent metal cation (usually Pb^{2+}), and X is a halogen anion (Cl^-, Br^-, I^-). The divalent metal B is surrounded by six halogen atoms forming a BX_6 octahedral structure while the A cation is located in the cubo-octahedral cavity within the corner-shared BX_6 octahedral framework forming a three-dimensional (3D) structure (Figure 1). In recent years, metal halide perovskites have attracted great research interest due to their cost-effective solution processability and remarkable performance in optoelectronic applications. The utilization of capping ligands such as oleic acid (OA) and oleylamine (OLA) during colloidal synthesis allows for the creation of perovskite nanocrystals. Demonstrated morphologies of perovskite nanocrystals include nanocubes, nanowires, nanoplatelets, nanoparticles, etc. [1-4] Perovskite nanocrystals possess a higher surface-area-to-volume ratio than their bulk counterparts. [12] Additionally, nanocrystals may exhibit different optoelectronic responses than their bulk form due to quantum confinement and strong anisotropic effects. [5, 6] Perovskite nanocrystals have demonstrated a promising future in many optoelectronic applications and have been applied in photovoltaic cells, [7-10] photodetectors, [11-18] lasers, [19-25] light-emitting diodes (LEDs), [26-45] and many other applications.

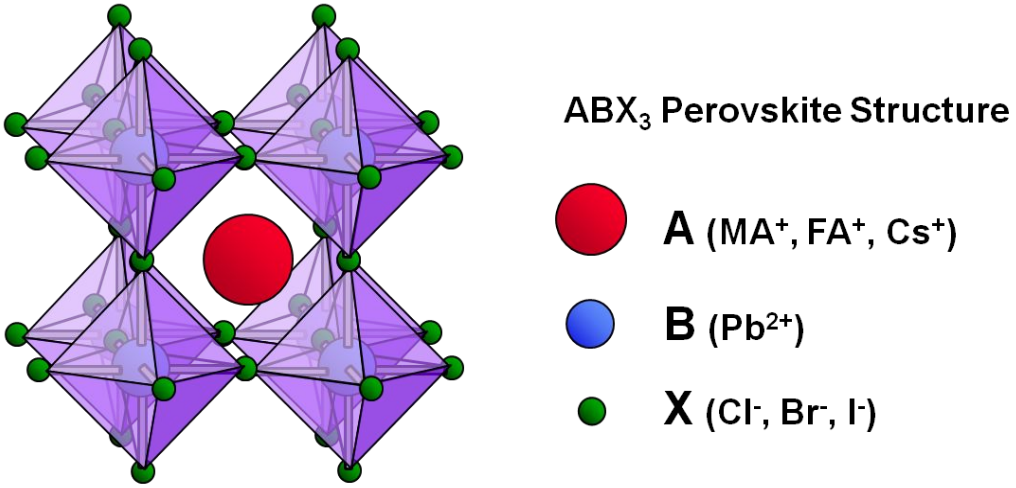

Figure 1. Schematic of perovskite ABX_3 structure, where the A cation (red ball) can be either an organic cation (e.g., $CH_3NH_3^+$ (MA), $CH(NH_2)_2^+$ (FA), etc.) or an inorganic alkali metal (e.g., Cs^+), the B cation (blue ball) is usually Pb^{2+}, and the X anion (green ball) is a halogen ion (i.e., Cl^-, Br^-, I^- or mixture thereof). The A cation is located in the cubo-octahedral cavity within the corner-shared BX_6 octahedral framework, forming a three-dimensional (3D) structure.

1-1. Colloidal Perovskite Nanocrystals

Although all-inorganic and organic-inorganic hybrid perovskites have been synthesized and studied for several decades, [46, 47] their optoelectronic potential was first explored only a decade ago. In their seminal work, Kojima *et al.* incorporated $CH_3NH_3PbBr_3$ ($MAPbBr_3$) into a sensitized solar cell and obtained an energy conversion efficiency of ~2.2%. [48] Since then, the solar conversion efficiency of perovskite solar cells has improved more than 10 times to >25% and is comparable to Si-based solar cells. [49] The tremendous photovoltaic efficiency of metal halide perovskites can be attributed to their unique optoelectronic properties: long carrier diffusion lengths, [50, 51] high charge carrier mobilities, [52] long-range balanced electron and hole transport, [53] low trap-state density, [54] multiphoton high absorption coefficients, [55-58] and direct and tunable band gaps. [5] Colloidal $MAPbBr_3$ nanocrystals were first synthesized in 2014 and have demonstrated excellent photoluminescence (PL) emission properties. [59-61] Perovskite nanocrystals possess many unique advantages over legacy light emitters such as solution processability, bright luminescence (the photoluminescence quantum yield (PLQY) can reach ~100%), [61, 62] narrow emission bandwidth (the full width at half maximum (FWHM) can be as low as below 15 nm), [5] and tunable emission spectra over the entire visible region (from roughly 400 nm all the way to around 750 nm). [63] The applications of metal halide perovskite nanocrystals extend beyond those mentioned above into many other uses such as: (1) serving as an intermediate layer to tune band gap alignment in photovoltaic cells, [64, 65] (2) filling pinholes and cracks in perovskite film photodetectors through recyclable dissolution–recrystallization (RDR), [66] (3) boosting power conversion efficiency (PCE) of solar cells by down-converting UV to harvestable visible light, [67] (4) tailoring lighting displays to the desired color temperature by down converting a blue chip LED source, [68-71] (5) probing for 2,4,6-trinitrophenol (TNP, picric acid), tetraoctylammonium halide salts (TOAX), or gaseous HCl by monitoring PL or colorimetric responses, [72-74] (6) serving as X-ray photon detection scintillators by converting X-ray irradiation and radioluminescence into visible wavelengths, [75] (7) generating hydrogen (H_2) via photocatalytic hydrohalic acid (HX) splitting, [76] (8) reducing CO_2 via photocatalysis with or without the assistance of another carrier transportation material for electron-extraction, [77-83] (9) preventing fraud by serving as fluorescent inks for anti-counterfeit or encryption printing purposes, [84-86] (10) serving as luminescence probes for bioimaging applications, [87-94] and many others.

1-2. Syntheses and Morphologies

Colloidal metal halide perovskite nanocrystals can be synthesized using several different methods. The hot injection method, adapted from the method commonly used in the synthesis of traditional II–VI, III–V, and IV-VI semiconductor quantum dots, is the first method introduced to synthesize perovskite nanocrystals which is performed at an elevated temperature. [95] Low temperature (or room temperature) synthesis methods include the ligand-assisted reprecipitation (LARP) method and supersaturated recrystallization (SR) method. [95] Hot-injection, LARP, and SR methods can all be used to synthesize both all-inorganic and organic-inorganic hybrid perovskite nanocrystals. [59-61] Hot-injection method usually involves the use of high-boiling point non-coordinating solvent such as octadecene (ODE), while low temperature synthesis methods usually employ both a polar solvent (with high solubility for ionic perovskite precursors, e.g., N,N-dimethylformamide (DMF) or dimethyl sulfoxide (DMSO)) and non-polar solvent (with poor solubility for ionic perovskite precursors, e.g., toluene or hexane). [96] In both high and low temperature methods capping ligands are needed to stabilize the reaction, with the acid-base pair of oleic acid (OA) and oleylamine (OLA) being among the most commonly used. Polymer micelles, [90, 97, 98] surfactant emulsions, [30] star-like copolymers, [99, 100] and microporous metal−organic frameworks (MOFs) [81, 101, 102] are examples of some additional capping ligands or templates that have been used for colloidal metal halide perovskite nanocrystal synthesis. Alternative wet-synthesis processes for perovskite nanocrystal synthesis include microwave irradiation, [103-105] ultrasonication, [17, 45, 106-112] dilution, [113] and solvothermal synthesis. [114]

The nucleation and growth mechanisms of $MAPbX_3$ nanocrystals created using the LARP method have been proposed, [115] and the formation mechanisms of $CsPbBr_3$ nanocrystals have been studied via a slowed-down microwave-assisted synthesis. [103] Systematic study of formation mechanisms of mixed halide perovskites has been achieved by a droplet-based microfluidic platform. [116] Gram-scale mass production of $CsPbX_3$ nanocrystals has been achieved by both a microwave irradiation process, [104] and by mixing Cs-oleate and Pb-oleate with tetraoctylammonium halide in toluene at room temperature. [117] In addition to the wet-synthesis processes mentioned above, some dry mechanosynthesis processes such as grinding or milling have been used to synthesize perovskite nanocrystals. After physically mixing precursors by grinding or milling, they can be dissolved in solvent with ligands to form colloidal nanocrystals, or in some cases the mixture of precursors will become bulk crystals in powder form without the addition of solvent or capping ligands. Luminescent $MAPbX_3$, [108, 118] $MASnBr_3$, [119] $CsPbX_3$, [120, 121] Mn-doped $CsPbX_3$, [122] and $Cs(AgBi)_{x/2}Pb_{1-x}Br_3$ [123] colloidal nanocrystals or powders have been made using grinding or milling methods.

The diverse dimensionality of perovskites adds an additional degree of freedom for tuning material properties. A multitude of diverse morphologies of metal halide perovskite nanocrystals can be created by fine tuning the synthesis conditions such as: temperature, reaction time, amount or type of the capping ligands, and injection speed of the precursors. Some examples for the various morphologies of the colloidal metal halide perovskite nanocrystals that have been successfully synthesized are 3D nanocubes, [1, 2, 110, 114, 124] two-dimensional (2D) nanoplates, [1-4, 27, 104, 110, 124-127] 2D nanosheets, [3, 128, 129] one-dimensional (1D) nanowires, [1, 4, 104, 110, 111, 114, 130-134] 1D nanorods, [1, 2, 104, 135] and zero-dimensional (0D) nanodots. [1-4, 96, 110, 136, 137] Hexagonal or irregular shape nanocrystals have also been achieved, [104, 138] but it is possible that these hexagonal or irregular shape nanocrystals are a lead-poor phase (e.g.,

Cs_4PbBr_6 phase compared to $CsPbBr_3$ phase), because the ratio of acid-base ligand pair will affect the solubility of lead halide salts. [109, 139]

1-3. Defect Tolerance

Unlike conventional II–VI, III–V, and IV-VI semiconductor quantum dots, lead halide perovskite nanocrystals are defect-tolerant and do not suffer similar quenched emission from surface defect states. The defect tolerance in both $CsPbX_3$ and $MAPbX_3$ nanocrystals can be attributed to the unique electronic band structure configuration of the bonding-antibonding interaction within their conduction bands and valence bands. [140, 141] In conventional semiconductors, the valence band (VB) and conduction band (CB) are predominantly composed of bonding (σ) and antibonding (σ*) orbitals, respectively. In lead halide perovskites, the valence band maximum (VBM) is antibonding (σ*) in nature and conduction band minimum (CBM) is stabilized by the spin−orbit splitting of Pb(6p) states (Figure 2). [142] Schematics of the two limiting cases of semiconductor band structure are in Figure 2a: (left) conventional defect-intolerant band structure, and (right) ideal hypothetical defect-tolerant band structure. Schematic of lead halide perovskite is shown in Figure 2b using $APbI_3$ (A=Cs or MA) as an example: (1) the valence band maximum (VBM) is exhibiting antibonding characters originating from the hybridization of Pb(6s) and I(5p) orbitals, which meets the optimal bonding character of defect tolerance as depicted in Figure 2a, while (2) the conduction band minimum (CBM) is mainly composed of antibonding orbitals contributed from Pb(6p) (rather than Pb(6p)−I(5p) interactions) and does not seem to meet the optimal bonding character of defect-tolerant case. Strong spin−orbit coupling (SOC) effects result in energy level splitting, which leads to a beneficial band broadening that shifts the bottom of the conduction band below the Pb(6p) atomic orbital and increases the chance that defects form as intra-conduction band states. [143] Density functional theory (DFT) calculation has demonstrated that both bulk or surface perovskites show no in-gap defect states between the VBM and CBM, [144] and that removing some of the surface atoms and/or capping molecules (creating dangling bonds) does not introduce localized trap states within the band gap. [145] Defects such as vacancies, interstitial atoms, and surface states will not likely form intra-gap states but rather appear as resonances inside shallow transition levels. Because of this, the surface passivation commonly used in conventional quantum dot synthesis is not strictly required in lead halide perovskites. [143] Because of their defect-tolerant nature, high PLQY lead halide perovskite nanocrystals do not require the same high purity, high temperature, or equipment-intensive vacuum synthesis as conventional semiconductor materials, which make them more easily scalable for mass production. [141] Exploration of other materials with similar defect tolerance electronic band structure is a promising direction, with I−III−VI compound semiconductors and Cu_3N being prime examples. [142] It is worth noting that A-site cations do not directly affect the bandgap because they form bonding states deep in the VBM and do not hybridize with PbI_6 octahedra near VBM or CBM. [146] The A-site cations do, however, indirectly change the bandgap because their size determines both the structural stability and the expansion or contraction of the perovskite lattice, both of which alter band structure. [142]

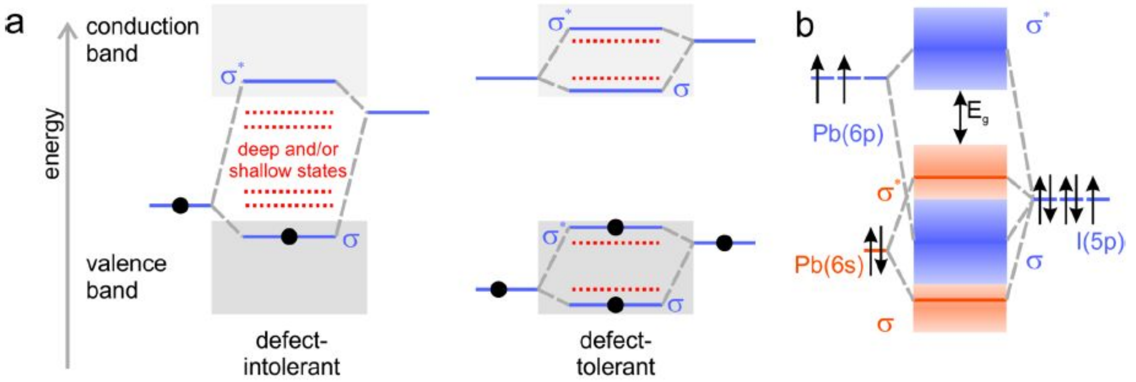

Figure 2. (a) Schematics of two limiting cases of band structure in semiconductors: (left) conventional defect-intolerant band structure and (right) ideal hypothetical defect-tolerant band structure. Bonding and antibonding orbitals are denoted as σ and σ*, respectively. (b) Schematic of simplified bonding and band structure in $APbI_3$ perovskite. The valence band maximum (VBM) exhibits a desired antibonding character similar to the ideal defect-tolerant case shown in (a). Reprinted with permission from Ref. [143], copyright 2016, American Chemistry Society.

1-4. Tolerance Factor and Octahedral Factor

Not all combinations of A^{1+}, B^{2+}, and X^{1-} can form the complex ABX_3 halide perovskite structure. Tolerance factor (*t*), a rule proposed by Goldschmidt in the early 1920s, is used to understand and quantify what combination of chemical species can form perovskite structure.[147]

$$t = \frac{(R_A + R_X)}{\sqrt{2}(R_B + R_X)} \qquad (1)$$

R_A, R_B and R_X are the ionic radii for the ions in the A, B and X sites of ABX_3 perovskites, respectively. A *t* value close to unity ($t \approx 1$) indicates a perfect fit and thus successful perovskite formation. The tolerance factor (*t*) can be used to determine whether the A site cations can fit in the cavities within the BX_6 framework. Differing from their oxide perovskite counterparts ($A^{2+}B^{4+}O^{2-}{}_3$), metal halide perovskite ($A^{1+}B^{2+}X^{1-}{}_3$) has a limited choice of cations because: (1) the relatively smaller negative charge of halides (1- vs. 2-) is only able to compensate A-site and B-site cations with lower oxidation states, and (2) the ionic radii of halides are larger than oxides, which requires larger B-site metal ions to maintain octahedral coordination geometry. [148] For lead halide perovskites, the tolerance factor ranges from $0.81 < t < 1.11$. [149] If *t* lies outside this range, 3D perovskite structure will not be formed and instead polymorphs of corner-sharing BX_6 octahedra with a lower dimensional connectivity such as 2D layers, 1D chains, or 0D BX_6 octahedral clusters will appear. [150-152]. These lower-dimensional lead halide compounds usually possess much larger band gaps and are not suitable for photovoltaic applications. [153] In addition to tolerance factor (*t*), the octahedral factor (μ) is also used to indicate perovskite stability,

$$\mu = \frac{R_B}{R_X} \qquad (2)$$

where μ is defined as the ratio of the ionic radii of the species occupying the B-site to X-site. For lead halide perovskites, the range for the octahedral factor is $0.44 < \mu < 0.90$. [149] Both the tolerance factor and the octahedral factor are necessary but not sufficient conditions for the formation of stable ABX_3 3D perovskites. [154]

Selecting species that fit the criteria listed above for ABX_3 perovskite can be challenging. For the A site, cesium (Cs^+) is the only monovalent metal with a sufficiently large ionic size (R_A of 1.88 Å) to sustain the lead halide perovskite structure, while Li^+, Na^+, K^+, Rb^+ cations all result in a tolerance factor smaller than 0.8. [155, 156] Two other monovalent organic molecular cations are known to fit in the 3D PbX_6 framework, and they are methylammonium (MA, $CH_3NH_3^+$) and formamidinium (FA, $CH(NH_2)_2^+$) with ionic radii (R_A) of 2.17 Å and 2.53 Å, respectively. [151, 157] It appears that for organic cations, both the size and distribution of the net positive charge are important. This helps explain why MA and FA can stabilize 3D lead halide perovskite structures and other monovalent organic cations with similar size (see effective ionic radii (R_A) in Table 1) cannot. [148] A wider range of divalent metal cations are candidates for the B-site (such as alkaline metals, transition metals, and lanthanides), but the use of many of them leads to limited ability to form 3D perovskite structures or band gaps too large for photovoltaic applications. [157] The most logical candidates to replace Pb^{2+} in the B site are the other group-14 elements, Ge^{2+} and Sn^{2+} (the effective radii (R_B) for Ge^{2+}, Sn^{2+}, and Pb^{2+} are 0.73 Å, 1.15 Å, and 1.19 Å, respectively), because they have a similar electronic configuration to Pb^{2+}. Unfortunately, Sn^{2+} and Ge^{2+} are not stable and oxidize to Sn^{4+} and Ge^{4+} easily. [157, 158] For X-site anions, the effective radii of halide anions (R_X) are 1.81 Å, 1.96 Å, and 2.20 Å for chloride (Cl^-), bromide (Br^-), and iodide (I^-), respectively. [151]

Table 1. The effective ionic radii of organic molecular cations and Shannon ionic radii (i.e., considering the respective coordination) of inorganic cations as well as the effective ionic radii of various anions.

A-Site Cation: Ionic Radius (R_A)	
Ammonium (NH_4^+):1.46 Å[a] Hydroxylammonium (NH3OH$^+$): 2.16 Å[a] Methylammonium ($CH_3NH_3^+$) 2.17 Å[a] Hydrazinium ($NH_3NH_2^+$): 2.17 Å[a] Azetidinium ($(CH_2)_3NH_2^+$): 2.50 Å[a] Formamidinium ($CH(NH_2)_2^+$): 2.53Å[a] Imidazolium ($C_3N_2H_5^+$): 2.58 Å[a] 3-Pyrrolinium ($NC_4H_8^+$): 2.72 Å[a];	Guanidinium ($(NH_2)_3C^+$): 2.78 Å[a] Tetramethylammonium ($(CH_3)_4N^+$): 2.92 Å[a] Thiazolium ($C_3H_4NS^+$): 3.20 Å[a] Tropylium ($C_7H_7^+$): 3.33 Å[a] Piperazinium ($C_4H_{12}N_2^{2+}$): 3.22 Å[b] Dabconium ($C_6H_{14}N_2^{2+}$): 3.39 Å[b] K^+: 1.64 Å[b]

<table>
<tr><td colspan="2">Dimethylammonium ($(CH_3)_2NH_2^+$): 2.72 Å[a]
Ethylammonium ($CH_3CH_2NH_3^+$): 2.74 Å[a]</td><td colspan="2">Rb^+: 1.72 Å[b]
Cs^+: 1.88 Å[b]</td></tr>
<tr><td colspan="4">B-Site Cation: Ionic Radius (R_B)</td></tr>
<tr><td>Be^{2+}: 0.45 Å[a]</td><td>Pd^{2+}: 0.86 Å[a]</td><td>Dy^{2+}: 1.07 Å[c]</td><td>Ce^{3+}: 1.01 Å[b]</td></tr>
<tr><td>Mg^{2+}: 0.72 Å[a]</td><td>Pt^{2+}: 0.80 Å[a]</td><td>Tm^{2+}: 1.03 Å[a]</td><td>Pr^{3+}: 0.99 Å[b]</td></tr>
<tr><td>Ca^{2+}: 1.00 Å[a]</td><td>Cu^{2+}: 0.73 Å[a]</td><td>Yb^{2+}: 1.02 Å[a]</td><td>Nd^{3+}: 0.98 Å[b]</td></tr>
<tr><td>Sr^{2+}: 1.18 Å[a]</td><td>Ag^{2+}: 0.94 Å[d]</td><td>Np^{2+}: 1.10 Å[d]</td><td>Sm^{3+}: 0.96 Å[b]</td></tr>
<tr><td>Ba^{2+}: 1.35 Å[a]</td><td>Zn^{2+}: 0.74 Å[a]</td><td>Tl^+: 1.50 Å[b]</td><td>Eu^{3+}: 0.95 Å[b]</td></tr>
<tr><td>Ti^{2+}: 0.86 Å[c]</td><td>Cd^{2+}: 0.95 Å[a]</td><td>Cu^+: 0.77 Å[d]</td><td>Gd^{3+}: 0.94 Å[b]</td></tr>
<tr><td>V^{2+}: 0.79 Å[c]</td><td>Hg^{2+}: 1.02 Å[a]</td><td>Ag^+: 1.15 Å[d]</td><td>Dy^{3+}: 0.91 Å[b]</td></tr>
<tr><td>Cr^{2+}: 0.80 Å[c]</td><td>Ge^{2+}: 0.73 Å[a]</td><td>Au^+: 1.37 Å[b]</td><td>Er^{3+}: 0.89 Å[b]</td></tr>
<tr><td>Mn^{2+}: 0.83 Å[a]</td><td>Sn^{2+}: 1.15 Å[a]</td><td>Au^{3+}: 0.85 Å[b]</td><td>Tm^{3+}: 0.88 Å[b]</td></tr>
<tr><td>Fe^{2+}: 0.78 Å[a]</td><td>Pb^{2+}: 1.19 Å[a]</td><td>Sb^{3+}: 0.76 Å[b]</td><td>Lu^{3+}: 0.86 Å[b]</td></tr>
<tr><td>Co^{2+}: 0.75 Å[a]</td><td>Sm^{2+}: 1.22 Å[c]</td><td>Bi^{3+}: 1.03 Å[b]</td><td>Pu^{3+}: 1.00 Å[b]</td></tr>
<tr><td>Ni^{2+}: 0.69 Å[a]</td><td>Eu^{2+}: 1.17 Å[a]</td><td>La^{3+}: 1.03 Å[b]</td><td></td></tr>
<tr><td colspan="4">X-Site Anion: Ionic Radius (R_X)</td></tr>
<tr><td colspan="2">Fluoride (F^-): 1.29 Å[b]
Chloride (Cl^-): 1.81 Å[b]
Bromide (Br^-): 1.96 Å[b]</td><td colspan="2">Iodide (I^-): 2.20 Å[b]
Formate ($HCOO^-$): 1.36 Å[b]
Thiocyanate (SCN^-): 2.17 Å[e]</td></tr>
</table>

* Effective ionic radius values are obtained from reference [a] [159] [b] [157] [c] [160] [d] [161] [e] [162].

1-5. Challenges and Overview

Different properties can be achieved by substituting ions in either the A-site, B-site, or X-site. Generally, A-site substitution can improve the overall stability by tuning the tolerance factor. B-site substitution can reduce the toxic Pb content and improve phase stability by altering the B-X bond length. X-site substitution can tune the band gap via changing the ratio of mixed-halide ions. It is worth noting that these simplified generalities do not fully capture all the effects that substituting ions in A-, B-, and X-sites can have on the final products. For example, substituting in any site of ABX_3 metal halide perovskites could alter its band gap (Table 2), yet only X-site substitution shows a clear trend in band gap tailoring.

Table 2. Summary of the tolerance factor (t) and band gap (Eg) values of ABX_3 metal halide perovskites with A-, B-, or X-site substitution. The t values are calculated based on the effective radii obtained from **Table 1**.

ABX_3	Tolerance factor	Band gap (eV)	ABX_3	Tolerance factor	Band gap (eV)	ABX_3	Tolerance factor	Band gap (eV)
$CsPbCl_3$	t=0.87	Eg=2.7[a]	$CsSnCl_3$	t=0.88	Eg=2.8[b]	$CsGeCl_3$	t=1.03	Eg=3.6[b]
$MAPbCl_3$	t=0.94	Eg=2.9[a]	$MASnCl_3$	t=0.95	Eg=2.8[c]	$MAGeCl_3$	t=1.11	Eg=3.7[b]
$FAPbCl_3$	t=1.02	Eg=3.0[a]	$FASnCl_3$	t=1.04		$FAGeCl_3$	t=1.21	
$CsPbBr_3$	t=0.86	Eg=2.4[a]	$CsSnBr_3$	t=0.87	Eg=1.8[b]	$CsGeBr_3$	t=1.01	Eg=2.4[b]
$MAPbBr_3$	t=0.93	Eg=2.3[a]	$MASnBr_3$	t=0.94	Eg=2.0[c]	$MAGeBr_3$	t=1.09	Eg=2.8[b]
$FAPbBr_3$	t=1.01	Eg=2.2[a]	$FASnBr_3$	t=1.02		$FAGeBr_3$	t=1.18	
$CsPbI_3$	t=0.85	Eg=1.8[a]	$CsSnI_3$	t=0.86	Eg=1.3[c]	$CsGeI_3$	t=0.98	Eg=1.6[d]
$MAPbI_3$	t=0.91	Eg=1.5[a]	$MASnI_3$	t=0.92	Eg=1.2[c]	$MAGeI_3$	t=1.05	Eg=1.9[d]
$FAPbI_3$	t=0.99	Eg=1.4[a]	$FASnI_3$	t=1.00	Eg=1.4[c]	$FAGeI_3$	t=1.14	Eg=2.2[d]

* Band gap (Eg) values are obtained from reference [a] [163] [b] [157] [c] [164] [d] [151].

Initial studies suggest that metal halide perovskite nanocrystals carry a promising future in many applications, yet substantial obstacles such as lead toxicity, hysteresis, and long-term stability may prevent them from successful commercialization. Notably, composition engineering has shown to be an effective route to overcoming many of those issues. By doping and substituting different ions into perovskites, their overall performance can be markedly improved by optimizing band alignment and emission range, [165] increasing stability, improving film morphology, enhancing charge carrier transport, minimizing hysteresis, and reducing toxic lead content. [146] For example, fully or partially replacing methylammonium (MA, $CH_3NH_3^+$) with formamidinium (FA, $CH(NH_2)_2^+$) in $MAPbI_3$ perovskite thin film solar cell devices results in a smaller band gap, longer exciton lifetime, superior thermal stability, and reduced hysteresis. [166-168] Nonetheless, composition engineering has its own limitation as partially substituting MA with FA increases the crystallization temperature of $MAPbI_3$ perovskite, leading to phase separation or unwanted non-perovskite yellow δ-phase. [168, 169] A few recent reviews have discussed the importance of composition engineering in metal halide perovskite nanocrystals. [170-174] Yet, an in-depth summary of both theoretical background and experimental guidelines on doping and ion substitution for crafting perovskite nanocrystals with outstanding optoelectronic properties and stabilities is still lacking. In this context, mixed-cation or mixed-anion colloidal metal halide perovskite nanocrystals achieved via doping or ion substitution is the primary focus of this review. This review will discuss relevant topics in the following order: general background of perovskite nanocrystals (Chapter 1), recent studies on doping and ion substitution in A-site (Chapter 2), B-site (Chapter 3), and X-site (Chapter 4), and applications (Chapter 5) and outlook (Chapter 6) of mixed-cation/mixed-anion colloidal metal halide perovskite nanocrystals. It is notable that this review will concentrate primarily on ABX_3 type 3D perovskites. Other perovskites such as $A_2B'B''X_6$, $A_3B_2X_9$, or Ruddlesden−Popper type low-dimensional perovskites will only be briefly discussed. [175-183]

2. A-Site Substitution

At room temperature, $MAPbX_3$ and $FAPbX_3$ usually exhibit cubic structure and $CsPbX_3$ usually has orthorhombic structure. The difference in structure is due to the fact that the Cs^+ ion is relatively smaller which leads to octahedral tilting/distortion and thus less symmetry leading to orthorhombic structure. [150] Due to the relatively small A-site cation, all inorganic $CsPbX_3$ perovskite nanocrystals have a relatively small tolerance factor (t) (Table 2). By changing the relatively small Cs^+ ion to larger A-site cations, the tolerance factor can be raised closer to 1. If the substituted A-site cations are too large for the PbX_6 octahedral framework, the Ruddlesden−Popper type layered perovskite structures may form. [158, 184] For traditional lead halide perovskite, FA is the relatively largest usable A-site cation and can achieve a tolerance factor (t) closer to 1 than MA and Cs cations. Compared to $MAPbI_3$, $FAPbI_3$ has shown superior solar cell performance due to red-shifted absorption (reduced band gap) and better charge transport. First-principles calculations demonstrate that the advantages of FA result from structure-induced enhancement of spin-orbit coupling (SOC). [185] The size of cations is not the only factor that determines crystal structure, as demonstrated by the fact that $MAPbI_3$ is tetragonal and $FAPbI_3$ is trigonal/pseudocubic even though the size of MA (R_A=2.17 Å) and FA (R_A=2.53 Å) are not that different. This difference can be explained by the fact that FA is more likely to form hydrogen bonds than MA, thereby stabilizing the pseudocubic structure. [185] The interaction between organic cations and the inorganic PbX_6 octahedra matrix mainly takes place through weak electrostatic interactions, but by careful cation design, it is possible to enhance the stability of perovskite by triggering stronger electronic coupling and electrostatic interactions like hydrogen-bonding, halogen-bonding, and Van der Waals interaction. [186]

$FAPbX_3$ colloidal nanocrystals with emission spanning the whole visible range have been successfully synthesized using both hot-injection method [187-189] and room temperature LARP method. [190, 191] Both hot-injection and room temperature synthesis methods can obtain $FAPbBr_3$ colloidal nanocrystals with similar optical properties (i.e., emission peak at ~530 nm, PLQY>85%, and FWHM<22 nm), but some mixed-halide $FAPbX_3$ colloidal nanocrystals are not single phase. Phase segregation has been widely observed in mixed-halide perovskite systems including $FAPbX_3$, [188] $MAPbX_3$, [192] and $CsPbX_3$ [193, 194]. An automated droplet-based microfluidic platform was used to show that phase segregation occurred in $FAPb(Cl/Br)_3$ nanocrystals when Cl:Br ≥ 0.4. [188] Ion migration has been proposed as a cause of the hysteresis phenomena observed in perovskite photovoltaic cells. [195, 196] Two different mechanisms of PL intermittency, blinking (binary on−off switching) and flickering (gradual undulation) behaviors, have been identified in single $FAPbBr_3$ nanocrystals. [197] It was found that surface treatment with sodium thiocyanate (NaSCN) enhanced PLQY and completely suppressed flickering, but had no effect on blinking behavior. [197]

2-1. FA-MA Mixed-Cation Lead Halide Perovskite Nanocrystals

$FAPbX_3$ can be synthesized via cation exchange by replacing MA in $MAPbX_3$ with FA. Post-synthetic cation exchange of $MAPbX_3$ nanocrystals to $FAPbX_3$ nanocrystals was achieved through a solid–liquid–solid cation exchange reaction by adding solid formamidine acetate (FA(Ac)) salts into a toluene solution of $MAPbX_3$ nanocrystals. [198] This cation exchange proceeds slowly due to the minimal solubility of FA(Ac) in toluene. $FAPbX_3$ nanocrystals with emissions spanning from 395 nm to 700 nm can be achieved, depending on the halide ratio of the initial $MAPbX_3$ nanocrystals. Both the absorption and emission spectral features of the perovskite nanocrystals red shifted after cation exchange.

The PL peak of the initial $MAPbBr_3$ nanocrystals was 515 nm and gradually shifted to 531 nm for the final $FAPbBr_3$ nanocrystals. This red shift corresponds to an energy shift of ~73 meV, which is comparable to the ~80 meV difference in band gaps of $MAPbBr_3$ (Eg =2.34 eV) and $FAPbBr_3$ (Eg =2.26 eV) (Figure 3b). [198] Interestingly the FWHM of the PL peak decreased from ~26 nm (122 meV, initial $MAPbBr_3$) to ~20 nm (88 meV, final $FAPbBr_3$), suggesting a narrower particle size/shape distribution of the final $FAPbBr_3$ (Figure 3c). The PLQY slightly decreased from 72% (initial $MAPbBr_3$) to 69% (final $FAPbBr_3$), which could be attributed to an increased number of trap states formed as a result of larger FA^+ cations transporting inside the perovskite crystalline lattices. [198] The evolution of PL lifetime decay during the FA^+ cation exchange reaction were measured and an increase of the overall photo-excited carrier lifetime from 10.2 ns (initial $MAPbBr_3$) to 35.9 ns (final $FAPbBr_3$) was observed (Figure 3d). Longer lifetimes were suggested to result from the relatively stronger interaction between the inorganic sublattice and FA^+, which originates from FA^+'s ability to form four short hydrogen bonds while MA^+ can only form three. [198, 199] The crystal structure of the perovskite nanocrystals was monitored by X-ray diffraction (XRD) and was found to maintain a cubic crystal structure during the cation exchange process. The calculated lattice constant increased from 5.91 Å (initial $MAPbBr_3$) to 6.01 Å (final $FAPbBr_3$), which corresponds to a unit cell volume expansion of 5.2%, induced by the ionic radius difference between the MA^+ and FA^+ cations (the effective radii of MA^+ and FA^+ cations are 2.17 Å and 2.53 Å, respectively). [198]

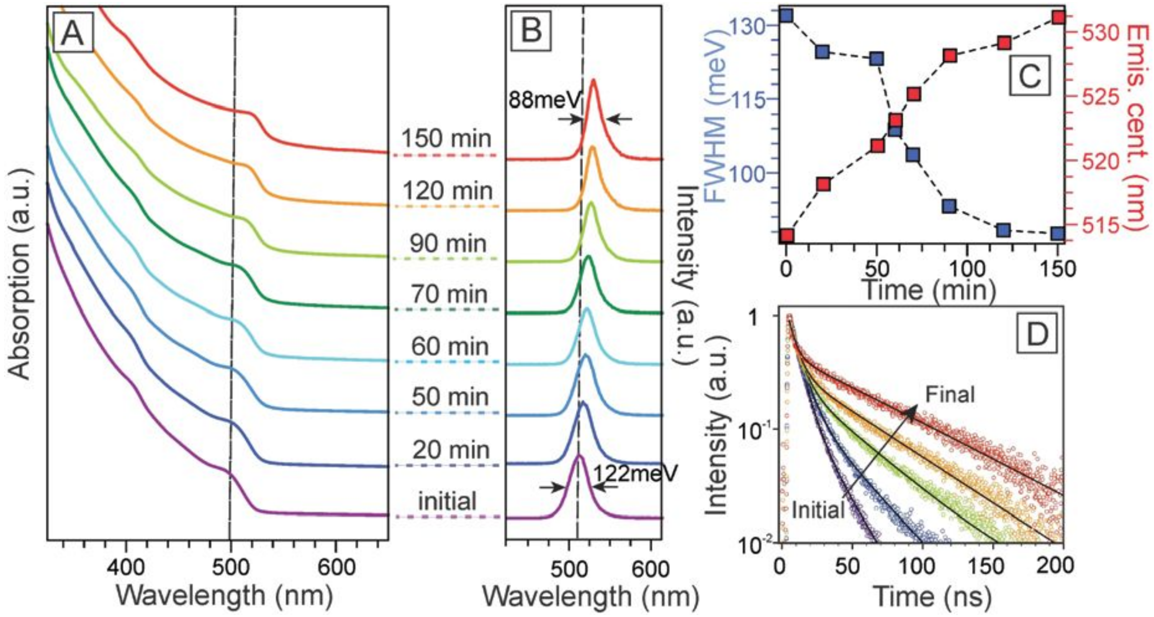

Figure 3. Evolution of optical properties during FA$^+$ cation exchange reaction from the initial $MAPbBr_3$ (purple lines) to the final $FAPbBr_3$ (red lines) perovskite nanocrystals: (A) absorption spectra, (B) photoluminescence (PL) spectra, (C) the PL peak position (red square) and the full width at half maximum (FWHM) (blue square) as a function of reaction time, and (D) the evolution of the PL lifetime decay curves. Reprinted with permission from Ref. [198], copyright 2017, Royal Society of Chemistry.

Perovskite's instability in polar solvents proves to be a challenge for ion exchange preparation of $FAPbI_3$ perovskite thin film solar cells from $MAPbI_3$ crystals. Usually, the cation-exchange process would involve immersing an as-prepared $MAPbI_3$ substrate in a FA$^+$-containing alcohol solution, but the polar nature of alcohol would immediately destroy the existing $MAPbI_3$. [200] To overcome this dissolution issue, $FAPbI_3$ thin film solar cell have been synthesized by converting $MAPbI_3$ to $FAPbI_3$ by exposing the $MAPbI_3$ perovskite film to gaseous FA, allowing the process to occur without polar solvents. [200] Although $FAPbI_3$ demonstrates better thermal stability than $MAPbI_3$, some structural instability challenges remain. It was found that the anisotropically strained (111) plane in the $FAPbI_3$ lattice can promote the transformation of black perovskite phase $FAPbI_3$ (α-phase) to yellow non-perovskite polymorph (δ-phase). Alloying smaller size methylammonium bromide (MABr) into $FAPbI_3$ (forming $FAPbI_3$-MABr) balances this lattice strain (which has shown to significantly enhance moisture stability) as well as contracts the overall lattice by increasing Coulombic interactions due to MABr's relatively smaller size (Figure 4). [201] $FA_xMA_{1-x}PbBr_3$ mixed-cation colloidal nanocrystals have been synthesized using LARP method by mixing different ratios of FABr and MABr precursors together with $PbBr_2$. Their optical properties have exhibited a continuous red-shift with increasing MA doping ratio, [70] a result which contradicts the fact that $FAPbBr_3$ (Eg =2.26 eV) has a smaller band gap than that of $MAPbBr_3$ (Eg =2.34 eV). [198] No clear explanation was given for this contradictory finding.

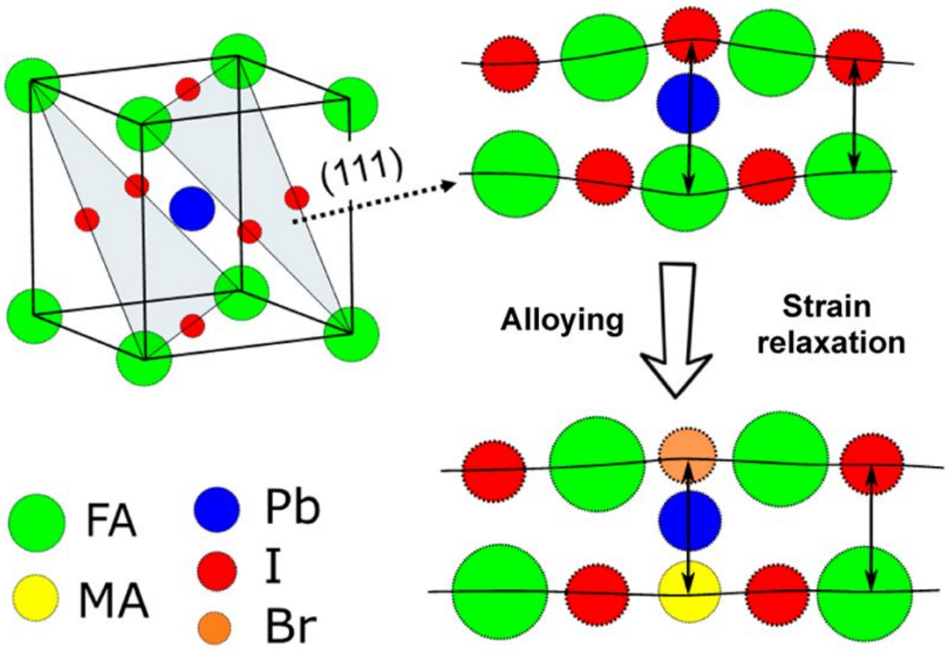

Figure 4. Schematic representation of strain relaxation of $FAPbI_3$ perovskite after MABr alloying (side view). Reprinted with permission from Ref. [201], copyright 2016, American Chemistry Society.

2-2. FA-Cs Mixed-Cation Lead Halide Perovskite Nanocrystals

In addition to $MAPbX_3$ nanocrystals, cation exchange of FA ions has also been implemented on $CsPbX_3$ nanocrystals. $FA_xCs_{1-x}PbI_3$ nanocrystals can be obtained by mixing $CsPbI_3$ nanocrystals with a FA-oleate precursor in toluene solution. [202] The $FA_{0.1}Cs_{0.9}PbI_3$ nanocrystals show a red emission peak at 685 nm with QY exceeding 70% and much better stability than their parent $CsPbI_3$ nanocrystals (PL stability improved from several days to a few months under storage at ambient conditions). The enhanced stability was proposed to be attributed to the lattice expansion caused by insertion of the larger FA^+ (pure $FAPbI_3$ nanocrystals retain their PL stability of near-IR region emission at ~780 nm for a few months when stored in ambient conditions as well). [202] The cation exchange mechanism of Cs^+ and FA^+ ions is reversible (one can obtain $FA_xCs_{1-x}PbI_3$ nanocrystals by mixing $FAPbI_3$ nanocrystals with Cs-oleate precursor as well), though there is an energetic cost of atomic rearrangement since $FAPbI_3$ is a cubic phase and $CsPbI_3$ is a γ-orthorhombic phase. [202] Substituting I with Br is an effective method to tune the band gap of $FAPbX_3$, but crystal will transform from a trigonal to a cubic phase at a critical I/Br ratio. [203] To overcome this issue, Cs has been introduced to stabilize the structure and form $FA_{0.83}Cs_{0.17}Pb(I_{1-x}Br_x)_3$ mixed-cation lead mixed-halide perovskite. [203] The introduction of relatively smaller Cs cations in the A-sites of $FAPbX_3$ contracts the lattice, which reduces the cubo-octahedral volume, thereby inducing stronger interaction between the cations and halides, facilitating the formation of highly crystalline perovskite crystals at a low temperature. [42] Colloidal $FA_{1-x}Cs_xPbBr_3$ mixed-cation perovskite nanocrystals with x=0–0.6 have been synthesized to study the effect of Cs doping (Figure 5a). [42] XRD detected standard perovskite phase throughout the entire composition range for x = 0–0.6 (Figure 5b), though a peak shift from 15.01 to 15.39° was observed, which indicates the shrinking of d-spacing due to incorporation of the smaller Cs cation. Cs doping has also shown to decrease lattice spacing by high-resolution transmission electron microscopy (HR-TEM). Fast Fourier transformation of HR-TEM images allow for the calculation of lattice fringe spacing (Figure 5c), and the linear relationship between d-spacing and Cs content indicates this doping system follows Vegard's law. As Cs doping content increases, the absorption band is blue shifted from 525 nm (x=0) to 503 nm (x = 0.6), (Figure 5d bottom axis) corresponding to a band gap shift from 2.27 to 2.33 eV (Figure 5d top axis). The PL peak is also blue shifted from 531 nm (x=0) to 519 nm (x = 0.6), with narrow

FWHMs of about 19–23 nm (Figure 5e). [42] Colloidal $FA_{0.33}Cs_{0.67}PbBr_{3-x}I_x$ ($0 \leq x \leq 3$) mixed-cation lead mixed-halide perovskite nanocrystals with controllable morphologies such as nanowires and nanosheets over a wide range of halide compositions were achieved by tuning the ligand participating in the reaction (Figure 6). [204] Nanosheets and nanorods can be grown by altering the ratio between oleic acid (OA) and oleylamine (OAm) during the reaction with the existence of bis(2-ethylhexyl)-amine (BEHA). [204] NIR emissive $Cs_xFA_{1-x}Pb(Br_{1-y}I_y)_3$ perovskite nanocrystals has been systematic studied by an automated droplet-based microfluidic platform. [205]

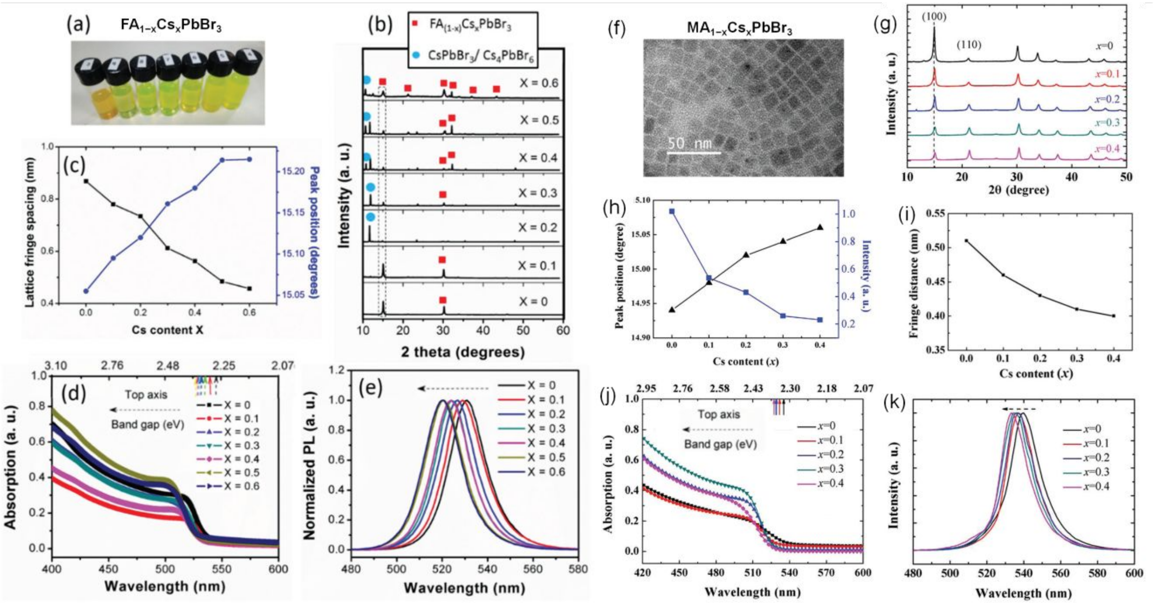

Figure 5. (a) Photographs of different perovskite nanocrystals in solution. (b) XRD patterns of $FA_{1-x}Cs_xPbBr_3$ (x = 0–0.6). (c) Lattice fringe and peak position (≈15°) as a function of Cs content, x, in $FA_{1-x}Cs_xPbBr_3$. (d) Absorption spectra and (e) PL emission spectra of $FA_{1-x}Cs_xPbBr_3$ (x = 0–0.6). Reprinted with permission from Ref. [42], copyright 2017, Wiley-VCH. (f) TEM image of the $MA_{0.7}Cs_{0.3}PbBr_3$ nanocrystals. (g) The XRD patterns obtained for the $MA_{1-x}Cs_xPbBr_3$ (x = 0 to 0.4) perovskites. (h) The (100) peak position and (100) peak, as well as (i) the fringe distance with different Cs content, x. (j) The absorption spectra and (k) PL spectra of $MA_{1-x}Cs_xPbBr_3$ (x = 0 to 0.4) perovskites measured at room temperature. Reprinted with permission from Ref. [206], copyright 2017, Royal Society of Chemistry.

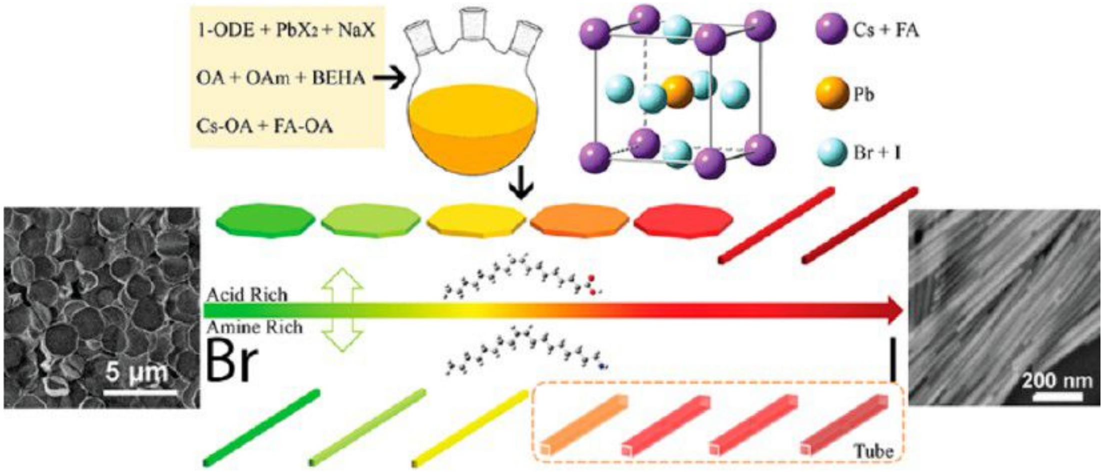

Figure 6. Schematic illustration for the formation of $FA_{0.33}Cs_{0.67}PbBr_{3-x}I_x$ ($0 \leq x \leq 3$) perovskite nanowires and nanosheets, where OA, OAm, and BEHA in the schematic represent oleic acid, oleylamine, and bis(2-ethylhexyl)-amine, respectively. Reprinted with permission from Ref. [204], copyright 2017, American Chemistry Society.

2-3. MA-Cs Mixed-Cation Lead Halide Perovskite Nanocrystals

Colloidal $MA_{1-x}Cs_xPbBr_3$ perovskite nanocrystals were synthesized using the LARP technique. Briefly, MABr, CsBr, $PbBr_2$, oleylamine, and oleic acid were dissolved in DMF and then added dropwise into toluene to form green colloidal nanocrystals. The as-prepared $MA_{1-x}Cs_xPbBr_3$ perovskite nanocrystals are primarily cubic, with sizes varying from 8 nm to 12 nm (Figure 5f). It was found that the absorption spectra blue-shifted from 515 nm to 505 nm when the Cs doping content increased from 0 to 0.4 (Figure 5j) and the PL spectra also gradually blue-shifted from 539 nm to 533 nm as Cs doping levels increased (Figure 5k). The crystallinity of $MA_{1-x}Cs_xPbBr_3$ perovskite was studied by XRD (Figure 5g). It was found that increasing the Cs doping amount decreased the (100) peak intensity and increased the (110) peak intensity, which indicates that (110) is the preferred crystal growth direction. The (100) peak shifted from 14.91 degree to higher values, which indicates shrinkage of the crystal lattice (Figure 5h). To further investigate the effect of Cs doping on the crystal structure, the lattice fringe was calculated from the fast Fourier transformation of the HR-TEM analyses (Figure 5i). Increased Cs doping into $MAPbBr_3$ lead to a reduction of lattice fringe distance due to the relatively smaller ionic radius of Cs atoms, which results in a reduction of the cubo-octahedral volume for the A-site cation. Smaller lattice spacing results in a larger band gap because a smaller lattice constant indicates stronger binding between the valence electrons and their parent atoms, therefore requiring more energy to promote from the valence to conduction band. [206] This trend is visible in Figure 7, where, for every halide choice, nanocrystals with the smallest cation (Cs) emit the shortest wavelength, and nanocrystals with the largest cation (FA) emit the longest wavelength. Note that nanocrystals with MA always emit somewhere between those with Cs and FA, reflecting the fact that its size lies between those two extremes (ionic radii of Cs=1.88 Å, MA=2.17 Å, FA=2.53 Å). [17] This trend helps explain why the energy band gap increased (optical properties blue-shifted) with increasing Cs doping content in the $FA_{1-x}Cs_xPbBr_3$ (Figure 5d and 5e) [42] and $MA_{1-x}Cs_xPbBr_3$ (Figure 5j and 5k) [206] systems. However, individual cases with results contradictory to this trend were still observed in the literature. For example, colloidal $MA_{1-x}Cs_xPbI_3$ perovskite nanocrystals were synthesized using a novel anhydrous toluene assisted method in Dowtherm A. Peak emission wavelength from the nanocrystals was observed to red shift from 671 to 744 nm as the Cs doping increased from x=0.1 to 0.5 (Table 3). [207] The emission shift was attributed to displacement of the valence band (VB) edge due to the Cs-driven transition of nanocrystals from tetragonal to orthorhombic phase. Notably, the shift was not believed to result from any electronic effects from the Cs incorporation. [207]

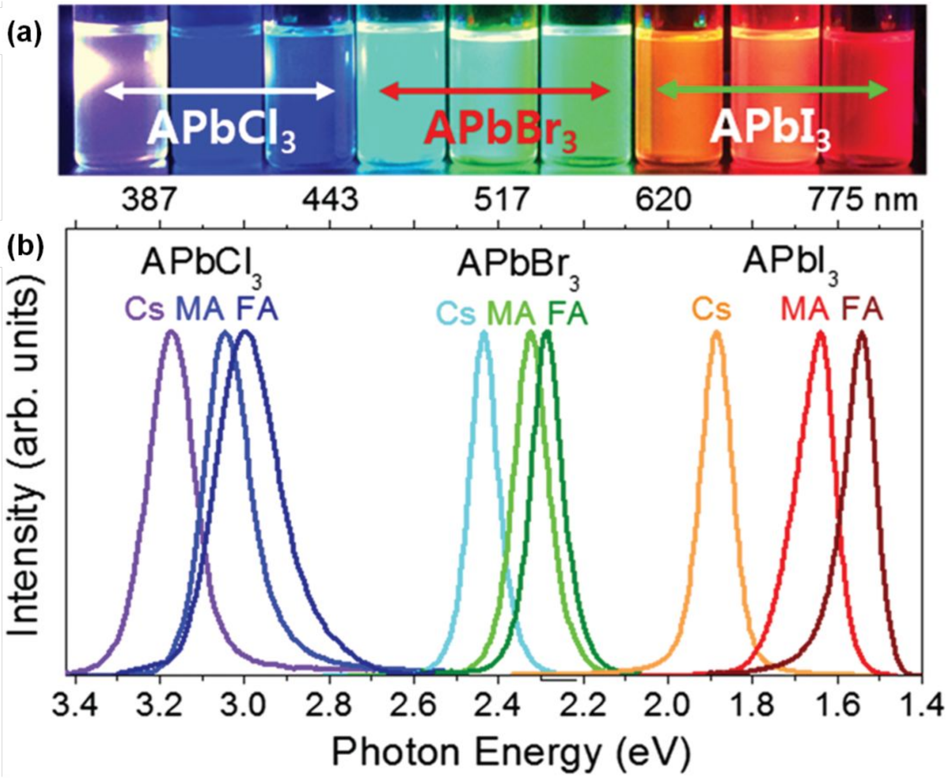

Figure 7. (a) Digital photographs of composition-tuned ultrasound-assist-synthesized colloidal $APbX_3$ (where A = Cs, MA, or FA, and X = Cl, Br, or I) perovskite nanocrystals under UV-lamp (Hg vapor lamp) irradiation, and (b) their corresponding PL spectra. Reprinted with permission from Ref. [17], copyright 2016, Royal Society of Chemistry.

2-4. Other Mixed-Cation Lead Halide Perovskite Nanocrystals

Potassium (K)-doped $CsPbX_3$ nanocrystals have been produced via a reduced temperature recrystallization method using Cs_2CO_3, PbX_2 and KX as precursors. [208] Rubidium (Rb)-doped bulk $Rb_xCs_{1-x}PbCl_3$ and $Rb_xCs_{1-x}PbBr_3$ solid solutions have been achieved through grinding and heating, [209] and colloidal $Rb_xCs_{1-x}PbCl_3$ and $Rb_xCs_{1-x}PbBr_3$ nanocrystals have been synthesized using a hot-injection method. [219] Colloidal $Rb_xCs_{1-x}PbBr_3$ nanocrystals showed a green emission with maximum PLQY of ~60% for $Rb_{0.4}Cs_{0.6}PbBr_3$. [210] Interestngly, another study demonstrated that emission could be tuned from 460 to 500 nm with PLQYs greater than 60% simply by varying the reaction temperatures. [211] Thallium (Tl) has also been used to synthesize perovskite nanocrystals. Orthorhombic Tl_3PbX_5 spheroidal nanocrystals and perovskite $TlPbI_3$ nanowires have been synthesized using a hot-injection method and displayed absorption in the UV range (281-440 nm) and had very weak wide emission across the visible spectrum (450-600 nm). [212] It was suggested that thallium halide (TlBr, TlI) alone has a similar band structure to perovskite, and possesses strong spin–orbit coupling effects and the ability to form photoluminescent colloidal semiconductor nanocrystals. [213]

Table 3. Summary of the emission peak wavelength, full width at half maximum (FWHM), photoluminescence quantum yield (PLQY), and synthesis method of colloidal metal halide perovskite nanocrystals with different A-site substitutions.

Nanocrystals	Emission Peak (nm)	FWHM (nm)	PLQY (%)	Ligands	Synthesis Method	Ref.
$CsPbCl_3$	390	~25	--	Oleylamine	Ultrasound Synthesis	[17]
$MAPbCl_3$	407	~25	--	Oleylamine	Ultrasound Synthesis	[17]
$FAPbCl_3$	413	~25	--	Oleylamine	Ultrasound Synthesis	[17]
$CsPbBr_3$	510	~15	--	Oleylamine	Ultrasound Synthesis	[17]
$MAPbBr_3$	532	~15	--	Oleylamine	Ultrasound Synthesis	[17]
$FAPbBr_3$	541	~15	--	Oleylamine	Ultrasound Synthesis	[17]
$CsPbI_3$	660	~15	--	Oleylamine	Ultrasound Synthesis	[17]
$MAPbI_3$	756	~15	--	Oleylamine	Ultrasound Synthesis	[17]

$FAPbI_3$	805	~15	--	Oleylamine	Ultrasound Synthesis	[17]
$MA_{0.9}Cs_{0.1}PbBr_3$	539	~17	--	Oleylamine, oleic acid	LARP	[206]
$MA_{0.6}Cs_{0.4}PbBr_3$	533	~17	--	Oleylamine, oleic acid	LARP	[206]
$MA_{0.9}Cs_{0.1}PbI_3$	671	~70	58	Octylamine	Anhydrous toluene assisted method	[207]
$MA_{0.8}Cs_{0.2}PbI_3$	738	~87	44	Octylamine	Anhydrous toluene assisted method	[207]
$MA_{0.7}Cs_{0.3}PbI_3$	744	~56	35	Octylamine	Anhydrous toluene assisted method	[207]
$MA_{0.5}Cs_{0.5}PbI_3$	744	~49	26	Octylamine	Anhydrous toluene assisted method	[207]
$FA_{0.9}Cs_{0.1}PbBr_3$	~531	~20	~73	Octylamine, oleic acid	LARP	[42]
$FA_{0.8}Cs_{0.2}PbBr_3$	~529	~20	~65	Octylamine, oleic acid	LARP	[42]
$FA_{0.7}Cs_{0.3}PbBr_3$	~525	~20	~54	Octylamine, oleic acid	LARP	[42]
$FA_{0.6}Cs_{0.4}PbBr_3$	~525	~20	~55	Octylamine, oleic acid	LARP	[42]
$FA_{0.5}Cs_{0.5}PbBr_3$	~520	~20	~47	Octylamine, oleic acid	LARP	[42]

$FA_{0.4}Cs_{0.6}PbBr_3$	~520	~20	~34	Octylamine, oleic acid	LARP	[42]
K^+:$CsPbCl_3$	~405	~15	2.08	Octylamine, oleic acid	Reduced temperature recrystallization	[208]
K^+:$CsPbBr_3$	~500	~30	71.51	Octylamine, oleic acid	Reduced temperature recrystallization	[208]
K^+:$CsPbI_3$	~675	~20	79.51	Octylamine, oleic acid	Reduced temperature recrystallization	[208]
$Rb_{0.2}Cs_{0.8}PbCl_3$	~414	~12	~3	Tri-n-octylphosphine, oleylamine, oleic acid	Hot injection method	[210]
$Rb_{0.4}Cs_{0.6}PbCl_3$	~400	~13	~2	Tri-n-octylphosphine, oleylamine, oleic acid	Hot injection method	[210]
$Rb_{0.6}Cs_{0.4}PbCl_3$	~394	~13	~7	Tri-n-octylphosphine, oleylamine, oleic acid	Hot injection method	[210]
$Rb_{0.8}Cs_{0.2}PbCl_3$	--	--	~9	Tri-n-octylphosphine, oleylamine, oleic acid	Hot injection method	[210]
$Rb_{0.2}Cs_{0.8}PbBr_3$	~514	~18	~35	Tri-n-octylphosphine,	Hot injection method	[210]

				oleylamine, oleic acid		
$Rb_{0.4}Cs_{0.6}PbBr_3$	~512	~22	~59	Tri-n-octylphosphine, oleylamine, oleic acid	Hot injection method	[210]
$Rb_{0.6}Cs_{0.4}PbBr_3$	~505	~22	~48	Tri-n-octylphosphine, oleylamine, oleic acid	Hot injection method	[210]
$Rb_{0.8}Cs_{0.2}PbBr_3$	~495	~24	~36	Tri-n-octylphosphine, oleylamine, oleic acid	Hot injection method	[210]
$Rb_xCs_{1-x}PbBr_3$	460-500	<25	60-90	Oleylamine, oleic acid	Hot injection method	[211]
Tl_3PbI_5	~530	~115	--	Oleylamine, oleic acid	Hot injection method	[212]

3. B-Site Substitution

It was suggested that the formation energy of the B-site is relatively larger than that of the A-site and X-site, which makes partial substitution of the B-site cation more difficult than the other ions in ABX_3 perovskites. [214] The main motivation for B-site substitution is to (1) reduce the toxic lead content, and (2) stabilize the perovskite phase. (1) Lead (Pb), a commonly used B-site species, is a toxic element with restricted use in many countries (including the entire European Union). [215] Identifying a safer, lead-free perovskite with performance equal to that of lead halide perovskite is currently one of the biggest challenges in the field. Isovalent substitution of Pb^{2+} with other divalent cations in the same group of the periodic table (i.e. Ge^{2+}, Sn^{2+}), is the most intuitive strategy and has been realized by many research groups. [216-219] Unfortunately, Sn^{2+} is not stable and easily oxidizes to Sn^{4+}. This oxidation problem is even more pronounced for Ge^{2+} owing to its $4s^2$ electrons, which possess even lower binding energy. [157, 158] Some also argue that the stereoactive lone pair on the Ge^{2+} center may result in highly distorted GeI_6 octahedra with three short and three long Ge–I bonds (quasi-3-D hexagonal structure). [160, 220] (2) Due to the size difference between Br^- and I^- ions, the tolerance factor for lead iodide perovskite is smaller (less stable) than that of the lead bromide perovskite (Table 2). The longer B-X bond length in the $[PbI_6]^{4-}$ octahedra allows it to rotate and tilt more compared to that of the $[PbBr_6]^{4-}$ octahedra. Partial substitution of Pb^{2+} with a smaller B-site cation can reduce the B-X bond length and stabilize the lead iodide perovskite by reducing the extent of octahedral rotation or distortion, thereby leading to larger tolerance factor (improved phase stability) and larger formation energy (improved thermal stability). [214] Despite improved stability, devices made from perovskite with partial or complete substitution of Pb^{2+} often show less impressive optoelectronic properties than those containing Pb. This degradation of optoelectronic properties is because, as mentioned earlier, the 6s and 6p orbitals of Pb^{2+} determine the valence band maximum (VBM) and conduction band minimum (CBM) of lead halide perovskites and substituting Pb^{2+} with other metal ions potentially introduces new defect states between VBM and CBM, destroying the defect tolerant nature of the lead halide perovskites. As a consequence, care must be taken when choosing B-site cations for doping or alloying to retain the impressive optoelectronic properties of metal halide perovskites. [214, 221]

Most effort in finding B-site replacements has focused on alternative isovalent cations that do not oxidize easily, are less toxic, and are smaller than Pb^{2+} ions. The partial replacement of Pb^{2+} with other divalent metal species (e.g., Co^{2+}, Cu^{2+}, Fe^{2+}, Mg^{2+}, Mn^{2+}, Ni^{2+}, Sn^{2+}, Sr^{2+}, and Zn^{2+}) for improving the phase stability or band energy alignment in lead iodide perovskite solar cells have been systematically studied. [214, 222] Besides isovalent substitution, aliovalent (heterovalent) substitution is also an alternative direction for B-site substitution. One can form a so-called "double perovskite" ($A_2B'B''X_6$) structure by replacing two B-site divalent Pb ions with two heterovalent ions ($2B \rightarrow B' + B''$), consisting of one with a higher and one with a lower oxidation state (i.e., one trivalent ion (M^{3+}) and one monovalent ion (M^+) or a quadrivalent ion (M^{4+}) and a vacancy (V^{0+}) forming A_2MX_6 structure). The most intuitive thought would be to substitute Pb^{2+} with

Bi^{3+} and Tl^{1+}, two elements directly adjacent to Pb in the period table (i.e., with same number of atomic orbitals). The lower binding energy of Bi 6p orbitals is likely to reduce the electronic band gap and the combination of trivalent and monovalent ions would cause fluctuations in electrostatic potential. [158] One advantage of this approach is that one can tune the carrier concentrations of perovskite by controlling the substitution ratio between the trivalent and monovalent ions making it into either n-type (by excess Bi) or p-type (by excess Tl). [158] Because this review mainly focuses on ABX_3 type perovskites, double perovskites or other heterovalent doping perovskites will only be lightly discussed.

3-1. Sn-based (Divalent or Quadrivalent Substitution) Perovskite Nanocrystals

Sn is the most obvious substitute for Pb because they are in the same group. By introducing some $SnBr_2$ to partially replace $PbBr_2$ during hot-injection synthesis, Sn(II)-doped $CsPbBr_3$ ($CsPb_{1-x}Sn_xBr_3$) nanocrystals have been synthesized. [223] Increasing the Sn content gradually blue-shifted the absorption edges from 520 nm (x=0) to 496 nm (x=0.7) and blue-shifted the PL peak positions with decreased PLQY from 71% (x=0) to 37% (x=0.7) (Figure 8a and 8b). The blue-shifted band gaps can possibly be attributed to lattice spacing shrinkage due to the smaller ionic radius of Sn cation (1.45 Å) compared to Pb cation (1.80 Å). [223] According to the empirical Vegard's law, [224] the band gap of a semiconductor is approximately a linear function of its lattice parameter and composition. Another group also demonstrated the substitution of Sn by partially replacing $PbBr_2$ with $SnBr_2$ during hot-injection synthesis, yet by using more oleic acid and oleylamine, they achieved a higher PLQY of 73.4%. [225] In their study they found that reaction time, temperature, and the precursor ratio of Pb:Sn all play an important role in the final product, and that both cubic $CsPbBr_3$ and tetragonal Cs_4PbBr_6 may form, depending on the growth conditions. A blue shift in the optical response was also observed when changing the precursor ratio of Pb:Sn from 1:1, 1:2.5 to 1:5. [225] Similarly, $CsPb_{1-x}Sn_xBr_3$ nanocrystals have been synthesized by LARP method (Figure 9). [226] PL intensity was observed to drastically improve at x=0.1, indicating that some Sn doping can promote radiative exciton recombination (Figure 9b). However, PL intensity was found to decrease when x > 0.1, suggesting that significant Sn doping generated numerous defect states with oxidation. The lack of a significant shift in the absorption peak positions signifies that the bandgaps of doped NCs were similar to that of pristine NCs, which are defined by the Pb 6s-Br 4p hybridized orbitals and the Pb 6p orbitals (Figure 9c). However, their PL peak positions were seen to also slightly blue-shifted, consistent with the results noted above. The XRD results suggested that the cubic structure of $CsPbBr_3$ nanocrystals was well maintained upon Sn doping (Figure 9d), but some Cs_2SnBr_6 impurity peaks (assigned by red triangles) were observed as Sn content increased. The morphology of nanocrystals became more irregular as the Sn concentration increased (Figure 9e-9j). Notably, room-temperature synthesis of $CsSnBr_3$ nanocrystals has not yet been reported due to their instability and extremely low PL, thus the highest x value can only be 0.9 instead of 1. [226] $CsPb_{1-x}Sn_xBr_3$ nanocrystals obtained by postsynthetic cation exchange using $SnBr_2$ toluene solution also showed a trend of blue-shifting up to a critical $SnBr_2$ concentration. [227] Doping during hot-injection synthesis is mainly a thermodynamically controlled process, and the room temperature postsynthetic ion exchange reaction is mainly a kinetically controlled process. Due to the rigid nature of the Pb cationic octahedral sublattice, postsynthetic cation exchange of Pb takes much longer than halide exchange. [228, 229] It was found to be easier to substitute Pb ions while the halide ions were being substituted simultaneously. Pb to Sn ion exchange of $CsPbBr_3$ nanocrystals was attempted using both SnI_2 and $SnBr_2$, and after 10 min of stirring only the sample containing SnI_2 successfully exchanged ions. [228] This suggested that the anion exchange reaction between the I/Br anions broke the Pb–Br bonding in the octahedral structure and provided a driving force for the cation exchange between Sn/Pb to happen. X-ray photoelectron spectroscopy (XPS) revealed that the Sn-exchanged perovskites displayed a lower binding energy shift of the Pb 4f spectrum, which demonstrates an increase in the number of Pb–oleate (Pb–OA) (corresponding to lower band energy regions) complexes and a decrease in the number of Pb–Br (corresponding to higher band energy regions) species. [228] This anion-driven cation exchange process in the perovskite systems has also been called halide exchange-driven cation exchange (HEDCE). [229] Interestingly blue-shifted optical responses were observed in most Sn-doped colloidal nanocrystal cases, [223, 225-227, 230] and red-shifted optical responses were observed in most Sn-doped thin film solar cell cases including: $CsPb_{1-x}Sn_xX_3$ [231] and $MAPb_{1-x}Sn_xX_3$ [216, 219] systems. Some even observed that the band gaps of $MAPb_{1-x}Sn_xX_3$ perovskites did not fall in between their parent perovskites ($MAPbX_3$ and $MASnX_3$) but that they are smaller than both of them. [217] A clear explanation of the contradictory optical responses in colloidal nanocrystal systems and thin film solar cell systems was not yet given in the literature. It is possible, however, that this contradiction is related to the halide content in the perovskite systems, noting that most studied thin film perovskite solar cells contain iodide ions and most studied colloidal nanocrystals perovskites contain bromide ions. In colloidal nanocrystal study related to iodide containing perovskites ($CsSn_{1-x}Pb_xI_3$), red-shifted optical responses were observed (Figure 8c and 8d), which is consistent with those trends found in the thin film solar cell systems. [10] Similarly, $MASnI_3$ nanocrystals demonstrate red-shifted optical responses compared to $MAPbI_3$. [232] One possible explanation for the counterintuitive blue-shifted optical properties observed in the $CsPb_{1-x}Sn_xBr_3$ nanocrystal systems is that the absorption and PL properties for bromide containing perovskite nanocrystals are solely determined by the $PbBr_6$ octahedra and would shift to higher energies with stronger interactions. [227] $SnCl_2$ has been used as a co-precursor to dope $CsPbI_3$ nanocrystals in conventional hot injection method. Sn^{2+} can partially replace Pb^{2+}, causing a slight lattice contraction and thus improving the perovskite stability. Cl^- has been found to passivate the surface defects of $CsPbI_3$ nanocrystals, thereby enhancing the PLQY, prolonging the emission lifetime, and improving the stability. The blue-shifted PL observed in this case is attributed to the lattice contraction due to the introduction of Sn. [233]

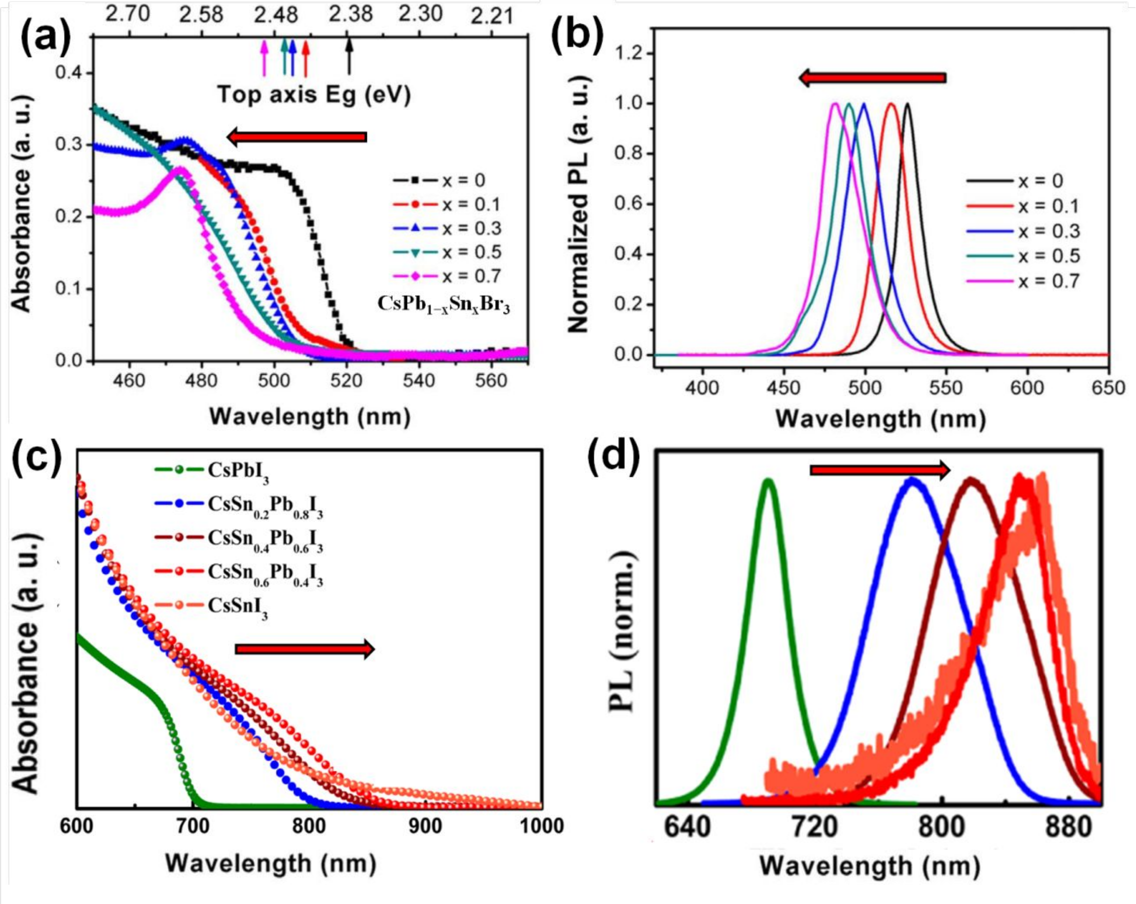

Figure 8. (a) Absorption spectra and (b) normalized PL spectra of $CsPb_{1-x}Sn_xBr_3$ nanocrystals as a function of Sn content (x=0–0.7). Reprinted with permission from Ref. [223], copyright 2016, Elsevier. (c) Absorption spectra and (d) normalized PL spectra of $CsSn_{1-x}Pb_xI_3$ nanocrystals prepared at 160 °C with various Sn/Pb stoichiometries. Reprinted with permission from Ref. [10], copyright 2017, American Chemistry Society. The red arrows indicating the directions of increasing Sn-doping content: (a)(b) blue-shifted optical responses were observed in the Sn-doped cesium lead bromide systems, while (c)(d) red-shifted optical responses were observed in the Sn-doped cesium lead iodide systems.

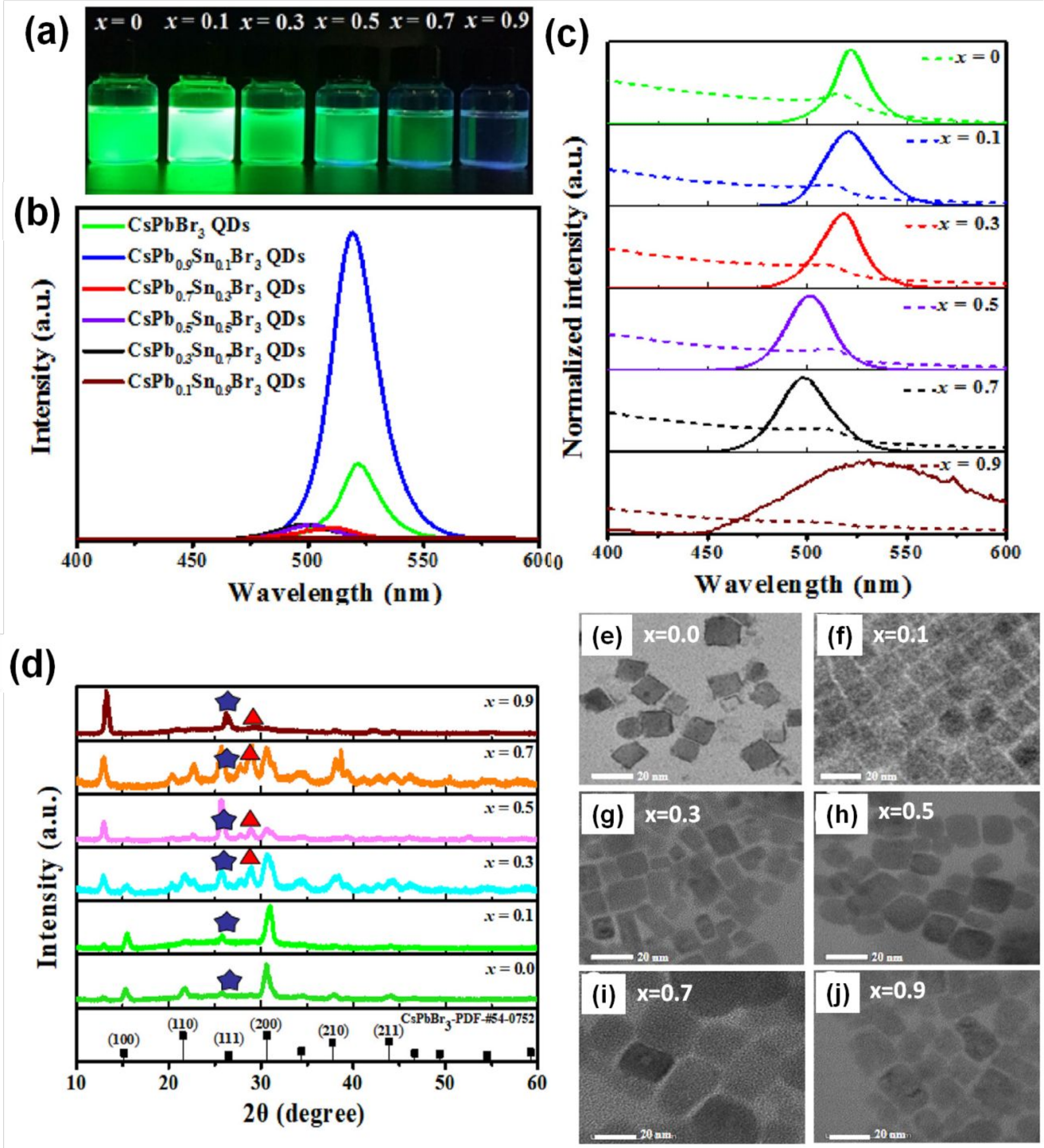

Figure 9. (a) Photographs of CsPb$_{1-x}$Sn$_x$Br$_3$ perovskite nanocrystals hexane solutions under 365 nm UV illumination. (b) PL spectra, (c) normalized steady-state absorption and PL spectra, (d) XRD patterns and (e)-(J) TEM images of CsPb$_{1-x}$Sn$_x$Br$_3$ perovskite nanocrystals as a function of Sn content x. Reprinted with permission from Ref. [226], copyright 2020, Elsevier.

$CsSnX_3$ perovskite nanocrystals have been synthesized via hot-injection method with the assistance of trioctylphosphine (TOP) (Figure 10a-10c), but the resulting $CsSnBr_3$ nanocubes have a relatively low PLQY of 0.14%. [234] Interestingly, unlike the above mentioned $CsPb_{1-x}Sn_xBr_3$ nanocrystals which blue-shifted upon doping of Sn, the optical properties of $CsSnX_3$ nanocrystals are red-shifted when compared with $CsPbX_3$, even in the bromide system. The absorption and emission wavelength of $CsSnX_3$ nanocrystals can be tuned from visible to near-infrared (NIR) (roughly from 500 to 900 nm, see Figure 10b), while the absorption and emission wavelength of $CsPbX_3$ nanocrystals can only be tuned within the visible range (roughly from 400 nm to 700 nm). [234] It was proposed that the band gaps of Sn-containing perovskite nanocrystals are relatively red-shifted (compared with their Pb-based counterparts) because Sn ions have a higher Pauling electronegativity (1.96) than Pb ions (1.87), which leads to a smaller separation between the X 5p states in the valence band and the Sn 5p states in the conduction band. [151] Contrary to this trend, Ge-based perovskites (with high electronegativity of 2.01) like $CsGeX_3$ do not have smaller band gaps than $CsSnX_3$. The X 5p and Ge 4p do not yield band gaps smaller than their Sn counterparts (Table 2) because the smaller Ge^{2+} cation results in a substantially different quasi-3-D hexagonal structure. [151] Similarly, the reported band gap values for $MAGeX_3$ are larger than that of $MASnX_3$ analogs (Table 2) due to its substantially different quasi-3-D hexagonal structure resulting from a second-order Jahn−Teller (SOJT) effect. [151] $CsSnX_3$ perovskite quantum rods with a narrow emission range (from 625 to 709 nm, Figure 10d-10f) have been synthesized using a solvothermal method with the assistance of trioctylphosphine oxide (TOPO) and diethylenetriamine (DETA) in a sealed teflon-lined autoclave. Three unique crystal structures were obtained (Figure 10e), each corresponding to a different halide (monoclinic for $CsSnCl_3$, cubic for $CsSnBr_3$, and orthorhombic for $CsSnI_3$). [235] Besides the nanocubes and quantum rods mentioned above, hollow $CsSnBr_3$ perovskite cubic nanocages have been achieved by hot-injection method using stannus 2-ethylhexanoate (a branched n-alkanoates ligand) as the tin(II) source and $MgBr_2$ as the bromine source (Figure 11). [236] The stability of the $CsSnBr_3$ nanocages can be significantly improved with the surface treatments of perfluorooctanoic acid (PFOA) where PFOA serves as a strong electron-withdrawing group to stabilize Sn^{2+} species. [236]

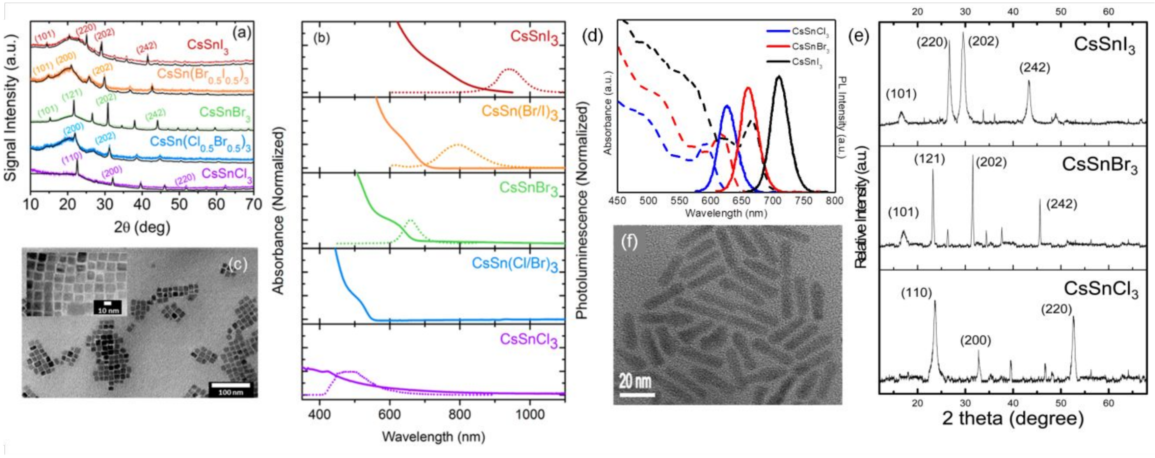

Figure 10. (a) Powder XRD patterns of $CsSnX_3$ (X = Cl, $Cl_{0.5}Br_{0.5}$, Br, $Br_{0.5}I_{0.5}$, I) perovskite nanocrystals. (b) Absorption and steady-state PL spectra of nanocrystals containing pure and mixed halides (Note that due to anion disorder non-emissive mixed halide phase, $CsSn(Cl_{0.5}Br_{0.5})_3$ nanocrystals only showed a very weak emission originating from a small subset of pure $CsSnCl_3$ nanocrystals). (c) TEM images of $CsSnI_3$ nanocrystals. Reprinted with permission from Ref. [234], copyright 2016, American Chemistry Society. (d) Absorption and PL spectra for $CsSnX_3$ (X = Cl, Br, and I) perovskite quantum rods. (e) XRD patterns for $CsSnX_3$ (X = Cl, Br, and I) perovskite quantum rods. (f) High-resolution TEM (HRTEM) image of $CsSnI_3$ perovskite quantum rods. Reprinted with permission from Ref. [235], copyright 2016, American Chemistry Society.

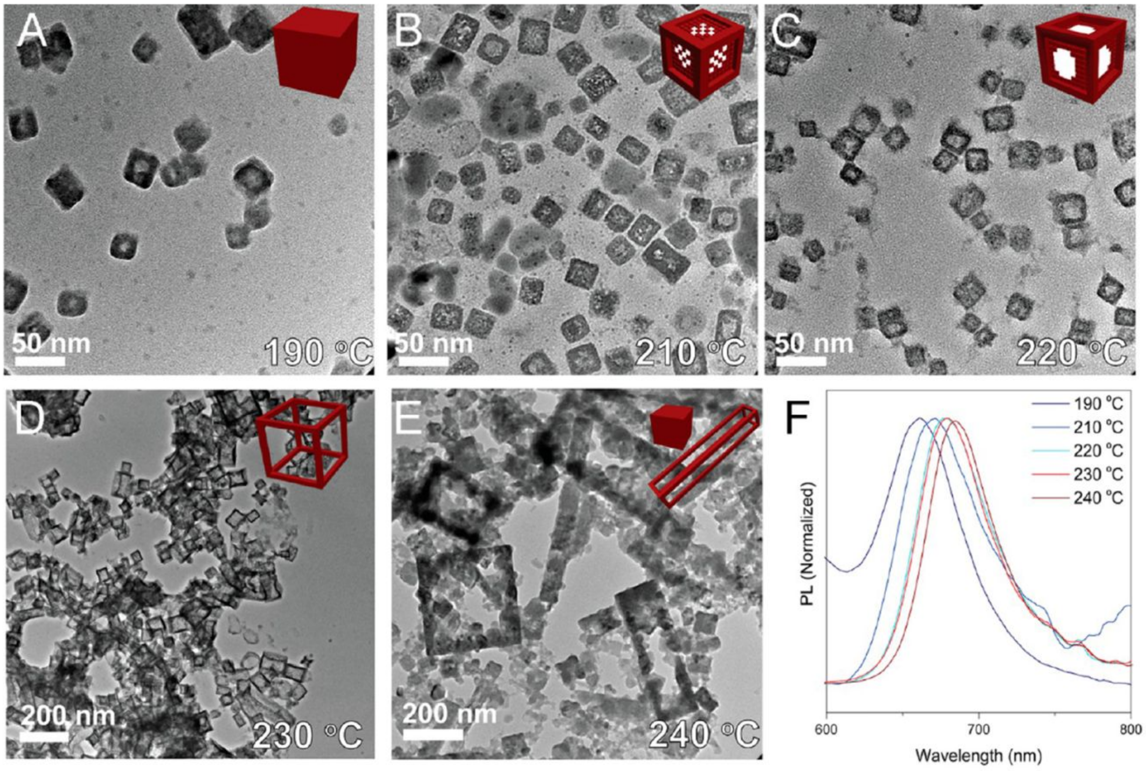

Figure 11. (A−E) TEM images of $CsSnBr_3$ nanoccages synthesized at different reaction temperatures (190, 210, 220, 230, and 240 °C, respectively). (F) Normalized PL emission spectra of the corresponding samples. Reprinted with permission from Ref. [236], copyright 2017, American Chemistry Society.

Because Sn(II) easily oxidizes to Sn(IV) (which causes the instability of $CsSnX_3$), direct synthesis of nancrystals using Sn(IV), instead of ion exchanging with Sn(II), will lead to more stable Sn-based perovskite. $CsPb_{1-x}Sn_xBr_3$ perovskite nanocrystals with Sn(IV) substitution were achieved by hot-injection method. [230] The PLQY increased from 45% to 83% when the relative amount of Sn increased from x=0 to x=0.33 probably due to the suppression of nonradiative Auger recombination trions (charged excitons). Further incorporation of Sn will lead to a decrease in PLQY, which is likely due to the formation of the Cs_2SnBr_6 phase. It is worth noting, however, that the study was conducted using Sn(II) ($SnBr_2$) instead of Sn(IV), so their statement of Sn(IV) substitution is questionable. [230] Cs_2SnI_6 nanocrystals with morphologies of spherical quantum dots, nanorods, nanowires, nanobelts, and nanoplatelets have been achieved by using a tetravalent tin ion (Sn^{4+}) instead of divalent tin ion (Sn^{2+}) as a Pb^{2+} replacement (Figure 12). [237] Ligand-free Cs_2SnI_6 perovskite nanocrystals have also been achieved and demonstrate colloidal stability for 30 min to 12 hours, depending on the particle size. [238] Cs_2SnI_6 is a double perovskite structure, which can be visualized by removing half of the B-site cations in ABX_3 perovskite. Orange emitting 2D Ruddlesden−Popper type $(C_{18}H_{35}NH_3)_2SnBr_4$ ($(OAm)_2SnBr_4$) perovskite nanocrystals have also been achieved with high PLQY of 88%. [239] $CsSnI_3$ also shows phase instability similar to that of $CsPbI_3$: under ambient conditions, the black phase easily transforms to yellow phase. [240] It has been demonstrated that alloyed $CsSn_{1-x}Pb_xI_3$ nanocrystals are stable in ambient air for up to a few months, which is far superior to both of its parent $CsSnI_3$ and $CsPbI_3$ nanocrystals, which are both only air stable for a few minutes. [10] Notably, monovalent, divalent and trivalent cations such as Li^+, Na^+, K^+, Rb^+, Mn^{2+}, Zn^{2+}, Cd^{2+}, Sn^{2+}, Sr^{2+}, Ni^{2+}, Cu^{2+}, Mg^{2+}, Bi^{3+}, In^{3+}, Mn^{3+}, and Sb^{3+} have been doped into $CsSn_{1-x}Pb_xI_3$ nanocrystals to improve their PLQY. Interestingly, only monovalent Na^+ doping displayed a significant PLQY enhancement from ~0.3% to ~28%, while Zn^{2+} and Cd^{2+} doping only improved the PLQY from ~0.3% to ~8%. Moreover, Na^+ doping can enhance the single-color near-band-edge emission, yet the PL spectra of Zn- and Cd-doped $CsSn_{1-x}Pb_xI_3$ nanocrystals exhibited a wide emission plateau extending from 700 to 900 nm. On the basis of these observations, it was suggested that the formation of a stronger chemical interaction between I^- and Sn^{2+} ions upon Na^+ doping could potentially assist the stabilization of Sn^{2+} and suppress the formation of I vacancy defects, thereby resulting in PL enhancement. [241] Incorporation of fluorine (via addition of SnF_2 during fabrication) resulted in significant improvements in both the stability and performance of $FASnI_3$ and $CsSnI_3$ thin film solar cells and $CsSnI_3$ near-infrared lasing. The increased performance can probably be attributed to the suppression of both trap states (Sn vacancies/free carrier density) and Sn^{2+} oxidation, both of which can be explained by the fact that the F^- is a strong electron-withdrawing group that has a stronger interaction with Sn^{2+} than other halides. [242-247] Further study is needed to determine if the increased stability from incorporation of SnF_2 extends into $CsSnI_3$, $MASnI_3$, and $FASnI_3$ nanocrystals. [240] $CsSn_{1-x}Pb_xI_3$ powders with different phases have been prepared via self-organizing processes in aqueous solutions followed by annealing under nitrogen or air for different temperatures and times. [248] It is interesting to see that most studies in tin(II)-based perovskite nanocrystals focus on all-inorganic $CsSnX_3$ nanocrystals, although an early work does document solid state synthesis of $CH_3NH_3SnBr_3$ powders. [119]

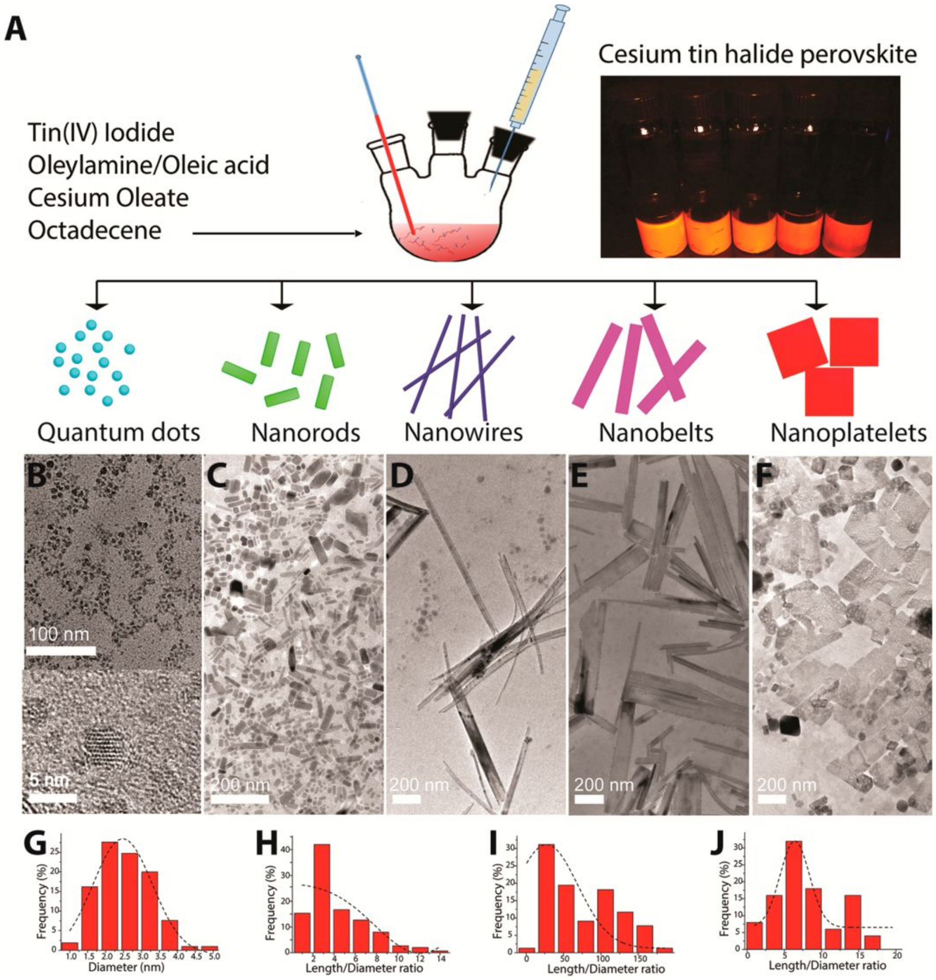

Figure 12. (A) Schematic of the controlled synthesis procedures of Cs_2SnI_6 perovskite nanocrystals with different shapes (left panel) and photograph of the as-prepared Cs_2SnI_6 samples under UV light (top right panel). (B−F) TEM images of Cs_2SnI_6 nanocrystals with different shapes (the inset of B gives an HRTEM image of Cs_2SnI_6 spherical quantum dots). (G) particle size distribution histogram corresponding to (B), and (H−J) length−diameter ratio histograms corresponding to (C−E) (G−J give imaginary lines showing the best-fit

Gaussian distributions). Reprinted with permission from Ref. [237], copyright 2016, American Chemistry Society.

It is worth noting that though scientists have intensively studied using Sn^{2+} as a non-toxic substitute for Pb^{2+} in lead halide perovskite systems, one recent study stated that health effects from SnI_2 are more harmful than potential lead poisoning induced by PbI_2. [249] The synthesis of Sn-based perovskite nanocrystals also usually requires the use of toxic phosphines (TOP or TOPO) as coordinating solvent, which further calls into question whether Sb truly is a safe alternative to Pb. [228, 230, 234, 235]

3-2. Mn-based (Divalent Substitution) Perovskite Nanocrystals

Mn-doping is another widely studied strategy to replace Pb in perovskite nanocrystals. [250] Due to the rigid nature of the Pb cationic sublattice in lead halide perovskite nanocrystals, halide exchange-driven cation exchange (HEDCE previously mentioned) is required to dope Mn. [229] By adding $MnCl_2$ as a doping agent into previously-synthesized $CsPbBr_3$, Pb cations can be partially exchanged by Mn ions and $CsPb_{1-x}Mn_x(Cl/Br)_3$ can be obtained. The resulting $CsPb_{1-x}Mn_x(Cl/Br)_3$ is dual-emitting, with two PL peaks. The HEDCE strategy demonstrates that postsynthetic partial cationic replacement is more likely to occur when the rigid halide octahedron structure is opened due to halide exchange. It was found that only $MnCl_2$ molecules (rather than mixture of Mn and Cl ions) facilitate successful partial cation exchange. The partial cation exchange reaction occurs over an extended time span, and though the final product possesses only two PL peaks, up to three emission peaks appear during the exchange process. [229] Figure 13a illustrates the temporal evolution of PL spectra of $CsPbBr_3$ nanocrystals after adding the $MnCl_2$ precursor. The original emission peak of $CsPbBr_3$ nanocrystals was at around 520 nm which showed green color under the irradiation of a 365 nm UV lamp (the first digital photograph of “0 min” in the upper panel of Figure 13a). After 12 min of reaction, a peak at 438 nm appeared and the peak intensity of 520 nm decreased. The peak at 438 nm is an indication of the fast halide exchange, resulting in the formation of $CsPb(Cl/Br)_3$

nanocrystals. After 43 min of reaction, the peak intensities at 438 nm and 520 nm keep increasing and decreasing, respectively, and another shoulder peak at 572 nm becomes visible (see blowup spectra from the inset). The peak at 572 nm indicates Mn^{2+} ligand-field transition emission from $^4T_1$ to $^6A_1$. [229] The notation $^4T_1 \rightarrow {}^6A_1$ refers to a transition between spin−orbit coupled energy levels of Mn^{2+} originated from the Tanabe-Sugano diagram. [251] It took almost 40 h for completely exchange of all the initial $CsPbBr_3$ nanocrystals into $CsPb_{1-x}Mn_x(Cl/Br)_3$ nanocrystals, which is indicated by the complete disappearance of the peak at 520 nm. The long reaction time is due to the difficult diffusion of large sized $MnCl_2$ molecules into the nanocrystal lattice at room temperature (20°C). Mild heating (50°C) can dramatically shorten the reaction time from 40 h to 2 h due to accelerated molecular diffusion. [229] Because of the slow diffusion of $MnCl_2$ into the center of the nanocrystals, it was proposed that the three intermediate emission peaks are from mid-states of $CsPbBr_3/CsPb_{1-x}Mn_x(Cl/Br)_3$ core/shell structures. With prolonged reaction time (allowing for diffusion), the domain of $CsPbBr_3$ core will gradually decrease and the PL peak of $CsPbBr_3$ (at 520 nm) will eventually disappear. For HEDCE to occur, the halide exchange and cation exchange between $MnCl_2$ molecules and $CsPbBr_3$ nanocrystals must proceed at the same time and same lattice site. It is for this reason that using separate Mn^{2+} and Cl^- ions from different sources do not lead to Mn doping. The same HEDCE strategy can be repeated in different metal systems, like forming Sn-doped perovskite using $SnCl_2$. [229] The final dual-emitting $CsPb_{1-x}Mn_x(Cl/Br)_3$ nanocrystals have the potential to be used in temperature sensing applications due to temperature-dependent intensity of the two PL peaks. Figure 13b reveals that the intrinsic emission peak of $CsPb(Cl/Br)_3$ perovskite at 438 nm gradually decreases when the temperature is increased from 5 °C to 50 °C, which is due to thermally activated trapping of charge carriers. The slight red-shift in PL peak position was due to thermal expansion of the crystalline lattice. [229] The emission peak of Mn at 572 nm was enhanced when the temperature increased, which can be attributed to elevated temperature-promoted exciton-to-Mn energy transfer rates, induced by the increased spectral overlap between perovskite donor and Mn acceptor. The slight blue-shift in peak position can be attributed to thermal expansion of the crystalline lattice which changed the strength of the ligand field on Mn ions. The temperature-dependent exciton-to-Mn energy transfer in $CsPb_{1-x}Mn_x(Cl/Br)_3$ nanocrystals was found to exhibit linear ratiometric emission between the intrinsic perovskite (emission at ~438 nm) and Mn (emission at ~572 nm) (the inset of Figure 13b) and can be used for temperature sensing. [229] A similar temperature-dependent PL study has also revealed the coupling between excitons and the d electrons of the dopants, and it was found that the exciton PL possesses biexponential kinetics where the short-lived emission is ascribed to the surface trapping state recombination while the long-lived component is due to the band-edge excitonic recombination. [252] $CsPb_xMn_{1-x}(Cl/Br)_3$ nanocrystals can also be achieved by mixing $CsPbBr_3$ and $CsPb_xMn_{1-x}Cl_3$ nanocrystals together and stirred for 1 h to complete the simultaneous Mn^{2+} cation and Cl^- anion exchanges, and the absorption and band edge emission of the as-prepared nanocrystals can be elaborately tuned from 402 nm to 514 nm while the real Pb and Mn contents can be analyzed by inductively coupled plasma-optical emission spectrometer (ICP-OES) analysis. [253] The cation exchange process between Pb^{2+} and Mn^{2+} ions has been proven to be a reversible/interchangeable process that one can obtain $CsPb_{1-x}Mn_xCl_3$ nanocrystals by either adding $MnCl_2$ precursors into $CsPbCl_3$ nanocrystal solution or by introducing $PbCl_2$ precursors into $CsMnCl_3$ nanocrystal solution. [254] Similar to the HEDCE method, Mn doping can also occur through cation exchange driven by the photoinduced halide exchange in dihalomethane (CH_2X_2, X= Cl, Br) solvent. [255] Mn^{2+} post-synthetic ion exchange can also be done via a quasi-solid-solid cation exchange reaction. By adding solid $MnCl_2 \cdot 4H_2O$ precursors to dried $CsPbCl_3$ nanocrystals in the presence of ligands and allowing for a 15-hour reaction, Mn^{2+} heterogenous surface doping of the $CsPbCl_3$ nanocrystals, followed by inward dopant diffusion, has been confirmed by electron paramagnetic resonance (EPR) and optical spectroscopies. It was found that the presence of excess oleylamine ligands is able to to activate the Mn^{2+}-precursor and plays an important role in this quasi-solid-solid cation exchange reaction. [256]

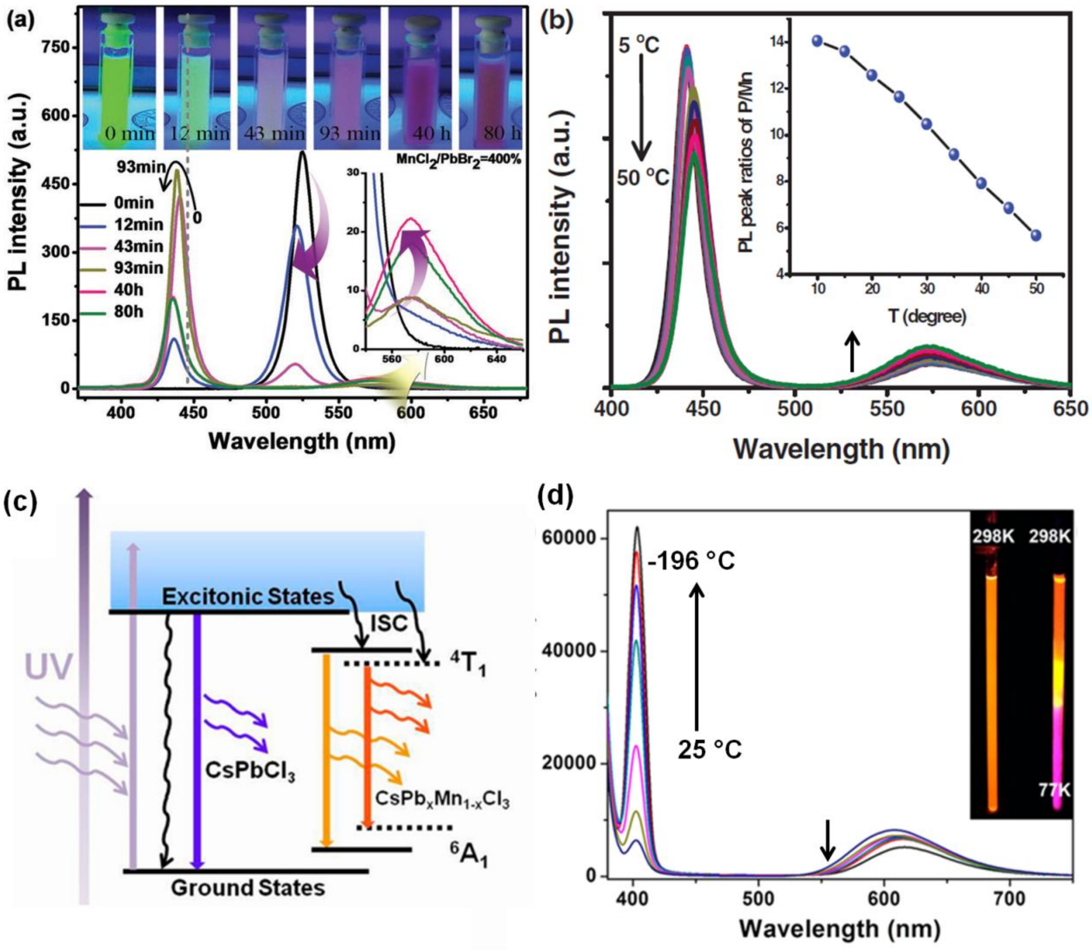

Figure 13. (a) The bottom panel is the temporal evolution of PL spectra of $CsPbBr_3$ nanocrystals after adding the $MnCl_2$ precursor and the top panel is the corresponding digital photograph at different times under the irradiation of a 365 nm UV lamp. The inset is the blowup spectra between 550-650 nm. (b) PL spectra of $CsPb_{1-x}Mn_x(Cl/Br)_3$ nanocrystals collected from 5 °C to 50 °C. The inset is the ratio of PL peak intensity between perovskite intrinsic emission at ~438 nm and Mn emission at ~572 nm. Reprinted with permission from Ref. [229], copyright 2017, Wiley-VCH. (c) Energy levels and fluorescent mechanism of $CsPb_xMn_{1-x}Cl_3$ nanocrystals, where ISC represents intersystem crossing. (d) Temperature-dependent emission spectra of the $CsPb_{0.73}Mn_{0.27}Cl_3$ nanocrystals collected from 25 °C to -196 °C. Reprinted with permission from Ref. [257], copyright 2017, American Chemistry Society.

Direct replacement of Pb with Mn during colloidal synthesis is easier than using above mentioned post-synthetic processes. It has been demonstrated that by using a phosphine-free hot-injection preparation method, the Mn substitution ratio can reach 46% ($CsPb_{0.54}Mn_{0.46}Cl_3$). [257] The energy transfer of photoinduced excitons from the $CsPbCl_3$ host to the doped Mn greatly enhanced the PLQY of the $CsPbCl_3$ nanocrystals. In the temperature-dependent dual emission study, they decreased the temperature from 298 K to 77 K (from 25 °C to -196 °C) and found that the intensity of the 390nm emission peak greatly increased, with no significant shift in peak position (Figure 13d). The intensity of the 580 nm emission peak slightly decreased and the peak position red-shifted to longer wavelengths. The dual PL emission from the Mn-doped $CsPbCl_3$ can be explained by this model (Figure 13c): $CsPbCl_3$ host absorbs energy from the 365 nm excitation source and emits light at 390 nm via radiative recombination of the excitons. Electron or hole traps lead to nonradiative relaxation (energy loss) with low PLQY. The Mn substitution generates new states that allow exciton-to-Mn^{II} energy transfer from the $CsPbCl_3$ host to the doped Mn^{II} ions. Excitons with sufficient thermal activation energy are allowed to transfer from one excited state to the other via intersystem crossing (ISC) ($^4T_1$–$^6A_1$ transition, d−d transition of Mn^{II} ions). [257] New radiative recombination pathways of exciton-to-Mn^{II} energy transfer result in a longer fluorescent lifetime and emission of light at 580 nm with enhanced PLQY. The PL intensity of $CsPbCl_3$ host is enhanced with decreased temperature due to the restriction of nonradiative relaxation processes, and the PL intensity of the Mn^{II} ion is reduced because fewer electrons have sufficient thermal energy to undergo the ISC process. The decreased temperature slightly reduced the energy level of the $^4T_1$–$^6A_1$ transition and therefore the emission wavelength of Mn^{II} slightly red-shifts. It was found that a Mn^{II} doping ratio of 27% ($CsPb_{0.73}Mn_{0.27}Cl_3$) obtains the highest PLQY of 54% (Table 4). [257] It has also been found that Mn doping cannot occur when Mn-carboxylates such as manganese(II) acetate ($Mn(Ac)_2$), manganese(II) acetylacetonate ($Mn(Acac)_2$), and manganese-oleate ($Mn(oleate)_2$) are used as Mn precursors, suggesting that pre-existing Mn−Cl bonds are beneficial for incorporating Mn into the lattice, similar to the prerequisite of HEDCE process mentioned above. [258] Although one can synthesize Mn-doped $CsPbCl_3$ by mixing $PbCl_2$ and $MnCl_2$ during synthesis, the same approach was not successful for $PbBr_2/MnBr_2$ or PbI_2/MnI_2 systems. This is probably due to the differences in their bond strengths. The bond dissociation energy of Mn−Cl (338 kJ/mol) is only 12% higher than that of Pb−Cl (301 kJ/mol), the bond dissociation energy of Mn−Br (314 kJ/mol) is 26% stronger than that of Pb−Br (249 kJ/mol), and Mn−I bond (282 kJ/mol) is 46% stronger than Pb−I bond (194 kJ/mol). [258] It was suggested that the similar bond energy of $PbCl_2$ and $MnCl_2$ favors mixing of these isovalent ions within the lattice, which leads to successfully doped perovskite nanocrystals. In the other two cases, the large disparity in bond energies may favor extended domains of MnX_2 instead of the dispersion of Mn^{2+} within perovskite lattice. [258] Therefore, to obtain Mn-doped $CsPbBr_3$ or $CsPbI_3$ nanocrystals, one will need to first synthesize Mn-doped $CsPbCl_3$ nanocrystals then substitute the halide anion via postsynthetic anion exchange by adding excess $PbBr_2$ then PbI_2. The dual emission phenomenon from the energy transfer between the host and the dopant seen in Mn-doped $CsPbCl_3$ systems is less significant in the Mn-doped $CsPbBr_3$ system and can hardly be seen in the Mn-doped $CsPbI_3$ system. This is because of the energy level mismatch in the latter two cases. The energy difference (Δ) between the host perovskite band edge transition (CB-to-VB) and the dopant Mn transition ($^4T_1$-to-$^6A_1$) determine whether it is a forward energy transfer (k_{ET}) or a backward energy transfer (k_{BET}) (Figure 14). [258] No Mn peak can be seen in the Mn-doped $CsPbI_3$ system (bottom left panel of Figure 14) because the small band gap of the host $CsPbI_3$ results in backward energy transfer (k_{BET}) from the Mn dopant to the perovskite host. The evolution of the exciton-to-Mn^{2+} energy transfer (ET) efficiency as a function of composition (Br/Cl ratio) and temperature in Mn^{2+}-doped $CsPb(Br/Cl)_3$ nanocrystals has been studied. [259]

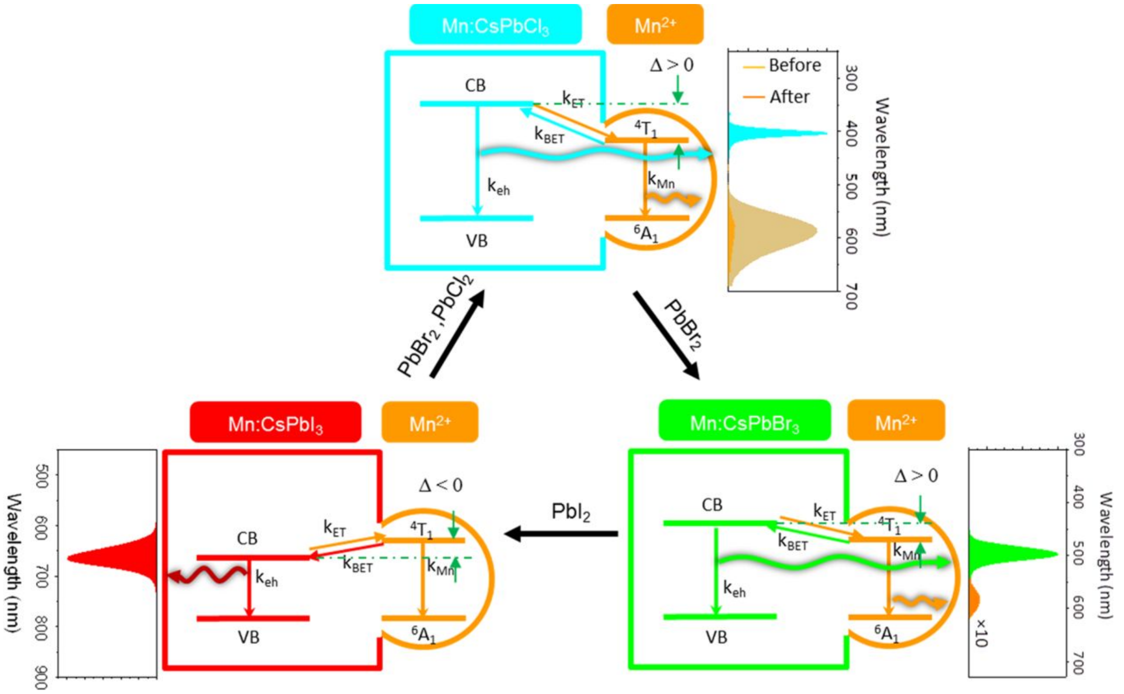

Figure 14. The evolution of the energy level diagram of Mn-doped CsPbX$_3$ (Mn:CsPbX$_3$) nanocrystals during forward and reverse anion exchange. CB and VB denote the conduction and the valence band of the nanocrystal, respectively. The relative intensities of the two PL features of Mn:CsPbX$_3$ nanocrystals are established by the interplay of rates of several competing processes including: band edge electron−hole recombination (k$_{eh}$), deactivation of the Mn^{2+}-based d−d transition (k$_{Mn}$), and forward (k$_{ET}$) and back (k$_{BET}$) energy transfer between the nanocrystal and the impurity. The competition between the latter two processes is also strongly influenced by the energy difference (Δ) between the band edge and Mn^{2+}-based transitions. (Top panel) The Δ in freshly prepared Mn:CsPbCl$_3$ nanocrystals is large and positive, favoring forward energy transfer and strong Mn^{2+}-based PL (yellow shading spectrum labeled as Before in the top right box). After anion exchange with PbBr$_2$, (bottom right panel) the Δ in resulting Mn:CsPbBr$_3$ nanocrystals is still positive but much smaller; and some Mn^{2+} is lost to ion exchange with Pb^{2+}. Both effects lead to reduced Mn^{2+}-based PL (orange shading spectrum in the bottom right box; amplitude multiplied by a factor of 10). After further exchange with PbI$_2$, (bottom left panel) the Δ in the obtained Mn:CsPbI$_3$ nanocrystals is negative, resulting in no Mn^{2+}-based PL (bottom left box). Finally, reverse anion exchange by sequentially exchanging Mn:CsPbI$_3$ with PbBr$_2$ then PbCl$_2$ returns nanocrystals from Mn:CsPbI$_3$ to Mn:CsPbBr$_3$ then Mn:CsPbCl$_3$

(top panel), restoring a large and positive Δ, leading to the re-emergence of Mn^{2+}-based PL. Note that the intensity of the Mn^{2+}-based PL is much smaller compared to the freshly prepared samples (orange shading labeled as After in the top right box), due to the loss of Mn^{2+} when Pb-containing exchange precursors are used. Reprinted with permission from Ref. [258], copyright 2016, American Chemistry Society.

The theory of bond dissociation energy difference mentioned above, suggests that the combination of $PbCl_2$ (301 kJ/mol) and $MnBr_2$ (314 kJ/mol), instead of $PbBr_2$ (249 kJ/mol) and $MnCl_2$ (338 kJ/mol), will create better Mn-doped $CsPb(Cl/Br)_3$ nanocrystals because the difference in their bond dissociation energy is only 4% (much smaller than that of the later combination of 36%. Somewhat surprisingly, many research groups have used a combination of $PbBr_2$ and $MnCl_2$ precursors to achieve Mn-doped $CsPb(Cl/Br)_3$ via both a hot-injection approach [260] and room temperature synthesis [261]. Rationale for this seeming contradiction is still under debate. Successful synthetic procedures for doping Mn into $CsPbBr_3$ [262] and $CsPbCl_3$ [258] nanocrystals are very similar. The procedure for the former and latter are summarized below, respectively: heating a $PbBr_2/MnBr_2/HBr$ mixture with capping ligands first, then swiftly inject Cs-oleate vs. heating $PbCl_2/MnCl_2$ mixture with capping ligands first, then swiftly inject Cs-oleate. The only differences in the previous case compared to the latter are the addition of HBr, some additional capping ligands, and a slightly different heating temperature. Therefore, it is possible that the addition of HBr is key to successfully doping Mn into $CsPbBr_3$ nanocrystals. Their results suggest that Mn luminescent intensity is strongly depended on the amount of HBr used to control the x value in the $L_2[Pb_{1-x}Mn_x]Br_4$ intermediate structure (where L=ligand). [262] Although no other papers mentioned the importance of adding HBr during the Mn doping process, a few papers did mention the importance of adding HCl during the Mn doping process in $CsPbCl_3$ systems. [263-265] While $PbCl_2$ and $MnCl_2$ have been used as the Pb and Mn precursors for most of the Mn-doped $CsPbCl_3$ studies, Xu *et al.* demonstrated that Mn-doped $CsPbCl_3$ can also be achieved at room temperature through the use of lead(II) acetate ($Pb(Ac)_2$), manganese(II) acetate ($Mn(Ac)_2$), and a small amount of HCl acid solution. [263] The acetate ligands in the metal acetate salts will be replaced by oleate ligands and form soluble metal-oleate complexes when dissolved in toluene with the presence of oleic acid and oleylamine. Hydrochloric acid is proposed to play two roles in the room-temperature synthesis of Mn-doped $CsPbCl_3$: (1) protonating the carboxylate groups of the oleate ligand which increases the concentration of active metal monomers, and facilitates generation of $CsPbCl_3$ nanocrystals and (2) providing excess Cl^- to the surface of nanocrystals, increasing the potential binding sites for Mn^{2+}. An optimal amount of HCl exists in order to obtain the highest Mn emission. [263] It was proposed by Adhikari *et al.* that using alkylamine hydrochloride (RNH_3Cl, created by mixing oleylamine and HCl) during synthesis will increase the reactivity of $MnCl_2$ with $PbCl_2$ in the hot-injection method and create more, smaller particles, facilitating the slow Mn^{2+} doping process (no fast cooling required). [264] Mn doping by slowly dripping a small volume of $SiCl_4$ into a dispersion of $CsPbCl_3$ nanocrystals (prepared by hot-injection method with the presence of manganese(II) stearate) in toluene at room temperature was also proposed by Lin *et al.* [265] They found slow incorporation of Mn^{2+} when the reaction proceeded in air and no doping was found for the reaction run under vacuum. They proposed that this was due to the formation of HCl during the hydrolysis of $SiCl_4$ with the water in air (by the reaction of $SiCl_4 + 2H_2O \rightarrow SiO_2 + 4HCl$). Under vacuum, there was no air (water) to trigger hydrolysis of $SiCl_4$. HCl serves many purposes in this process: (1) reacts with the manganese(II) stearate precursor releasing Mn^{2+}, (2) etches the surface of $CsPbCl_3$ nanocrystals (by H^+), and (3) reconstructs/passivates the surface of $CsPbCl_3$ nanocrystals (by Cl^-). [265] Halide acid is not always necessary for Mn-doping; one group successfully doped Mn into $CsPbI_3$ without the addition fo HI by using hot-injection method with a combination of PbI_2, MnI_2 and Cs-oleate. [266]

In Mn-doped $CsPbCl_3$ nanocrystals, the host exciton can undergo ultrafast nonradiative Auger-like recombination (τ_{Aug} = ~12 ps) when co-existing with the long-lived excited Mn-dopant state. Such a fast Auger-like process competes with the exciton-to-dopant spin-exchange internal energy transfer (IET, with τ_{IET} = ~303 ps). The generation of multiple Mn-emission sites through consecutive IET is thus difficult, allowing for Mn-dopant emission from only one Mn^{2+} site per nanocrystal at a time. This is different from the Mn-doped CdS or CdSe quantum dots with consecutive exciton-to-dopant IET processes that generate multiple excited Mn-dopants per nanocrystal. Notably, such a dopant-induced Auger-like recombination corresponds to the broadly observed excitation-dependent saturation of dopant emission in Mn-doped nanocrystals. [267] Mn-doped $CsPbCl_3$ nanocrystals showed an energy transfer time (τ_{ET}) of 380 ps, which is slower than the 70-190 ps energy transfer time of Mn-doped CdS/ZnS core/shell quantum dots. [268] Because the exciton−Mn energy transfer time is longer for Mn-doped $CsPbCl_3$ nanocrystals than Mn-doped CdS/ZnS core/shell quantum dots, it can be concluded that Mn-doped $CsPbCl_3$ nanocrystals have weaker exciton−Mn exchange coupling than Mn-doped CdS/ZnS core/shell quantum dots. [268] This is because, unlike Mn-doped CdS/ZnS core/shell quantum dots, $CsPbCl_3$ nanocrystals (cubes with length of ~10 nm in this specific study) are larger than their Bohr radius (the Bohr radius/exciton binding energy of $CsPbCl_3$, $CsPbBr_3$, and $CsPbI_3$ are 2.5 nm/75 meV, 3.5 nm/40 meV, and 6 nm/20 meV, respectively) [5] and therefore quantum confinement has no effect on exciton−dopant exchange coupling. In $CsPbCl_3$ nanoplatelets, where the thickness of the $CsPbCl_3$ nanoplatelets is smaller than their Bohr radius, enhanced dopant−carrier exchange interaction is observed due to strong quantum confinement effects. [269]

Excitation-dependent emission color tuning from an individual Mn-doped $CsPbCl_3$ microcrystal with a wide color tuning range (reversible between orange and blue) has been reported (Figure 15c). Mn-doped $CsPbCl_3$ microcrystals were grown by immersing a $PbAc_2$-coated glass slide in a mixed isopropanol solution containing $MnCl_2 \cdot 4H_2O$ and CsCl for about 48 h at room temperature, and exhibit dual-color emission from both perovskite host excitons (blue) and Mn-dopants (orange) via an exciton-to-dopant IET process (Figure 15a). By simply changing the laser excitation repetition rate or pulse intensity, the relative emission intensity between exciton ($I_{exciton}$) and Mn-dopant (I_{Mn}) can be continuously and reversibly altered from $I_{Mn} >> I_{exciton}$ to $I_{exciton} >> I_{Mn}$ with increasing excitation intensity (Figure 15b). Such emission color tuning is enabled by (1) the saturation of Mn-dopant emission at high excitation intensity through a bottlenecked energy transfer effect mediated by shallow trap states, and (2) a linear dependence of host exciton emission with excitation intensity. It has been demonstrated that this reversible emission color switching is highly photo-stable as the emission color can be switched between orange and blue for more than 300 cycles within a continuous 14 h operation. [270] Up to 2% Mn-doped $CsPbCl_3$ nanoplatelets, with dimensions of 32 nm by 9 nm (length by width) and thickness of 2.2 nm (4 monolayers), can be achieved through room temperature synthesis method (Figure 16a). [269] Room temperature synthesis of $CsPbCl_3$ nanoplatelets was achieved by modifying the room temperature synthesis of $CsPbBr_3$ nanoplatelets. [271] In Mn-doped $CsPbCl_3$ nanoplatelets, the $CsPbCl_3$ excitonic PL (emission peaks around 400 nm in Figure 16e) is quenched by the new midgap levels created by Mn d states. At the same time, the excitonic energy transferred from the perovskite host to the Mn^{2+} dopant leads to a spin-forbidden $^4T_1-^6A_1$ Mn d-electron emission (emission peaks around 600 nm in Figure 16e) and enhances the PLQY from 2.8% (undoped $CsPbCl_3$ nanoplatelets) to 20% (0.8% Mn-doped $CsPbCl_3$ nanoplatelets). Further increasing the doping ratio from 0.8% to 2% reduces PL efficiency. This decrease is probably due to the increase of intrinsic defects [261] or due to increased interactions between neighboring Mn^{2+} ions, similar to cases of Mn-doped II−VI semiconductors where an optimal Mn-doping concentration exists. [269] Undoped $CsPbCl_3$ nanoplatelets possess a low PLQY of 2.8% (compared to $CsPbBr_3$ nanoplatelets that usually show PLQY as high as 90%), which could be because there is a greater probability of capping molecules forming nonradiative deep midgap states for wider band gap semiconductors. Further anion exchange reactions can convert these Mn-doped $CsPbCl_3$ nanoplatelets into Mn-doped $CsPbBr_3$ nanoplatelets, which still exhibit weak Mn emission. [269] Mn-doped $CsPbBr_3$ perovskite magic sized clusters (PMSCs) and perovskite quantum dots (PQDs) have been synthesized at a room temperature using manganese(II) chloride tetrahydrate ($MnCl_2 \cdot 4H_2O$) and $MnBr_2$ as Mn^{2+} dopant sources and benzoic acid (BA) and benzylamine (BZA) as passivating ligands. [272] The fluorescence of Mn-doped $CsPbBr_3$ PMSCs and PQDs synthesized with 0.10, 0.20, 0.30, and 0.40 mol of $MnCl_2 \cdot 4H_2O$ changed from green to blue, pink and orange (Figure 17c). Their UV-vis spectra have two or three excitonic absorption peaks at 392/411/464, 395/452, 398/450 and 399/447 nm, respectively (Figure 17a), and the corresponding PL spectra display multiple emission peaks at 398/412/471/585, 411/455/589, 411/454/590, and 411/455/591 nm, respectively (Figure 17b), with increasing $MnCl_2 \cdot 4H_2O$ concentration. [272] It may be possible that the Mn and Cl are simultaneously doped into the $CsPbBr_3$ nanocrystals, resulting in Mn-doped $CsPb(Br/Cl)_3$ nanocrystals that show blue-shifted perovskite intrinsic peak with increasing amount of $MnCl_2$ precursors, similar to the HEDCE previously discussed. We note that, in this study, such blue-shifted peak were attributed to the effect of passivation and smaller size nanocrystals formation from the additional Cl^- ions. [272] To this point, it is not known whether room temperature synthesis or hot-injection method is better for incorporating a higher Mn doping ratio. The Mn doping concentration using room temperature synthesis can be as high as 37 % ($CsPb_{0.63}Mn_{0.37}Cl_3$), [261] while an Mn doping ratio of 46% ($CsPb_{0.54}Mn_{0.46}Cl_3$) can be achieved by hot-injection. [257] Room temperature synthesis may lead to higher doping ratio than high temperature synthesis because the doped Mn^{2+} ions could be ejected from the surface of nanocrystals (a phenomenon known as self-purification or self-annealing process) when subjected to high temperatures. [261, 273-275] Some scientists doubt the presence of the defect self-purification process in nanocrystals because the diffusion barriers for most defects cannot be readily overcome at temperatures used in colloidal synthesis (350 °C and below). [276] Doping Mn^{2+} into traditional II−VI semiconductor quantum dots has been demonstrated to be more difficult than doping into bulk and was also proposed to be a result from the exclusion effect. [258] At typical colloidal synthesis temperatures (<350 °C), the impurity diffusion rate into the semiconductor lattice is negligible and therefore the doping is accomplished via control over kinetic factors. [258] A few approaches have been proposed to promote Mn inclusion. One approach is to take advantage of the strong binding of dopant ions to specific crystal facets, followed by material overgrowth. Another approach is to utilize polychalcogenide precursors which feature Mn directly bound to other lattice constituents in a cluster form, which will favor Mn's inclusion. [258] One can tell whether the Mn-doping is substitutional or interstitial via XRD patterns of the perovskite powders/films. If the Mn doping is substitution, the XRD peak will shift to higher 2θ values indicating the incorporation of smaller Mn into the lattice sites of Pb. If the Mn doping is interstitial, the XRD peak will shift to lower 2θ, indicating an expansion of the crystalline lattice due to the insertion of Mn^{2+} ions in the interstices. [277] Mn-doped $CsPbCl_3$ nanocrystals were synthesized by the halide-rich method using manganese(IV) oxide (MnO_2). [278] When fabricated at the molar ratio of Pb/Mn/Cl=1:1:8, Mn^{4+} (from MnO_2) was witnessed to be reduced to Mn^{2+} (in the form of $MnCl_2$) and dope into the $CsPbCl_3$ lattice. [278] Mn^{2+}-doped $CsPbCl_3$ nanocrystals have been synthesized using a single-step ultrasonic synthesis route, and triethylamine (TETN) was introduced to passivate the surface of $CsPbCl_3$:Mn nanocrystals. [112] Gram-scale mass production of Mn^{2+}-doped $CsPbX_3$ nanocrystals have been achieved through a microwave-assisted hot injection method [279] and a solvent-free mechano-synthesis approach. [122] Mn^{2+}-doped $CsPbCl_3$ and $CsPb(Br/Cl)_3$ nanocrystals have also been achieved through a room-temperature transformation doping method from Cs_4PbX_6 nanocrystals. [280] Mn-doped lead-free $Cs_2AgInCl_6$ and Cs_2AgBiX_6 (X= Cl, Br) double perovskite nanocrystals have also been studied. [281, 282] Mn and Ni codoped $CsPbCl_3$ perovskite nanocrystals have also been realized through the addition of $NiCl_2$. [283]

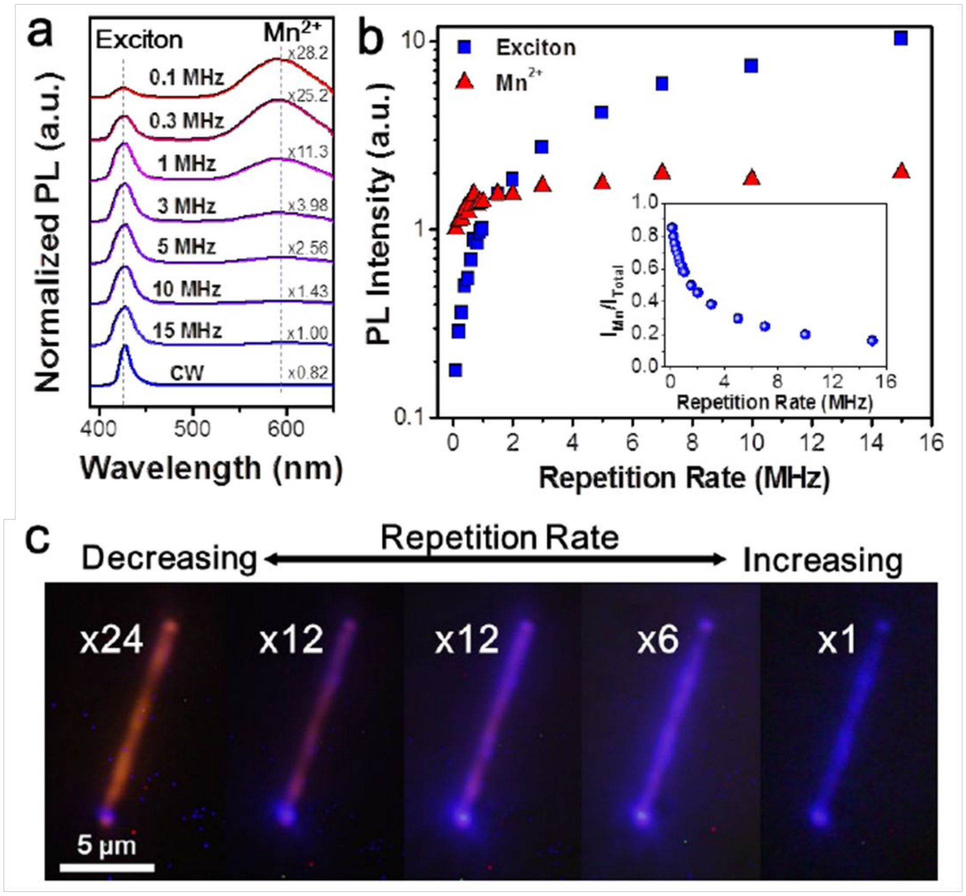

Figure 15. (a) A set of PL spectra and (b) the corresponding change of integrated emission intensities of host exciton ($I_{exciton}$) and Mn-dopant (I_{Mn}) collected from an individual Mn-doped $CsPbCl_3$ microcrystal excited under various laser repetition rates. The inset is a plot of I_{Mn}/I_{total} (where $I_{total}=I_{Mn}+I_{exciton}$) as a function of excitation repetition rate. (c) PL images

of an individual Mn-doped microcrystal showing the continuous change of emission color between orange and blue with increasing/decreasing the excitation repetition rate. The numbers next to the image are the magnification of PL intensity for comparison. Reprinted with permission from Ref. [270], copyright 2019, American Chemistry Society.

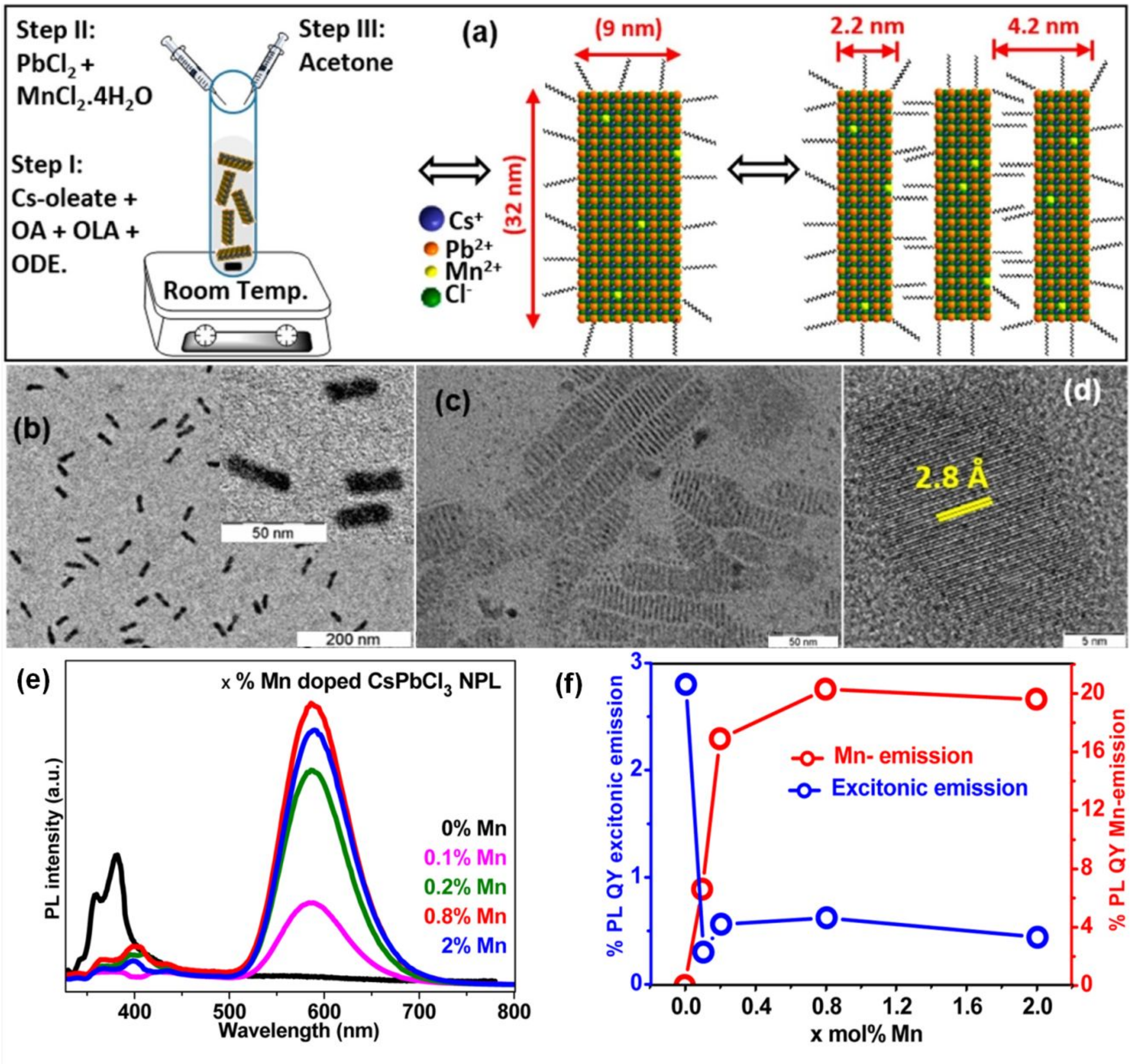

Figure 16. (a) Schematic representations of synthesis and morphology of 0.8% Mn-doped $CsPbCl_3$ nanoplatelets, which can undergo face-to-face self-assembly. OA, OLA, and ODE refer to oleic acid, oleylamine, and 1-octadecene, respectively. (b) TEM image of nanoplatelets lying flat on the TEM grid. Inset shows a magnified view. (c) TEM image of self-assembled nanoplatelets lying perpendicular to the TEM grid. (d) HRTEM image

illustrating lattice fringes for nanoplatelets lying flat on the TEM grid. (e) PL spectra as a function of Mn doping concentration, where absorbance at excitation wavelength for all samples was maintained the same. (f) PLQY for excitonic and Mn emission as a function of Mn doping concentration, where open circles are data points and solid lines are just a guide to the eye. Reprinted with permission from Ref. [269], copyright 2017, American Chemistry Society.

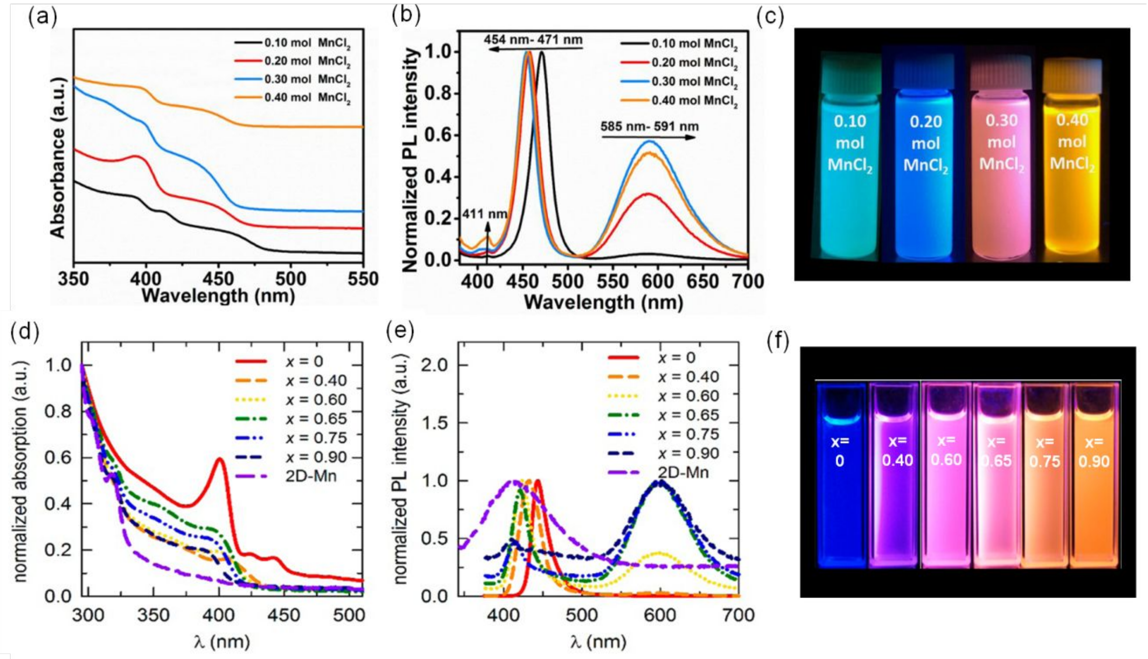

Figure 17. (a) UV−vis absorption and (b) PL spectra of Mn-doped $CsPbBr_3$ perovskite magic sized clusters (PMSCs) and PQDs prepared using 0.10, 0.20, 0.30, and 0.40 mol of $MnCl_2{\cdot}4H_2O$. (c) Photograph of the Mn-doped $CsPbBr_3$ PMSCs and perovskite quantum dots (PQDs) samples synthesized with 0.10, 0.20, 0.30, and 0.40 mol of $MnCl_2{\cdot}4H_2O$ in toluene under UV irradiation (λex = 365 nm). Reprinted with permission from Ref. [272], copyright 2020, American Chemistry Society. Optical properties of 3-D $MAPb_{1-x}Mn_xBr_{3-(2x+1)}Cl_{2x+1}$ nanocrystals with various Mn doping content (x) and 2-D $(MA)_2MnCl_4$ (2D-Mn) nanocrystals with 100% Mn: (d) Absorption spectra normalized at 295 nm and (e) normalized PL spectra excited at 365 nm, except for 2-D $(MA)_2MnCl_4$ which was excited at 308 nm. The highest emission intensity among the exciton and Mn^{2+}

peaks was used for normalization. For x ≤ 0.6, exciton emission peaks were used for normalization; while for x > 0.6, Mn^{2+} emissions were used. The 2-D $(MA)_2MnCl_4$ emission was normalized at its emission maximum of 410 nm. (f) Photographs of the corresponding Mn-doped nanocrystals under 365 nm UV light illumination. Reprinted with permission from Ref. [284], copyright 2017, American Chemistry Society.

In addition to the Mn-doped $CsPbCl_3$ and Mn-doped $CsPb(Cl/Br)_3$ noted above, Mn-doped organic-inorganic hybrid lead halide perovskites ($MAPbX_3$, X =Cl, Br, I) have also been achieved. Interestingly, all examples of Mn-doped organic-inorganic hybrid lead halide perovskites are based on room temperature synthesis approaches. [258, 284, 285] It was also interesting to note that the Mn doping ratio in the $MAPbCl_3$ and $MAPb(Br/Cl)_3$ systems can be significantly higher than that of the Mn-doped $CsPbCl_3$ and $CsPb(Br/Cl)_3$ systems. The highest Mn doping ratio in $CsPbCl_3$ and $CsPb(Br/Cl)_3$ systems is 46%, while Mn doping ratio in $MAPbCl_3$ and $MAPb(Br/Cl)_3$ systems can reach as high as 90% (Figure 17d-17f). [284, 285] The stark difference in the possible doping ratios of all-inorganic and organic-inorganic hybrid perovskites is attributed to the flexibility of the organic cation ($CH_3NH_3^+$) network which can preserve perovskite structure better than the rigid inorganic cation (Cs^+). [284] It was found that 90% Mn-doping is roughly the solubility limit, and further inclusion of Mn to 100% will result in the formation of 2-D $(MA)_2MnCl_4$ instead of 3-D $MAMnCl_3$. The transition is said to occur because Mn is smaller than Pb, and complete substitution will result in an unstable octahedral factor (μ) of less than 0.40. [284] Due to limited space, many papers regarding Mn-doped perovskite nanocrystals are not covered in this review. [286-293] You may refer to a recent review for a more comprehensive insight into Mn-doped perovskite nanocrystals. [294]

3-3. Lanthanide-based (Trivalent Substitution) Perovskite Nanocrystals

Rare-earth element lanthanide ions have widely been used to dope phosphors like Ce^{3+}-doped $Y_3Al_5O_{12}$ (cerium-doped yttrium aluminum garnet, YAG:Ce), [295, 296] and up-conversion nanoparticles such as Yb^{3+}, Er^{3+} co-doped $KMnF_3$ ($KMnF_3$:Yb,Er) [297, 298] and $NaYF_4$ ($NaYF_4$:Yb,Er) [299-301]. The radius of Ce^{3+} is similar to that of Pb^{2+} (103 pm and 119 pm for Ce^{3+} and Pb^{2+}, respectively) [302] and has been doped in KPb_2Cl_5 and KPb_2Br_5 ternary lead halides. [303] $CeBr_3$ salt has been incorporated with hot-injection method to successfully dope Ce^{3+} into $CsPbBr_3$ nanocrystals, resulting in an improved PLQY. [302] Modified hot injection has also lead to successful lanthanide doping in Ce^{3+},Yb^{3+} co-doped $CsPbCl_{1.5}Br_{1.5}$ and Yb^{3+},Er^{3+} co-doped $CsPbCl_{1.5}Br_{1.5}$ nanocrystals. Ce^{3+},Yb^{3+} co-doped $CsPbCl_{1.5}Br_{1.5}$ ($CsPbCl_{1.5}Br_{1.5}$:Yb(7.1%),Ce(2%)) nanocrystals show a significantly high PLQY of 146% and a large absorption cross-section, which make them prime candidates for downconversion material. [304] The PLQY can exceed 100% through a mechanism called the quantum-cutting effect, where one absorbed high-energy photon can downconvert into two emitting low-energy photons. [305] When the two photons are emitted at a wavelength far away from their absorption edge (which means with large Stokes shift), the self-absorption loss can be eliminated and the PLQY can be doubled. Yb^{3+}-doped $CsPbCl_3$ nanocrystals synthesized via hot injection method have successfully demonstrated PLQY of 170% (close to the theoretical quantum-cutting limit of 200%), because they have emission in the NIR (~1000 nm) range while their absorption is in the near UV (~400 nm) range. [306] It is proposed that the aliovalent Yb^{3+} dopants tend to form a cation vacancy charge-neutral defect complex ($Yb^{3+}-V_{Pb}-Yb^{3+}$), which facilitates trapping the excitation energy from the $CsPbCl_3$ host (therefore almost no excitonic luminescence near absorption edge can be found). The trapped excitation energy is then divided to excite the two neighboring Yb^{3+} dopants followed by luminescent $^2F_{5/2} \rightarrow {}^2F_{7/2}$ f−f transitions of Yb^{3+} ions resulting in quantum-cutting NIR emission with PLQY approaching 200%. [306-309] Density functional theory (DFT) calculation demonstrats that the charge-neutral $Yb^{3+}-V_{Pb}-Yb^{3+}$ complex does not create an inter-bandgap defect energy level, and therefore different from the previous proposal, the energy donor in the quantum cutting process is actually the "right-angle" Pb atom rather than the Yb^{3+}-induced defect. [310] Yb^{3+} doping can also be achieved via postsynthesis exchange using $Yb(NO_3)_3 \cdot 5H_2O$ in a mixture of methyl acetate:toluene (1:3 v/v) as precursor. [311] In order to see the quantum-cutting mechanism of $^2F_{5/2} \rightarrow {}^2F_{7/2}$ f−f transitions, a fundamental energy-conservation threshold of $Eg > 2\times E_{f-f}$ must exist, meaning that the absorption band gap of perovskite host must be adequately large. When continuously decreasing the band gap by tuning the x value from 0 to 1 in Yb^{3+}-doped $CsPb(Cl_{1-x}Br_x)_3$ nanocrystals, quantum-cutting effect can be retained for x values as large as ~0.75 then a steep drop of PLQY is observed with larger x values. [312] It has been proposed that the formation of a higher-concentration of defects can facilitate the introduction of a higher-concentration of Yb^{3+} dopant ions. [313] Yb^{3+}-doped $Cs_2AgInCl_6$ and Cs_2AgBiX_6 (X= Cl, Br) double perovskite nanocrystals also exhibit NIR emission at ~1000 nm. [281, 314] Although Yb^{3+}-doped perovskite nanocrystals can show PLQY approaching 200% due to quantum cutting process, there is still obstacles preventing them from practical use as solar downconversion materials due to their PL power saturation under modest photoexcitation fluences. [315] Eu^{3+}-doped $CsPbBr_3$ and Tb^{3+}-doped $CsPbBr_3$ nanocrystals have been synthesized using a one-pot ultrasonication method. [316] Various of lanthanide ions (Ce^{3+}, Sm^{3+}, Eu^{3+}, Tb^{3+}, Dy^{3+}, Er^{3+}, and Yb^{3+}) have been systematically studied and successfully doped into the lattices of $CsPbCl_3$ perovskite nanocrystals through a modified hot-injection method using the corresponding lanthanide chloride salts as doping precursors. [317] From the absorption spectra (Figure 18a), it was found that as the atomic number of the lanthanide ion increased, the band gap of the host perovskite nanocrystals gradually blue-shifted due to lattice contraction, which is in good agreement with common band gap engineering literature. [317] In the emission spectra (Figure 18b), several peaks associated with the intrinsic electronic transitions of lanthanide ions can be found in the doped systems besides the narrow band-edge emission peak at around 410 nm. The overall PLQY of doped systems is enhanced mainly due to the contribution of intrinsic emissions from the lanthanide ions. Although the energy transfer from exciton of perovskite host to doping ions likely decreases the PLQY of the exciton, some nonradiative recombination pathways (such as Cl vacancy) may be removed during the doping and result in enhanced PLQY of exciton. [317] $LiYbF_4:Tm^{3+}@LiYF_4$ core/shell nanoparticles were used to sensitize $CsPbX_3$ perovskite nanocrystals in order to achieve upconversion luminescence (UCL) through a radiative energy transfer upconversion (RETU) process. Lanthanide-doped core/shell nanoparticles function as the energy donor to convert the NIR excitation light into the UV and visible emission light through successive photon absorption and energy transfer upconversion (ETU) processes, then the emitted light from nanoparticles will be reabsorbed by perovskite nanocrystals. [318] Bright blue light-emitting CsBr lead-free nanocrystals doped with Eu^{2+} have been achieved through hot-injection method. [319] We note that discussion on a few more lanthanide-doped perovskite nanocrystals studies can be found in this review. [320]

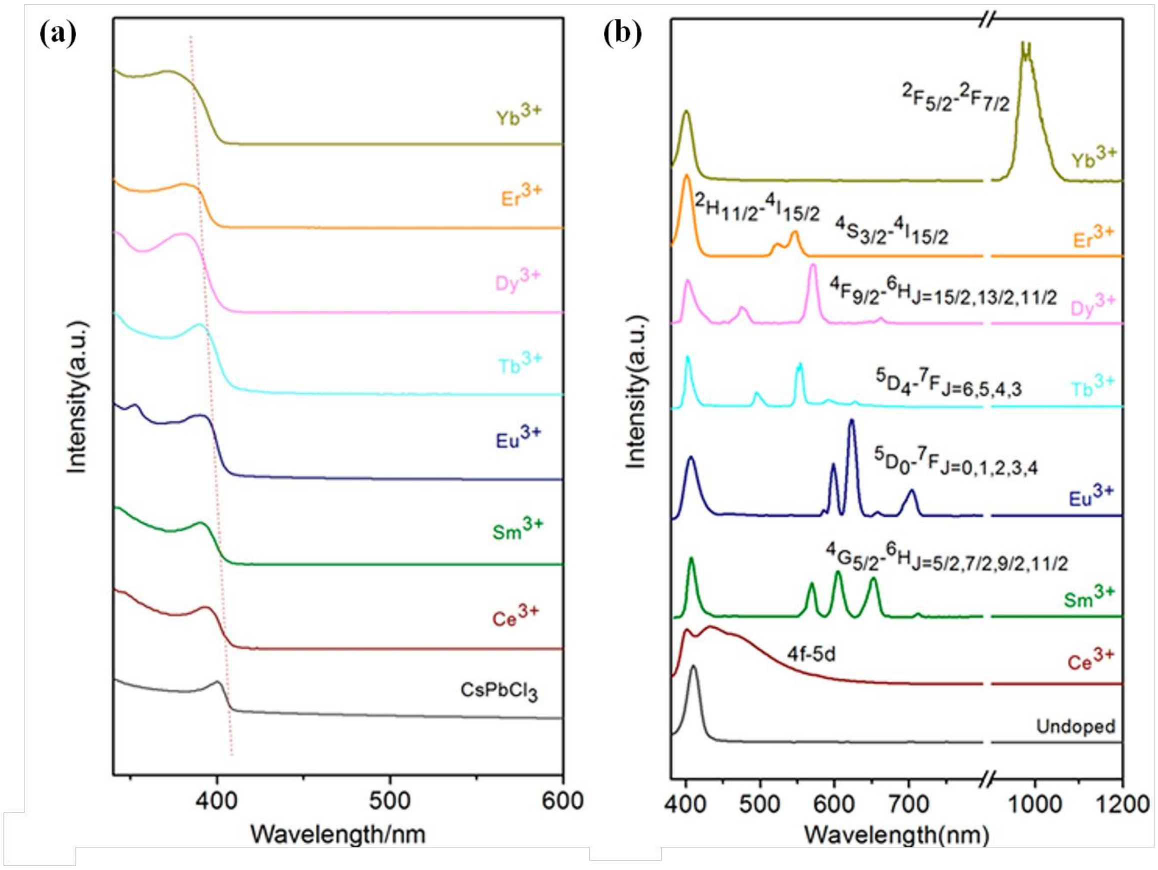

Figure 18. Absorption spectra and (b) PL emission spectra of $CsPbCl_3$ nanocrystals doped with different lanthanide ions. Reprinted with permission from Ref. [317], copyright 2017, American Chemistry Society.

3-4. Au (Au(0), Au(I), Au(II), Au(III)) and Ag-based Perovskite Nanocrystals

Interesting combinations can be observed when incorporating Au into perovskite systems due to the different valence charge states in gold systems. $Cs_2[Au^IX_2][Au^{III}Y_4]$ (X, Y = halogen) gold mixed-valence complexes with mono-halogen (X=Y, i.e., $Cs_2Au_2X_6$)

[321] or hetero-halogen (X≠Y) [322] with distorted perovskite structures have both been achieved. [323] The perovskite-type gold mixed-valence systems undergo either pressure-induced or photo-induced Au valence transition from the mixed-valence state of $Au^{I,III}$ to the single-valence state of Au^{II}. The electrical properties of mixed-valence $Au^{I,III}$ complexes are attributed to the mobility of bipolarons, the dynamic two-electron exchange between the Au^{I} and Au^{III} states, and can behave as either an insulator or metal, depending on pressure or temperature. [321-323] Although the distorted perovskite structures of these $Cs_2[Au^{I}X_2][Au^{III}Y_4]$ complexes are three-dimensional, the charge transfer interaction between Au^{I} and Au^{III} within these complexes is two-dimensional through the bridging halogen Y, which sits in the a-b plane. Because the bridging halogen Y is responsible for controlling the pressure-induced gold valence transition in the $Cs_2[Au^{I}X_2][Au^{III}Y_4]$ complexes, the critical pressure for the valence transition from $Au^{I,III}$ to Au^{II} is distinct for different halogen systems. [322, 323] Besides the Au(I)/Au(III) and Au(II) states mentioned above, Au can also be incorporated into perovskite systems through Au(0) state. [324] When introducing $AuBr_3$ into a $CsPbBr_3$ nanocrystal/toluene solution, gold nanoparticles can spontaneously form at the edge of $CsPbBr_3$ nanocrystals (Figure 19a and 19b, from (1) $CsPbBr_3$ to (2) Au-$CsPbBr_3$). If $AuCl_3$ is introduced to $CsPbBr_3$ nanocrystals, gold nanoparticles will again form on their surface, and an anion exchange process forming Au-$CsPb(Br_{1-x}Cl_x)_3$ nanocrystals will occur (Figure 19a and 19b, from (1) $CsPbBr_3$ to (3) Au-$CsPb(Br_{1-x}Cl_x)_3$). It was proposed that the Au(III) ions can be reduced into Au(0) by the oleylamine on the surface of $CsPbBr_3$ nanocrystals, and subsequently nucleate and grow into Au nanoparticles on the corners of perovskite nanocrystals, without the assistance of any additional reducing agent (Figure 19b). [324] The PLQY of the nanocrystals is decreased when Au-$CsPbBr_3$ or Au-$CsPb(Br_{1-x}Cl_x)_3$ hybrid structures are formed suggesting that there is a charge-transfer process between the perovskite nanocrystal and the Au nanoparticles. [324] Another study suggested that the formation of Au-$CsPbBr_3$ hybrid structures may not always occur and sometimes a cation exchange process between Au ions and Pb ions may form $Cs_2Au^{I}Au^{III}Br_6$ nanocrystals, which have absorption in the NIR range (Figure 19c-19f). [325] By introducing some $PbBr_2$ salts at the same time as adding $AuBr_3$ crystals, the existence of excess Pb ions competitively prevents the cation exchange of Au ions for Pb ions and insures there is no formation of

$Cs_2Au^{I}Au^{III}Br_6$ nanocrystals (Figure 19c-19f, from (4) $CsPbBr_3$ to (6) Au-$CsPbBr_3$). The diameter of the deposited Au nanoparticles can be tuned by the concentration of additional Au(III) ions. The formation of $Cs_2Au^{I}Au^{III}Br_6$ nanocrystals can be considered an alternative synthetic strategy for Pb-free perovskites via a postsynthetic cation exchange process. The formation of Au-$CsPbBr_3$ hybrid nanocrystals can provide improved catalytic activity due to the plasmon-exciton coupling effect and the metal domains of Au-$CsPbBr_3$ hybrid heterostructures can act as electrical contact points for nanoscale optoelectronic devices. [325] Silver ions (Ag^+) have also been proposed to heterovalently dope colloidal $CsPbBr_3$ nanocrystals via substituting Pb^{2+} ions and significantly improve the conductivity and charge-carrier mobility by nearly 3 orders of magnitude. Heterovalent doping of Ag^+ has been found to shift the Fermi level downward to the valence band and induce a p-type character in Ag^+-doped $CsPbBr_3$ nanocrystals and significantly improve the conductivity and charge-carrier mobility by nearly 3 orders of magnitude compared to the undoped $CsPbBr_3$ nanocrystals, confirmed by field effect transistor (FET) studies. [326] In another study, however, Ag^+ ions were proposed to replace Cs^+ ions instead of Pb^{2+} ions and claimed to simultaneous dope and surface passivate the $CsPbI_3$ nanocrystals film in LED device. [327]

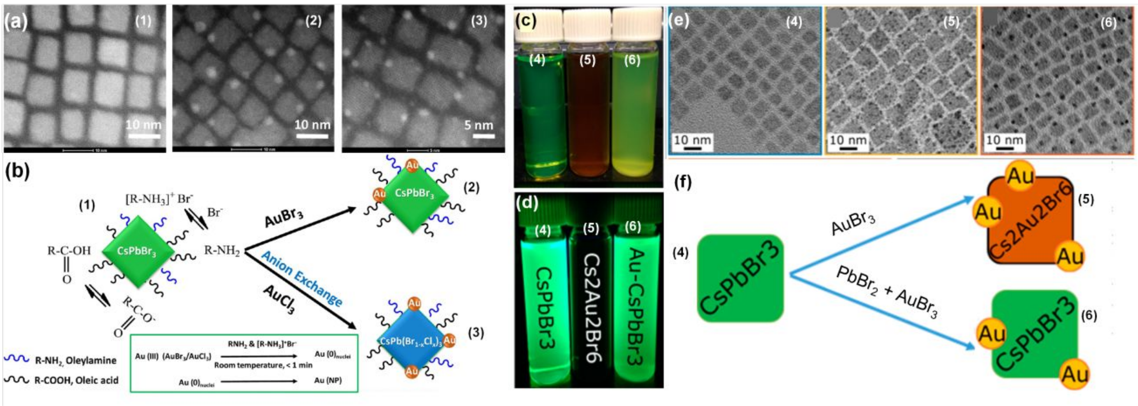

Figure 19. (a) High-resolution scanning transmission electron microscopy (HR-STEM) images of (1) parent $CsPbBr_3$ nanocrystals, and (2) Au-$CsPbBr_3$ or (3) Au-$CsPb(Br_{1-x}Cl_x)_3$ hybrid structures after reactions. (b) Schematics of surface amine ligands reacting with the additional $AuBr_3$ (or $AuCl_3$) salts leading to the reduction of Au(III) to Au(0), forming Au

nanoparticles at the edge of $CsPbBr_3$ (or $CsPb(Br_{1-x}Cl_x)_3$, due to the accompanied anion exchange when adding $AuCl_3$ salts) nanocrystal. Reprinted with permission from Ref. [324], copyright 2017, American Chemistry Society. Photographs of (4) $CsPbBr_3$, (5) $Cs_2Au_2Br_6$, and (6) Au-$CsPbBr_3$ nanocrystal solutions under (c) ambient light and (d) UV light excitation, and (e) their corresponding TEM images. (f) Schematics of (4) $CsPbBr_3$ nanocrystals reacting with $AuBr_3$ forming (5) $Cs_2Au_2Br_6$ nanocrystals (gold cation exchange accompanied with some gold deposition) or (6) Au-$CsPbBr_3$ nanocrystals (purely gold deposition, the existence of excess Pb ions from added $PbBr_2$ can competitively prevent the gold cation exchange from ocurring). Reprinted with permission from Ref. [325], copyright 2017, American Chemistry Society.

3-5. Other Divalent (Isovalent) Substitution Perovskite Nanocrystals

Other than the widely studied Sn-doped and Mn-doped systems, a few other divalent cations have also been tested in doping colloidal metal halide perovskite nanocrystals. Alkaline-earth (AE) metals (e.g., Mg^{2+}, Ca^{2+}, Sr^{2+}, and Ba^{2+}) have been proposed to be used as dopants to substitute Pb^{2+} in halide perovskites through a one-pot synthetic method. [328] AE metal chloride (i.e., $MgCl_2$, $CaCl_2$, $SrCl_2$, and $BaCl_2$) were added to the other precursors during synthesis of $CsPbCl_3$ perovskite nanocrystals, and it was found that the incorporation effectiveness of AE^{2+} ions in $CsPbCl_3$ nanocrystals are quite different. It was found that only Ba^{2+} can be incorporated into the core of nanocrystals, while Ca^{2+} and Sr^{2+} stay at/near the surface of nanocrystals, passivating the nonradiative recombination surface vacancies and significantly enhancing PLQY (pristine $CsPbCl_3$: 0.8%; Ca^{2+}-doped $CsPbCl_3$: 77.1%). Mg^{2+} found to rarely incorporate into the nanocrystals, neither in the core nor at the surface, probably due to its relatively small ionic radius (ionic radius (Å): Mg^{2+}=0.72, Ca^{2+}=1.00, Sr^{2+}=1.18, Ba^{2+}=1.35, Pb^{2+}=1.19), which results in a notable self-purification effect that excludes Mg^{2+} outside the lattice. [328] $SrCl_2$ has also been used as a co-precursor during $CsPbI_3$ nanocrystals synthesis to simultaneously dope Sr^{2+} ions and passivate the surface with Cl^- ions. Because Sr^{2+} has a smaller ionic radius (1.18 Å) than Pb^{2+} (1.19 Å), it can cause a slight contraction in $CsPbI_3$ lattice, resulting in improved stability. At the same time, Cl^- ions can passivate surface defects of $CsPbI_3$

nanocrystals, resulting in enhanced PL. [329] SrI_2 has also been used to stabilize cubic phase α-$CsPbI_3$ nanocrystals, and a high PLQY of 80% can be maintained even after storage for two months. [330] Ni^{2+}, with the smallest ionic and Shannon radii among all transition metal ions, has been used to dope $CsPbI_3$, $CsPbBr_3$, and $CsPbCl_3$ nanocrystals using NiI_2, $NiBr_2$, and $NiCl_2$ as precursors, respectively. [208, 331-334] It was found that Ni^{2+} doping can restrict the phase change of $CsPbI_3$ nanocrystals from α-$CsPbI_3$ to δ-$CsPbI_3$ and significantly improve their stability. [331] While violet emitting $CsPbCl_3$ nanocrystals usually have relatively low PLQYs (<5%), [335] Ni^{2+} doping was found to boost the PLQY of violet emitting $CsPbCl_3$ nanocrystals from 2.4% up to 96.5%. [333] Similarly, postsynthetic treatment of $CsPbCl_3$ nanocrystals using $CdCl_2$ can also boost the PLQY of violet emitting $CsPbCl_3$ nanocrystals from 3% up to 96±2% and maintain its original PL peak position (406 nm) and peak width (FWHM ~10−12 nm). [336] By adding optimum amount of $CuCl_2$ during hot-injection synthesis of $CsPbCl_3$ nanocrystals, the PLQY of violet-emitting $CsPbCl_3$ nanocrystals can be boosted from ~0.5% to 60% with an emission peak position (λ_{em}) at 403 nm, and the PLQY of halide-exchanged $CsPb(Cl/Br)_3$ can be boosted from ~8% to ~92% (for sample with λ_{em} = 430 nm) and from 22% to 98% (for sample with λ_{em} = 460 nm). [335] All the abovementioned Ni, Cd, and Cu-doped $CsPbCl_3$ and $CsPb(Cl/Br)_3$ nanocrystals exhibit no blue shift in the PL peak position, even though one would be expected from lattice contraction associated with the incorporation of relatively smaller Ni^{2+}, Cd^{2+}, and Cu^{2+} ions. One study demonstrated, however, that doping smaller Cu^{2+} ions can boost the PLQY of $CsPb(Br/Cl)_3$ nanocrystals from 23% to 80% but would also blue shift the wavelength from 466 nm to 453 nm. [337] It has been demonstrated that $CsPbCl_3$ nanocrystals only experience a massive boost in PLQY when treated with $Cu(II)X_2$ precursors (when treated with $CuCl_2$ or $CuBr_2$, the PLQY of $CsPbCl_3$ can be boosted from 2.7% to 12.3% ($CuCl_2$ treatment) and 92.6% ($CuBr_2$ treatment)), and not when treated with Cu(I)X precursors (when treated with CuCl or CuBr the PLQY of $CsPbCl_3$ showed improvements of only 2.7% (CuCl treatment) and 22.3% (CuBr treatment)). [338] Simply by increasing the Cu doping concentration, the emission wavelength of $MAPb_{1-x}Cu_xBr_3$ can be tuned from 468 nm to 513 nm. [339] Co^{2+} doping in $CsPbBr_3/Cs_4PbBr_6$ nanocrystals can lead to effective catalytic sites for CO_2 reduction. [80] Partial substitution of Pb^{2+} with Zn^{2+} in $CsPbI_3$ perovskite nanocrystals exhibited an improved, close-to-unity PLQY of 98.5% due to the increased radiative decay rate and decreased non-radiative decay rate. [340] A postsynthetic cation exchange method was used to dope $CsPbBr_3$ nanocrystals with metal(II) ions by dissolving metal(II) bromide salts ($MBr_2 = SnBr_2$, $CdBr_2$, $ZnBr_2$) in oleylamine and adding it to a perovskite nanocrystal-toluene solution at room temperature inside a nitrogen-purged glovebox. [227] Using metal(II) bromide salts ensures that no anion exchange occurs and any change is solely coming from cation exchange. Blue-shifted absorption and PL spectra were observed in all three cases (Figure 20), but the blue-shift behaviors vary from case to case and strongly depend on the precursor concentration and the type of divalent cation. For the case of postsynthetic reaction with $SnBr_2$, the blue-shift is small for both low and high $SnBr_2$ concentrations. Postsynthetic reactions with $CdBr_2$ and $ZnBr_2$ lead to more pronounced blue-shifts than those seen with $SnBr_2$. The size, shape, high PLQYs (over 60%), and colloidal stability in toluene of parent $CsPbBr_3$ nanocrystals were maintained for at least several months after the reactions with metal(II) bromide salts. 1D powder electron diffraction (PED) patterns (obtained by azimuthally integrating the 2D electron diffraction (ED) patterns) show that the lattice contracts more after reaction with $CdBr_2$ and $ZnBr_2$ salts than with $SnBr_2$ (Figure 20f and 20g). This is expected due to the differences in the ionic radii ($r(Pb^{2+}) = 119$ pm, $r(Sn^{2+}) = 118$ pm, $r(Cd^{2+}) = 95$ pm, $r(Zn^{2+}) = 74$ pm, and coordination number (CN) = 6 in all cases). [227] The cation exchange process is often limited by the diffusion rates of the outgoing and incoming cations, which is often attributed to vacancy-mediated migration which is limited by the formation energy of each vacancy. Cation diffusion in perovskites is relatively much slower than that of anions because cations have higher activation energies and lack of interstitial sites for interstitial diffusion. Therefore, the postsynthetic cation exchange in this study is very slow and only partially occurs despite the large excess amount of M^{2+} cations used. It was suggested that the amount of oleylamine added also plays an important role in the ion exchange process because the amount of oleylamine (OLAM) will affect the amount of OLAM-Br complex (between both host perovskite and MBr_2 dopant) and that strongly affects the number of halide vacancy generated (Figure 21). [227] We note that the abbreviation for oleylamine in the whole paper is not consistent due to the different abbreviations used in different schematic figures. Transition metal halides (FeX_3, CoX_2, NiX_2, CuX_2, and ZnX_2) have also been used to dope $CsPbX_3$ nanocrystals. [341] Similary, metal(II) bromide salts (MBr_2 = $ZnBr_2$, $MnBr_2$, $EuBr_2$) have been used to convert Cs_4PbBr_6 nanocrystals into $CsPb_xM_{1-x}Br_3$ nanocrystals, [342] following an earlier finding that excess $PbBr_2$ would transform Cs_4PbBr_6 nanocrystals into $CsPbBr_3$ nanocrystals. [343]

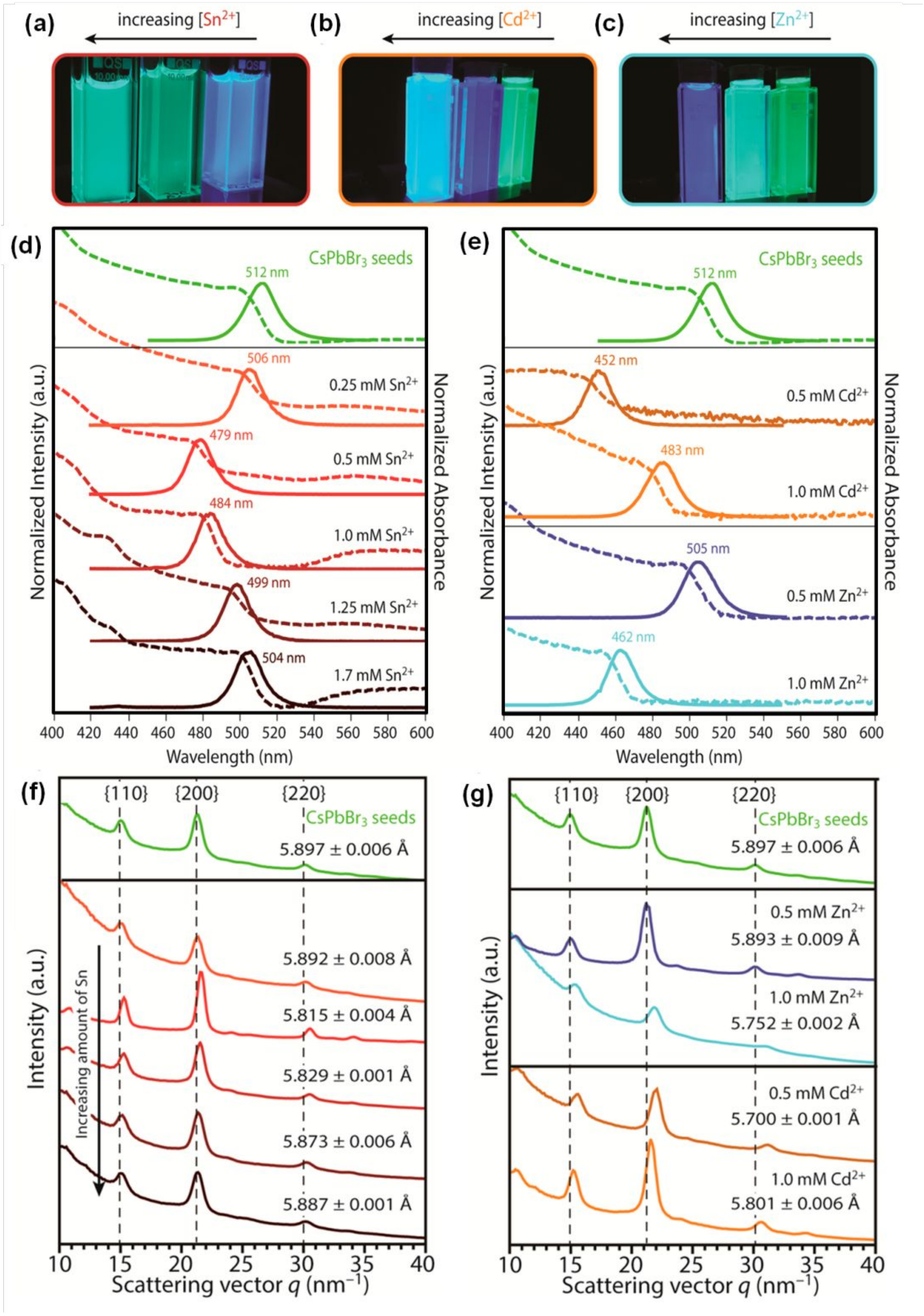

Figure 20. Photographs of colloidal suspensions of $CsPbBr_3$ nanocrystals upon reaction with different divalent cation bromide salts under UV illumination: (a) $CsPbBr_3$ nanocrystals after reaction with different concentrations of $SnBr_2$ (from right to left: 0.5, 1.25, and 1.7 mM), (b) parent $CsPbBr_3$ nanocrystals (right vial) and product nanocrystals after reaction with different concentrations of $CdBr_2$ (0.5 mM (middle vial) and 1.0 mM (left vial)), and (c) parent $CsPbBr_3$ nanocrystals (right vial) and product nanocrystals after reaction with different concentrations of $ZnBr_2$ (0.5 mM (middle vial) and 1.0 mM (left vial)). PL spectra (solid lines) and absorption spectra (dashed lines) of (d) parent $CsPbBr_3$ nanocrystals (green lines) and product nanocrystals obtained after reaction with different concentrations of $SnBr_2$ (red and brown lines) and (e) parent $CsPbBr_3$ nanocrystals (green lines) and product nanocrystals obtained after reaction with different concentrations of $CdBr_2$ (orange lines) and $ZnBr_2$ (blue lines). In all cases, a blue-shift of both the absorption and the PL emission spectra is observed after reacting $CsPbBr_3$ nanocrystals with divalent cation bromides (MBr_2), while the well-defined absorption features and narrow PL FWHMs (~80 meV) are preserved. 1D powder electron diffraction (PED) patterns of $CsPbBr_3$ nanocrystals after reaction with MBr_2 obtained from azimuthal integration of 2D electron diffraction (ED) patterns: (f) after reaction with $SnBr_2$ with concentration of 0.25, 0.50, 1.0, 1.25, and 1.7 mM, from top to bottom, respectively, show minor lattice contraction; whereas (g) after reaction with 0.50 and 1.0 mM of $ZnBr_2$ and $CdBr_2$ show larger lattice contraction. Reprinted with permission from Ref. [227], copyright 2017, American Chemistry Society.

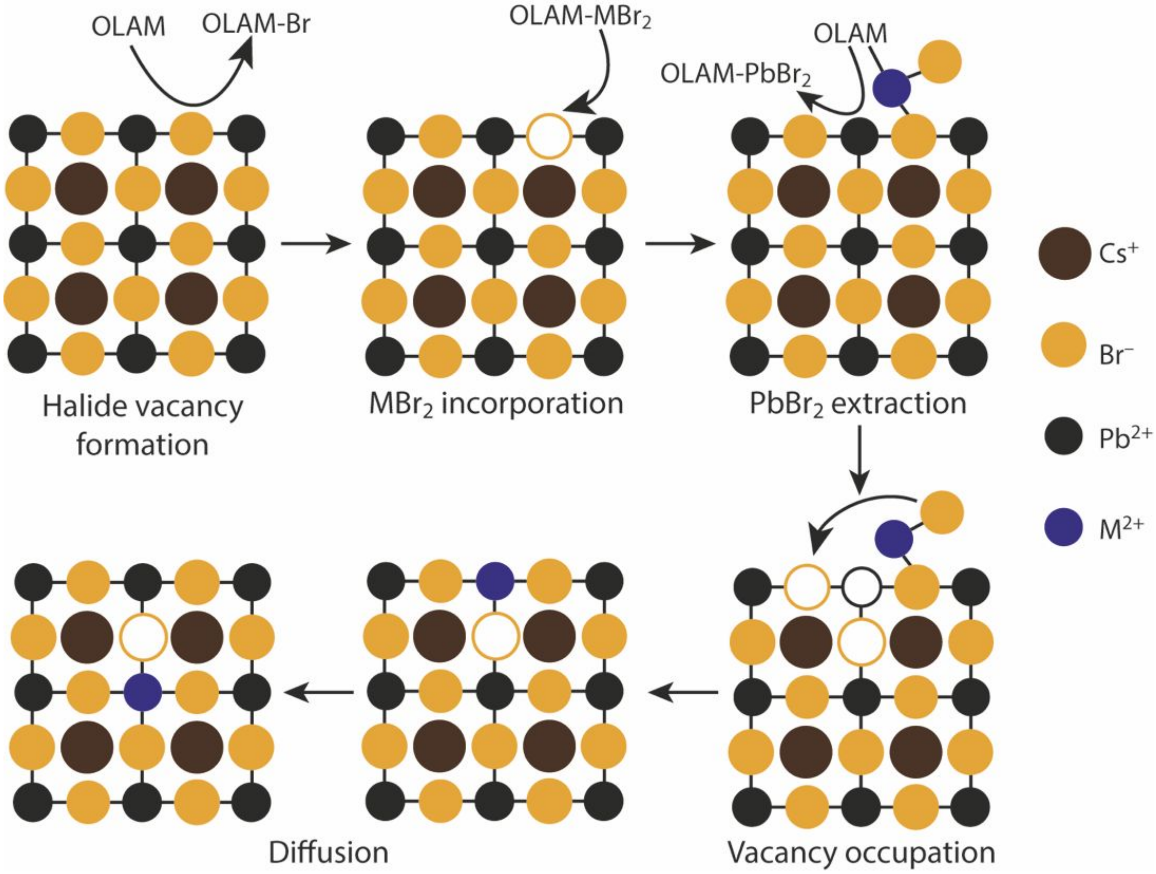

Figure 21. "Schematic representation of the proposed cation exchange reaction mechanism. In the first step, surface halide vacancies are created by oleylamine (OLAM) molecules in solution. In the second step, a Br anion of an OLAM-MBr_2 unit occupies the halide vacancy. In a third step, the bound OLAM molecule extract a $PbBr_2$ unit, leaving a cation and halide vacancy behind, which are occupied by the bound MBr_2 species. Finally, the incorporated divalent guest cation diffuses into the perovskite lattice, leaving behind a halide vacancy at the surface for a second cation exchange process to occur." Reprinted with permission from Ref. [227], copyright 2017, American Chemistry Society.

3-6. Other Trivalent (Heterovalent) Substitution Perovskite Nanocrystals

Scientists have also considering doping Bi to replace Pb because Bi^{3+} and Pb^{2+} are isoelectronic (i.e., both electron configurations are the same as $[Xe]4f^{14}5d^{10}6s^{2}6p^{0}$). Incorporating heterovalent Bi^{3+} ions may induce electronic doping (act as electron donor) by increasing the charge carrier density in the lead halide perovskites. Doping heterovalent Bi^{3+} ions in colloidal $CsPbBr_3$ perovskite nanocrystals has been achieved by hot-injection method with a combination of $BiBr_3$, $PbBr_2$, and Cs-oleate (Figure 22A−D). [344] Through the use of Kelvin Probe, time-resolved transient absorption, and photoemission spectroscopy in air (PESA), it was demonstrated that Bi^{3+} doping not only affects the band structure and carrier dynamics of $CsPbBr_3$, but also the interfacial charge transfer between Bi-doped $CsPbBr_3$ and two well-known molecular electron acceptors, tetracyanoethylene (TCNE) and phenyl-C_{61}-butyric acid methyl ester ($PC_{61}BM$). [344] The driving-force of interfacial charge transport, Gibbs free energy ($-\Delta G$) between the molecular acceptor and donor moieties, can be tuned upon metal doping. [344] Interestingly, band gap broadening (blue-shift) was found in the Bi-doped $CsPbBr_3$ nanocrystals (Figure 22C), and band gap narrowing (red-shift) was found in most Bi-doped single crystal cases including Bi-doped $CsPbBr_3$ (Figure 22F), [345] Bi-doped $MAPbBr_3$, [346] and Bi-doped $MAPbCl_3$ single crystals [347]. One study claimed Bi-doping had no effect on the band gap of Bi-doped $MAPbBr_3$ single crystals, but instead significantly increases the sub-band gap density of states, which other studies incorrectly interpreted as band gap narrowing. [348] Though the effect of band gap narrowing or broadening is contradictory to each other in the single crystal and nanocrystal cases, there is no doubt that Bi-doping can affect the electronic properties of the host crystals. By sandwiching a ~2 mm thick Bi-doped perovskite single crystal in between two ~100 nm thick Au electrodes, the metal-semiconductor-metal configuration demonstrated current−voltage (I−V) characteristics of an Ohmic contact for the undoped single crystal (e.g., $CsPbBr_3$ [345] or $MAPbCl_3$ [347]), and showed that conductivity increased with Bi-doping content, probably due to higher carrier concentration and alteration of the metal-semiconductor band alignment. [345] High-level DFT calculations demonstrate that replacing Pb^{2+} with Bi^{3+} ions in the bulk or on the surface creates deep trap states that remove the defect-tolerant nature of $CsPbBr_3$ nanocrystals and function as nonradiative recombination centers significantly quenching the PL intensity. Conversely, Ce^{3+} ions can stabilize the bulk/surface structure of $CsPbBr_3$ nanocrystals providing band-edge states that leads to PL enhancement. [349] Besides Bi^{3+}, a few other trivalent ions have been examined as heterovalent dopants in lead halide perovskite systems. Sb^{3+} doping in super small blue emitting $CsPbBr_3$ nanocrystals is suggested to reduce the surface energy, improve the lattice energy, passivate the defect states below the band gap, and boosting their blue emitting PLQY from 50.0% to 73.8%. [350] Au^{3+} and In^{3+} have been successfully incorporated into $MAPbBr_3$ single crystals by the addition of $AuBr_3$ and $InBr_3$ salts, however they did not exhibit significant spectral changes (band gap narrowing). [346] They suggested that the outer ns^2 electrons play a critical role in band gap modulation and density functional theory (DFT) calculations also suggested that Au and In create deeper, more localized states than Bi. [346] Al^{3+} has been successfully incorporated in $CsPbBr_3$ nanocrystals by the addition of $AlBr_3$ salt, and a blue-shift in the emission was observed. [351] They suggested that the blue-shifted emission was due to the extended band gap of Al-doped nanocrystals as well as the quantum confinement effect originating from the elongated shape of Al-doped nanocrystals. The bond dissociation energy of Al_2Br_6 (the dimeric form of $AlBr_3$) needs to be considered during the incorporation because of the possibility of retention of some Al–Br (bridging) bonds. [351] The introduction of foreign Bi^{3+}, Al^{3+}, and In^{3+} ions to $CsPbBr_3$ nanocrystals by adding $BiBr_3$, $BiFeO_3$, $BiCl_3$, $AlBr_3$ or $InBr_3$ into the synthesis precursors will function as capping ligands and led to partial formation of growth-constrained thinner perovskite nanoplatelets with a thickness of 3 inorganic $PbBr_4^{2-}$ octahedron layers. The final products will be a mixture nanoplateles with two different thicknesses, as seen by two well-defined absorption and emission bands. [352] Fe(II)-doped $CsPbBr_3$ nanocrystals can be efficient photocatalysts for reduction of CO_2 without the need of any additional carrier transportation material or heterostructures. During photocatalytic reduction of CO_2, undoped $CsPbBr_3$ led to CO as the major product while Fe(II)-doped $CsPbBr_3$ led to CH_4 as the dominant product. [82] Fe(III)-doped $CsPbCl_3$ nanocrystals shows a pink-colored dual emission consisting of a sharp blue emission at 410 nm from the excitonic peak of $CsPbCl_3$ and a broad red emission at ~580 nm result from the $^4T_1 \rightarrow {}^6A_1$ (d−d) radiative transition of Fe^{3+} dopant. [353] Gadolinium (Gd^{3+}) doping was found to enhance the phase stability of α-$CsPbI_3$ nanocrystals from 5 days to 11 days probably due to the reasons of increased tolerance factor, distorted cubic symmetry, and decreased defect density. [354]

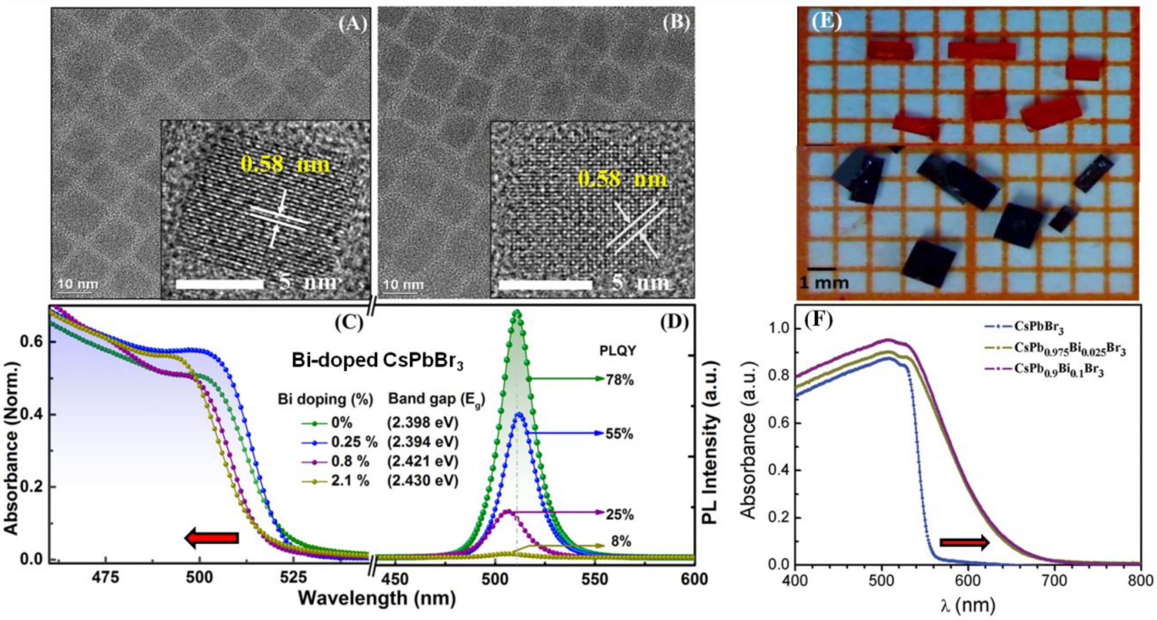

Figure 22. (A) TEM images of undoped $CsPbBr_3$ and (B) 2.1% Bi-doped $CsPbBr_3$ nanocrystals, with HRTEM images shown in the insets, indicating no change in the average size, shape, or crystal structure upon Bi^{3+} doping. (C) Absorption spectra and (D) PL spectra (λ_{ex} = 365 nm) of undoped and Bi-doped (0.25%, 0.8%, and 2.1%) $CsPbBr_3$ nanocrystals showing the spectral shift and change in the band gap energy (Eg, calculated from Tauc plots). Reprinted with permission from Ref. [344], copyright 2017, American Chemistry Society. (E) Photographs of $CsPbBr_3$ (top orange crystals) and $CsPb_{0.9}Bi_{0.1}Br_3$ (bottom black crystals) single crystals with reference grid width of 1 mm. (F) Absorption spectra of the $CsPbBr_3$ and $CsPb_xBi_{1-x}Br_3$ single crystals. Reprinted with permission from Ref. [345], copyright 2017, Royal Society of Chemistry. The red arrows indicating the directions of increasing Bi-doping content: (C) blue-shifted optical responses were observed in the Bi-doped $CsPbBr_3$ nanocrystals, while (F) red-shifted optical responses were observed in the Bi-doped $CsPbBr_3$ single crystals.

Lower toxicity bismuth (Bi^{3+}), antimony (Sb^{3+}), and indium (In^{3+}) ions are commonly used heterovalent ions for lead (Pb^{2+}) ion substitution in perovksite systems. To meet charge neutrality, the final product of lead-free substitution with trivalent ions will no longer be ABX_3 but will be either $A_3B_2X_9$ (e.g., $(MA)_3Bi_2Br_9$ [355] and $Cs_3Sb_2Br_9$ [356])

or $A_2B'B''X_6$ (e.g., Cs_2AgBiX_6 [79, 357, 358] and Cs_2AgInX_6 [282, 359-361]) double perovskite. The structure of $A_3B_2X_9$ can be visualized by removing every third layer of B atoms along the <111> direction of ABX_3 perovskite structure, [356] and the structure of $A_2B'B''X_6$ can be thought of as doubling the ABX_3 perovskite unit cell and replacing the B atoms alternatively with M^+ and M^{3+} cations. [357] CH_3NH_3Br and $BiBr_3$ were used to prepare the $(MA)_3Bi_2Br_9$ nanocrystals through a LARP method at room temperature and obtained blue emitting nanocrystals with emission peak at 423 nm, FWHM of 62 nm, and PLQY of up to 12%. [355] Similarly CsBr and $SbBr_3$ were used to prepare the $Cs_3Sb_2Br_9$ nanocrystals through LARP method and obtained blue emitting nanocrystals with emission peak at 410 nm, FWHM of 41 nm, and PLQY of up to 46%. [356] The emission wavelength of both $(MA)_3Bi_2Br_9$ and $Cs_3Sb_2Br_9$ nanocrystals can be tuned between ~360 nm to ~550 nm via halide substitutions. It was proposed that a Br-rich ($SbBr_x$) surface passivation resulted in the relatively high PLQY of their $Cs_3Sb_2Br_9$ nanocrystals, similar to Br-rich ($PbBr_x$) surface passivation proposed in the $CsPbX_3$ systems. [362] $Cs_3Bi_2Br_9$ nanocrystals have been synthesized through a similar room temperature LARP method, and it was proposed that after addition of deionized (DI) water, a self-passivating layer of BiOBr was formed which led to enhanced PL and improved stability. Similar improvement was not observed in the $(MA)_3Bi_2Br_9$ systems. [71] The optical properties of $Cs_3Bi_2X_9$ nanocrystals [71, 363] displayed a rough trend of slightly red-shifting, with slightly higher quantum yield when compared to $(MA)_3Bi_2X_9$ nanocrystals, [355, 364] though some exceptions exist. $Cs_3Sb_2X_9$ nanocrystals [356] present a wider emission range than both $Cs_3Bi_2X_9$ and $(MA)_3Bi_2X_9$ nanocrystals, and possess a much higher quantum yield for the iodide nanocrystals (Figure 23 and Table 4). Ligand-free $Cs_3Bi_2X_9$ nanocrystals with emission ranging from 400 nm to 560 nm have been synthesized through a one-pot room temperature method similar to the ligand-capped nanocrystals using various CsX and BiX_3 halide salts as precursors (Figure 24). [365] The ligand-free nanocrystals exhibited much lower PLQYs than ligand-capped nanocrystals but the PLQY of ligand-free $Cs_3Bi_2Br_9$ nanocrystals can be improved by storing in open air, which probably facilitates perovskite hydrate formation on the nanocrystal surface passivating surface trap-states. [365] $Cs_3Bi_2I_9$ nanocrystals have been synthesized using a hot-injection method with BiI_3 as a precursor, and the coexistence of direct-indirect transitions of their band gap was discussed. [366] $Cs_3Bi_2I_9$ and $Rb_3Bi_2I_9$ are considered as 0D and 2D structure, respectively. [367]

In the $A_2B'B''X_6$ double perovskite cases, the ionic radii of Bi^{3+} (1.03 Å) and Ag^+ (1.15 Å) are similar to that of Pb^{2+} (1.19 Å) and are commonly used for heterovalent substitutions. [368] Double perovskites made from Bi^{3+} could possess defect-tolerance similar to the perovskites made from Pb^{2+} because of the isoelectronic nature of Bi^{3+} and Pb^{2+}. [369] Some other possible candidates for M^{3+} are Sb^{3+} (0.76 Å), In^{3+} (0.80 Å), and Ga^{3+} (0.62 Å) (As^{3+} is less desirable due to its toxicity). Possible candidates for M^+ are Cu^+ (0.77 Å), Na^+ (1.02 Å), and Au^+ (1.37 Å). [368, 369] Based on calculations, the band gaps for Bi^{3+} and Sb^{3+} double perovskites tend to be indirect and smaller than 2.7 eV, [368] while Cs_2InAgX_6 tend to be direct band gap, which is more suitable for photovoltaic applications. [359] Mn-doped $Cs_2AgInCl_6$ double perovskite nanocrystals have been achieved through a hot injection method. These doped nanocrystals exhibited a bright orange PL emission with PLQY of ~16%, which contrasts greatly with the white PL emission and PLQY of ~1.6% displayed by undoped $Cs_2AgInCl_6$ nanocrystals (Figure 25a). [282] Direct band gap undoped and Ag-doped $Cs_2NaInCl_6$ double perovskite nanocrystals have been synthesized via hot injection method. [370] Varying the amount of Na alloying in $Cs_2Na_xAg_{1-x}BiCl_6$ ($x = 0, 0.25, 0.5, 0.75$, and 1) double perovskites leads to increase in their optical band gaps (from 3.39 eV for $x = 0$ to 3.82 eV for $x = 1$) and significant improvement in their weak PLs (a 30-fold increment). [371] Study reveals that the Bi^{3+} dopants inside the Bi-doped $Cs_2Ag_{1-x}Na_xInCl_6$ double perovskite nanocrystals introduce $BiCl_6$ states that localize just below the CBM are essential for observing any PL emission, while the Ag^+ ions in the double perovskite structure give rise to localized $AgCl_6$ energy levels just above the VBM under Na-rich conditions. [372] The color temperatures of white emitting colloidal $Cs_2Ag_{1-x}Na_xIn_{1-y}Bi_yCl_6$ nanocrystals can be tuned by the amount of Na^+ and Bi^{3+} incorporation ($x = 0$–1, $y = 0.03$–0.16). [373] Doping with lanthanide ions (Yb^{3+} and Er^{3+}) can further red shift the visible emission of $Cs_2AgInCl_6$ nanocrystals to NIR emission with characteristic f−f transition peaks at 996 nm for Yb^{3+} and 1537 nm for Er^{3+} dopants (Figure 25b). [360] Cs_2InBiX_6 and Cs_2InSbX_6 In(I)-based double perovskites have been proposed to be intrinsically unstable, because In(I) easily oxidizes to In(III). [374] Cs_2AgBiX_6 (X = Cl, Br) nanocrystals have been successfully synthesized through hot-injection approaches using acetates (Cs(OAc), Ag(OAc), Bi(OAc)$_3$) as cation precursors and trimethylsilyl halide (TMSCl or TMSBr), [357] hydrochloric acid (HCl), or bromotrimethylsilane as halide precursors. [358] $Cs_2AgBiBr_6$ colloidal nanocrystals have also been successfully synthesized through hot-injection approaches using Cs_2CO_3, $BiBr_3$, and $AgNO_3$, [79] or AgBr [358] as precursors. Formation of quaternary Cs_2AgBiX_6 colloidal nanocrystals requires careful balancing of the reactivities and chemical potentials of the individual components. If balance is not achieved, impurities such as AgX, CsX, Cs−Bi−X or Cs−Ag−X ternary phases (e.g., Cs_3BiX_6) may form. [357] It was found that addition of a small amount of hydrobromic acid (HBr) is critical to ensure the full ionization of Ag^+, which prevents the formation of AgBr impurity in the final product. The injection temperature and the existence of oleylamine are also key factors for successful synthesis because $BiBr_3$ would remain insoluble at temperatures below 160 °C or without the addition of oleylamine. [79] Ligand-free $Cs_2AgBiBr_6$ nanocrystals have, however, been successfully synthesized using CsBr, AgBr and $BiBr_3$ as precursors through a room temperature anti-solvent recrystallization method without heat treatment or oleylamine. [375] These ligand-free $Cs_2AgBiBr_6$ nanocrystals exhibit a sub-band gap long absorption tail originating from surface defects on nanocrystals and could be suppressed by the addition of oleic acid surfactants. [375] The degradation products of $Cs_2AgBiBr_6$ have been proposed to be a combination of two different ternary cesium bismuth bromides (i.e., $Cs_3Bi_2Br_9$ and Cs_3BiBr_6), elemental silver, and bromine. [358]

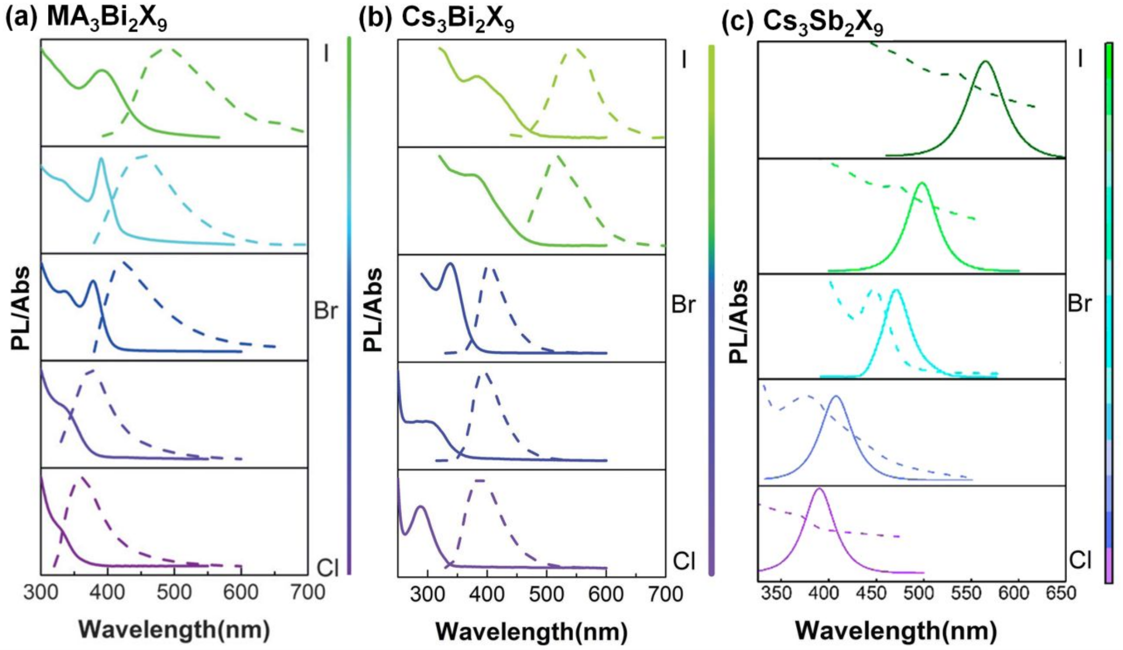

Figure 23. Absorption and PL spectra of (a) $(MA)_3Bi_2X_9$, Reprinted with permission from Ref. [355], copyright 2016, Wiley-VCH. (b) $Cs_3Bi_2X_9$, Reprinted with permission from Ref. [71], copyright 2017, Wiley-VCH. and (c) $Cs_3Sb_2X_9$ Reprinted with permission from Ref. [356], copyright 2017, American Chemistry Society. nanocrystals with different halide compositions. The summary of their optical properties can be found in Table 4.

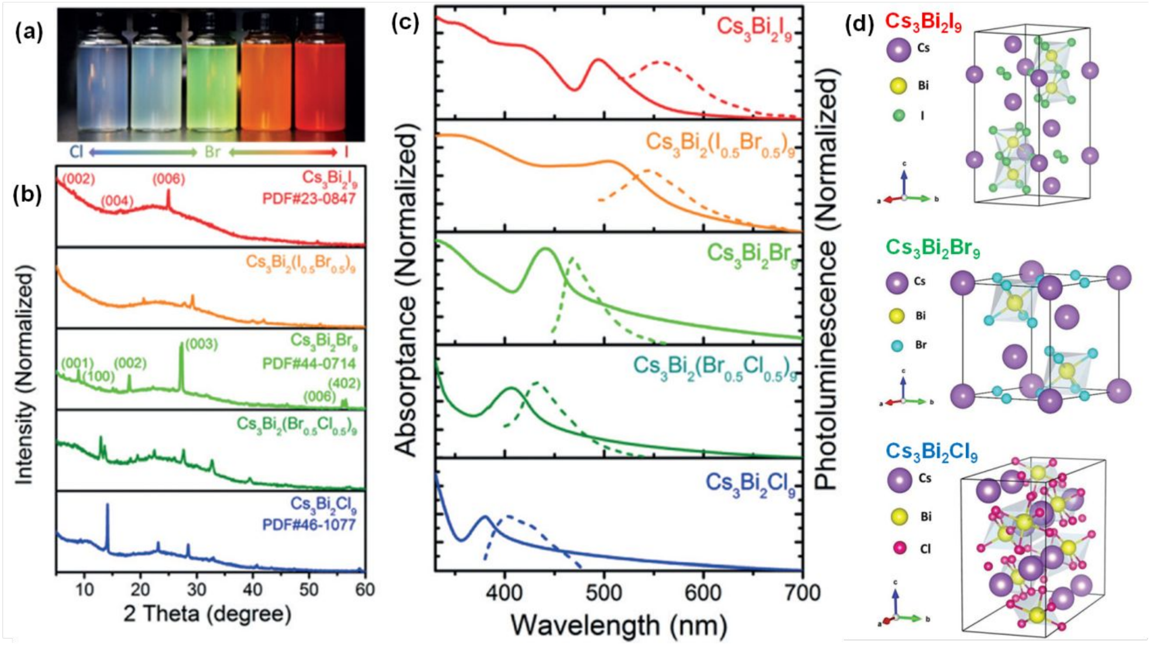

Figure 24. (a) Photographs, (b) XRD patterns, and (c) steady-state absorption and normalized photoluminescence spectra of the ligand-free $Cs_3Bi_2X_9$ (X=Cl, $Cl_{0.5}Br_{0.5}$, Br, $Br_{0.5}I_{0.5}$, I) nanocrystals. Reprinted with permission from Ref. [365], copyright 2017, Wiley-VCH. (d) Unit cell crystal structures of $Cs_3Bi_2I_9$, $Cs_3Bi_2Br_9$, and $Cs_3Bi_2Cl_9$. Reprinted with permission from Ref. [71], copyright 2017, Wiley-VCH.

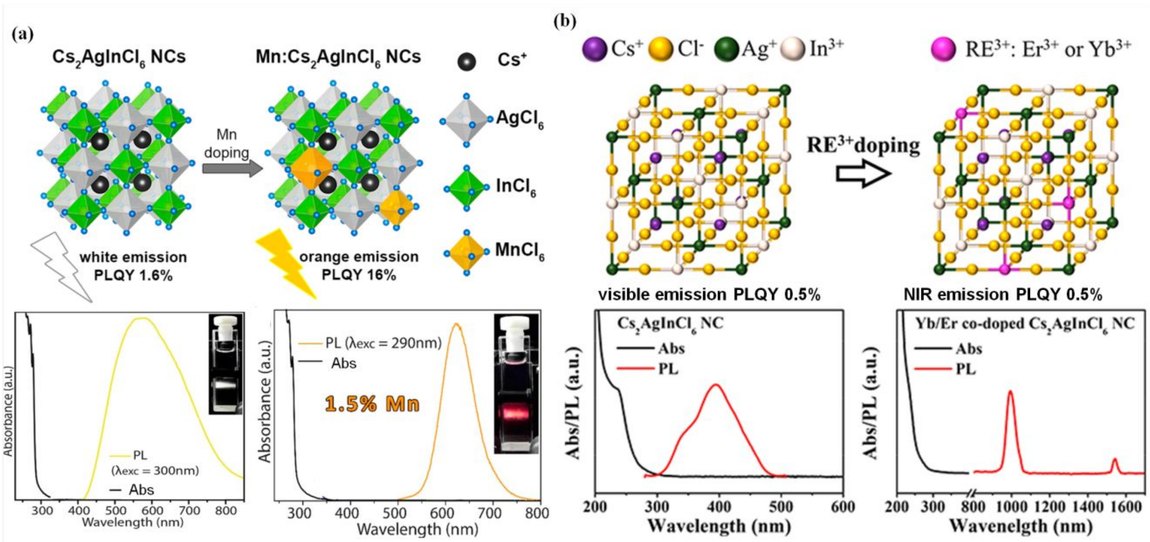

Figure 25. (a) Schematic of double perovskite structures (top panel) as well as absorption and PL spectra (bottom panel) of $Cs_2AgInCl_6$ (left) and Mn-doped $Cs_2AgInCl_6$ (right) nanocrystals. Insets show corresponding optical photos of PL emission of $Cs_2AgInCl_6$ (left) and 1.5% Mn-doped $Cs_2AgInCl_6$ (right) nanocrystals dispersions in hexane from cuvettes under Xe lamp excitation at 300 nm. Reprinted with permission from Ref. [282], copyright 2018, American Chemistry Society. (b) Schematic of double perovskite structures (top panel) as well as absorption and PL spectra (bottom panel) of $Cs_2AgInCl_6$ (left) and Yb^{3+}/Er^{3+}-codoped $Cs_2AgInCl_6$ (right) nanocrystals. RE^{3+} represents rare earth ions. Reprinted with permission from Ref. [360], copyright 2019, American Chemistry Society.

3-7. Size-Dependant Doping Regime

Though highly challenging, pinpointing the exact location or distribution of dopants within a host matrix and understanding the underlying mechanisms of doping is of key importance. Whether foreign ions can be fully incorporated within or simply segregate on the surface of the perovskite crystals depends heavily on the dopant's ionic radii. Take the incorporation of divalent alkaline earth metal ions in MA-based perovskite as an example. Theoretical calculations have predicted that Sr^{2+} can replace Pb^{2+} in the perovskite lattice because Sr^{2+} and Pb^{2+} have similar ionic radii (118 pm and 119 pm, respectively) and the tolerance factor of $MASrI_3$ (0.91) falls within the stable 3D perovskite structure range (0.8 to 1.0). [376] Despite that, the synthesis of a pure 3D $MASrI_3$ halide perovskite has not yet been reported. In Sr-doped perovskite films, a Sr-rich secondary phase has been observed to form on the surface. [377] On the other hand, Mg^{2+}, with a smaller ionic radius (72 pm), cannot form stable $MAMgI_3$ as its tolerance factor (1.06) is not within the stable 3D perovskite structure range (0.8 to 1.0).[377] Figure 26a and 26b show the grazing incidence x-ray diffraction (GIXRD) patterns of Sr and Mg-doped tetragonal $MAPbI_3$. No additional peaks were seen upon the addition of Sr^{2+} and Mg^{2+}, indicating no new crystalline phases are formed. The lack of an identifiable secondary phase suggested that the surface segregated phase is either amorphous or too thin (or too dispersed) to be detected by GIXRD. Le Bail refinement and the effect of GIXRD patterns broadening were used to characterise the microstrain due to doping. As schematically shown in Figure 26c, the microstrain represents a local distortion of the lattice, which can be revealed as a broadening of the peaks. No systematic XRD peak shift was observed, signifying the absence of lattice macrostrain or homogenous changes in the crystal structure. The microstrain evolution of the Sr doping (Figure 26d) and Mg doping (Figure 26e) series showed that the perovskite lattice can accumulate distortion up to a critical doping level, after which the lattice relaxes back probably due to the formation of segregated secondary phase. The microstrain of Sr-doped samples reached a maximum value at a doping concentration of 0.2% and quickly droped to a value similar to the undoped sample at higher concentrations. This suggested that phase segregation dominated the doping process, with dopant lattice incorpation only occurring within the low doping regime of 0.2. On the other hand, the microstrain in Mg-doped samples showed a more gradual decrease after the maximum was reached at doping concentration of 1%, implying both lattice incorporation and lattice relaxation due to segregation can occur simultaneously at concentrations higher than 1%. It is hypothesized that dopants are incorporated into the perovskite lattice until a critical distortion is attained, beyond which the dopant starts to segregate at the surface, resulting in a relaxation of the perovskite lattice. The findings that Mg^{2+} has a higher inclusion concentration than Sr^{2+} (despite the more favorable tolerance factor of Sr^{2+}) suggests a plausible scenario of Mg^{2+} inclusion in interstitial positions.[377] The Mg-doped perovskite lattice only shows contraction in the c-direction while the Sr-doped perovskite lattice displays uniform changes in both directions. It can be concluded true incorporation of the dopant into the perovskite lattice occurs within the low doping concentration regime (0.1-1 mol%). In contrast, the high doping concentration regime (3-10 mol%, such as those numbers commonly used in the literature) results in surface phase segregation. Moreover, it was also found that, for one dopant (Sr^{2+} or Mg^{2+}), the low doping regime induces a more n-type doping character, yet the high doping regime triggers a less n-type doping feature, which is different from classical doping in silicon system. [377]

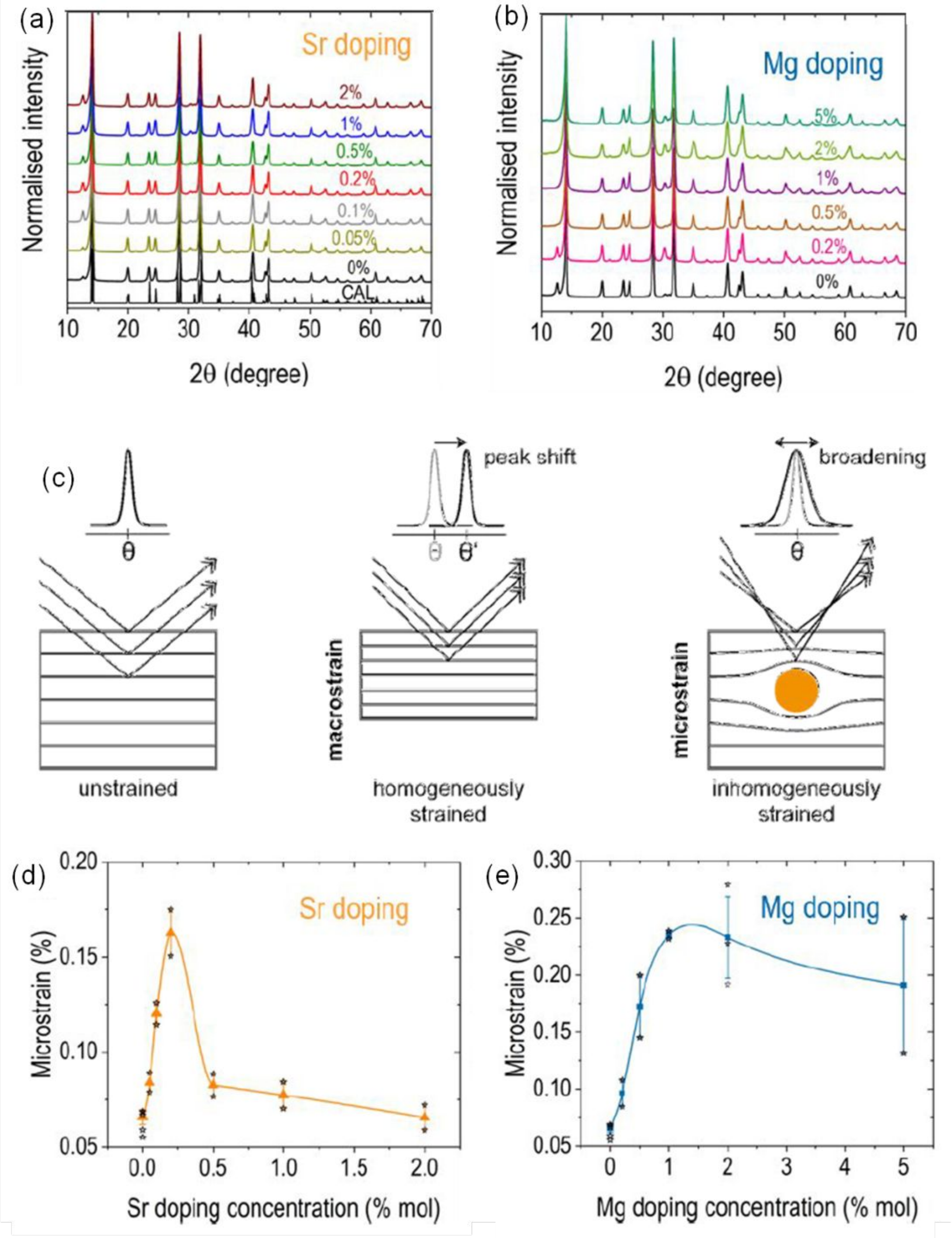

Figure 26. Grazing incidence x-ray diffraction (XRD) patterns of (a) Sr doping series (CAL is the theoretical calculation of tetragonal $MAPbI_3$) and (b) Mg doping series in $MAPbI_3$. (c) Schematic of no strain (left panel), macrostrain (central panel) which causes a peak shift in XRD pattern, and microstrain (right panel) which induces a peak broadening. (d) Microstrain values obtained by Le Bail refinement of the Sr-doped $MAPbI_3$ and (e) the Mg-doped $MAPbI_3$ samples as a function of nominal dopant concentration. The depicted microstrain values are the mean of at least two different samples (star points next to the

mean values), and the error bar represents the standard deviation. Spline fits of the values are shown as a visual guide. Reprinted with permission from Ref. [377], copyright 2020, American Chemistry Society.

Table 4. Summary of the emission peak wavelength, full width at half maximum (FWHM), photoluminescence quantum yield (PLQY), and synthesis method of colloidal metal halide perovskite nanocrystals with different B-site substitutions.

Nanocrystals	Emission Peak (nm)	FWHM (nm)	PLQY (%)	Ligands	Synthesis Method	Ref.
$CsPb_{0.9}Sn_{0.1}Br_3$	519	19	91.9	Oleylamine, oleic acid	LARP	[226]
$CsPb_{0.7}Sn_{0.3}Br_3$	516	28	62	Oleylamine, oleic acid	LARP	[226]
$CsPb_{0.5}Sn_{0.5}Br_3$	503	27	41	Oleylamine, oleic acid	LARP	[226]
$CsPb_{0.3}Sn_{0.7}Br_3$	501	30	30	Oleylamine, oleic acid	LARP	[226]
$CsPb_{0.1}Sn_{0.9}Br_3$	521	--	9.2	Oleylamine, oleic acid	LARP	[226]
$Na^+:CsPb_{1-x}Sn_xI_3$	840	~150	~28	Tri-n-octylphosphine, oleylamine, oleic acid	Hot injection method	[241]

$CsPb_{0.97}Mn_{0.03}Cl_3$	396/569	--	5	Oleylamine, oleic acid	Hot injection method	[257]
$CsPb_{0.94}Mn_{0.06}Cl_3$	396/574	--	22	Oleylamine, oleic acid	Hot injection method	[257]
$CsPb_{0.87}Mn_{0.13}Cl_3$	396/575	--	43	Oleylamine, oleic acid	Hot injection method	[257]
$CsPb_{0.73}Mn_{0.27}Cl_3$	396/579	--	54	Oleylamine, oleic acid	Hot injection method	[257]
$CsPb_{0.62}Mn_{0.38}Cl_3$	396/582	--	36	Oleylamine, oleic acid	Hot injection method	[257]
$CsPb_{0.54}Mn_{0.46}Cl_3$	396/587	--	17	Oleylamine, oleic acid	Hot injection method	[257]
Mn^{2+}:$CsPbCl_3$	404/600	25/90	12.7	Oleylamine, oleic acid	Hot injection method	[378]
Mn^{2+}:$CsPbBr_3$	~520	~25	89.6	Oleylamine, oleic acid	Hot injection method	[378]
Mn^{2+}:$CsPbI_3$	~690	~50	57.1	Oleylamine, oleic acid	Hot injection method	[378]
Ca^{2+}:$CsPbCl_3$	406.1	~10	77.1	Tri-n-octylphosphine, oleylamine, oleic acid	Hot injection method	[328]
$CsPb_{0.7}$ $Ce_{0.3}Br_3$	516	~25	52	Oleylamine, oleic acid	Hot injection method	[302]
$CsPb_{0.66}Ce_{0.34}Br_3$	~514	~25	64	Oleylamine, oleic acid	Hot injection method	[302]
$CsPb_{0.65}Ce_{0.35}Br_3$	~512	~25	50	Oleylamine, oleic acid	Hot injection method	[302]

$CsPb_{0.55}Ce_{0.45}Br_3$	~512	~25	78	Oleylamine, oleic acid	Hot injection method	[302]
$CsPb_{0.26}Ce_{0.74}Br_3$	510	~25	89	Oleylamine, oleic acid	Hot injection method	[302]
Yb^{3+}:$CsPbCl_3$	990	~55	170	Oleylamine, oleic acid	Hot injection method	[306]
Ni^{2+}:$CsPbCl_3$	407	<15	96.5	Tri-n-octylphosphine, oleylamine, oleic acid	Hot injection method	[333]
Ni^{2+}:$CsPbCl_{0.99}Br_{2.01}$	470	~20	89	Oleylamine, oleic acid	LARP	[334]
Ni^{2+}:$CsPbI_3$	~660	~40	79.2	Oleylamine, oleic acid	Hot injection method	[208]
Cd^{2+}:$CsPbCl_3$	406	~10−12	96±2	Tri-n-octylphosphine, oleylamine, oleic acid	Hot injection method w/ postsynthetic treatment	[336]
Cu^{2+}:$CsPb(Br/Cl)_3$	459	<40	92.6	Tri-n-octylphosphine, oleylamine, oleic acid	Hot injection method w/ postsynthetic treatment	[338]
$CsPb_{0.93}Cu_{0.07}(Br/Cl)_3$	453	<30	80	Oleylamine, oleic acid	Hot injection method	[337]
Al^{3+}:$CsPbBr_3$	456	16	42	Oleylamine, oleic acid	Hot injection method	[351]

Bi^{3+}:CsPbBr$_3$	517	~20	55	Oleylamine, oleic acid	Hot injection method	[344]
$MA_3Bi_2Cl_9$	360	50	15	Oleylamine, oleic acid	LARP	[355]
$MA_3Bi_2Br_9$	423	62	12	Oleylamine, oleic acid	LARP	[355]
$MA_3Bi_2I_9$	540	91	0.03	Oleylamine, oleic acid	LARP	[355]
$MA_3Bi_2Cl_9$	370	~50-60	24.7	Octylamine, oleic acid	LARP	[364]
$MA_3Bi_2Br_3Cl_6$	399	~50-60	22.4	Octylamine, oleic acid	LARP	[364]
$MA_3Bi_2Br_6Cl_3$	422	~50-60	54.1	Octylamine, oleic acid	LARP	[364]
$MA_3Bi_2Br_9$	422	~50-60	13.5	Octylamine, oleic acid	LARP	[364]
$Cs_3Bi_2Cl_9$	393	59	26.4	Oleylamine, oleic acid	Recrystallization method	[71]
$Cs_3Bi_2Br_9$	410	48	19.4	Oleylamine, oleic acid	Recrystallization method	[71]
$Cs_3Bi_2I_9$	545	70	0.018	Oleylamine, oleic acid	Recrystallization method	[71]
$Cs_3Bi_2Cl_9$	380	57	62	Octylamine, oleic acid	LARP	[363]
$Cs_3Bi_2Br_9$	411	38	22	Octylamine, oleic acid	LARP	[363]
$Cs_3Bi_2I_9$	526	76	2.3	Octylamine, oleic acid	LARP	[363]
$Cs_3Sb_2Cl_9$	370	52	11	Oleylamine or	LARP	[356]

				octylamine, oleic acid		
$Cs_3Sb_2Br_9$	410	41	46	Oleylamine or octylamine, oleic acid	LARP	[356]
$Cs_3Sb_2I_9$	560	56	23	Oleylamine or octylamine, oleic acid	LARP	[356]
$CsPb_{0.67}Sn_{0.33}Br_3$	517	~25	83	Oleylamine, oleic acid	Hot injection method	[230]
$CsSnCl_3$	~490	~100	≤0.14	Tri-n-octylphosphine, oleylamine, oleic acid	Hot injection method	[234]
$CsSnBr_3$	~660	~50	≤0.14	Tri-n-octylphosphine, oleylamine, oleic acid	Hot injection method	[234]
$CsSnl_3$	~945	~75	≤0.14	Tri-n-octylphosphine, oleylamine, oleic acid	Hot injection method	[234]
Cs_2SnI_6	~620	--	≤0.48	Oleylamine, oleic acid	Hot injection method	[237]
$Cs_2AgBiCl_6$	395	68	6.7	Oleic acid	Recrystallization method	[375]

$Cs_2AgBiBr_6$	465	82	0.7	Oleic acid	Recrystallization method	[375]
Cs_2AgBiI_6	575	69	<0.1	Oleic acid	Recrystallization method	[375]

4. X-Site Substitution

Tuning the emission bandgap of lead halide perovskite nanocrystals differs from traditional II−VI, III−V, and IV−VI semiconductor quantum dots because instead of altering dimensionality to utilize quantum confinement effects, [6, 7, 113, 126, 136, 187, 190, 191, 379-385] the emission band gap of metal halide perovskite nanocrystals is primarily tuned by their halide compositions. [5, 386, 387] For lead halide perovskite, the maximum wavelength difference that can be tuned by quantum confinement effects is roughly 100 nm (Figure 27a), which is relatively narrow compared to greater than 300 nm range that can be tuned via varying halide compositions (Figure 27b). [191]

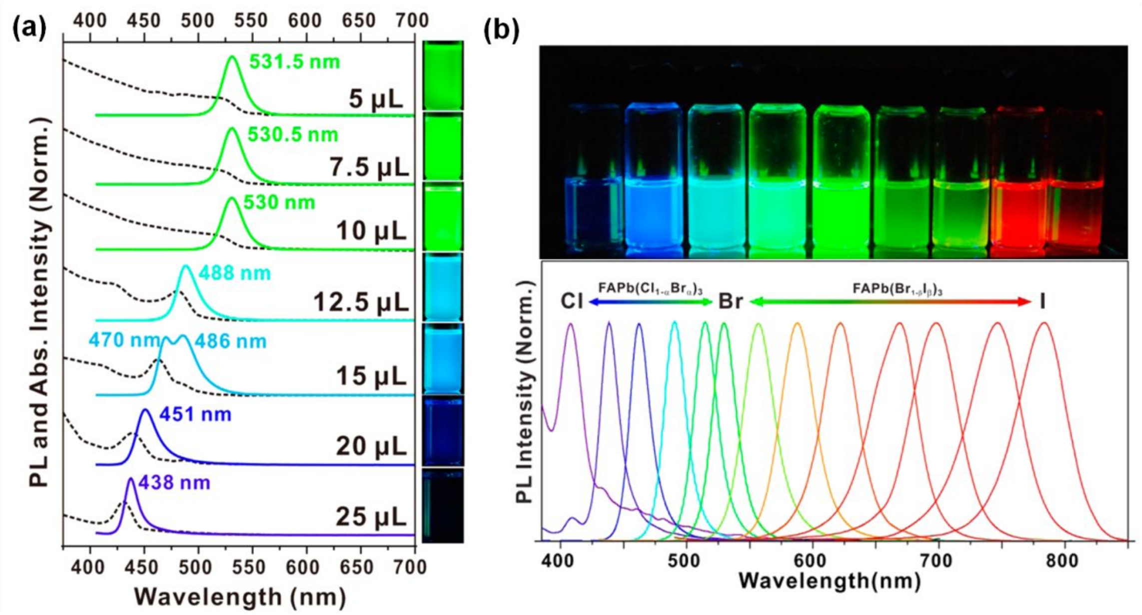

Figure 27. (a) Absorption (dashed lines) and PL (solid lines) spectra of $FAPbBr_3$ nanocrystals synthesized by varying the amount of oleylamine capping molecule from 5 to

25 μL (70%, Sigma-Aldrich), demonstrating their tunability through quantum confinement effect. (b) PL emission spectra of $FAPbBr_3$ nanocrystals synthesized with different halide anions, demonstrating their tunability through varying their anion species. Photographs in (a) and (b) are their corresponding suspension samples under 365 nm UV irradiation. Reprinted with permission from Ref. [191], copyright 2017, American Chemistry Society.

4-1. Halide-based Perovskite Nanocrystals

Compared to cation-exchange, anion-exchange in perovskite systems is relatively fast and easy. Mixed-halide perovskite (e.g., $CsPb(Br/Cl)_3$ or $CsPb(Br/I)_3$) colloidal nanocrystals can be achieved by either direct synthesis strategy of directly using mixed-anion precursors during nanocrystals synthesis, or by postsynthetic strategy of adding excess amounts of Cl or I halide precursors into as prepared colloidal bromide-based perovskite (e.g., $MAPbBr_3$ or $CsPbBr_3$) nanocrystal suspensions. [386] Options for Cl or I halide precursors include: lead halides (PbX_2), [386, 388] organoammonium halides (such as octadecylammonium halides (ODA-X), [386] oleylammonium halides (OLAM-X)), [386, 387, 389] and aryl-based aniline hydrohalide (An-HX). [389] Fast anion-exchange kinetics in halide perovskites are likely due to their low defect formation energy, the rigid nature of their cationic sublattice, and the high ion mobility in the lattice due to the prevalence of vacancies. [390, 391] Although both chlorine exchange and iodine exchange of $CsPbBr_3$ nanocrystals are kinetic processes and demonstrate no thermodynamic preference for these two anions, their anion exchange mechanisms are actually different: the chlorine exchange is likely diffusion-limited, whereas the iodine exchange is likely surface-limited. [392] In most cases, the parent $CsPbBr_3$ nanocrystals retain their cubic (Figure 28a) [387] or orthorhombic (Figure 28b) [390] structures during their anion-conversion from $CsPbBr_3$ to $CsPbI_3$ or $CsPbCl_3$. [95] There are also cases where $CsPbBr_3$ nanocrystals are transformed from cubic to orthorhombic when increasing the I^- anion-exchange level (Figure 28c), [388] which indicates that $CsPbBr_{3-x}I_x$ nanocrystals do not form a continuous solid solution over the entire I^- anion-exchange range (from $0 \leq x \leq 3$). [95] These contradictory findings may be due to anion-exchanged $CsPbI_3$ nanocrystals gradually undergoing a phase transition from black cubic phase to their thermodynamically preferred yellow orthorhombic phase. [393] Conversely, the shape and crystal structure of the parent $CsPbBr_3$ nanocrystals is retained while undergoing the Br−Cl exchange process. [388] There are still limitations for band gap tuning via halide substitutions. In perovskites, the conduction band (E_c) (electron affinity) and valence band (E_v) (ionization potential) energies are dictated mostly by the atomic orbitals of the cations and anions, respectively. [394] The valence orbitals change from 3p to 4p to 5p with a monotonic decrease in electron binding energy (lower ionization potential) during the halide substitution from Cl to Br to I, with most offset shown in the valence band (ΔE_v). [158] For example, the band gaps for $MAPbX_3$ can only be changed from 3.11, 2.22, to 1.51 eV for X=Cl, Br, and I, respectively, [395] which indicates that in order to obtain perovskites with band gaps smaller than 1.51 eV, an offset in the conduction band is also required, which would require substitution of a B-site cation.

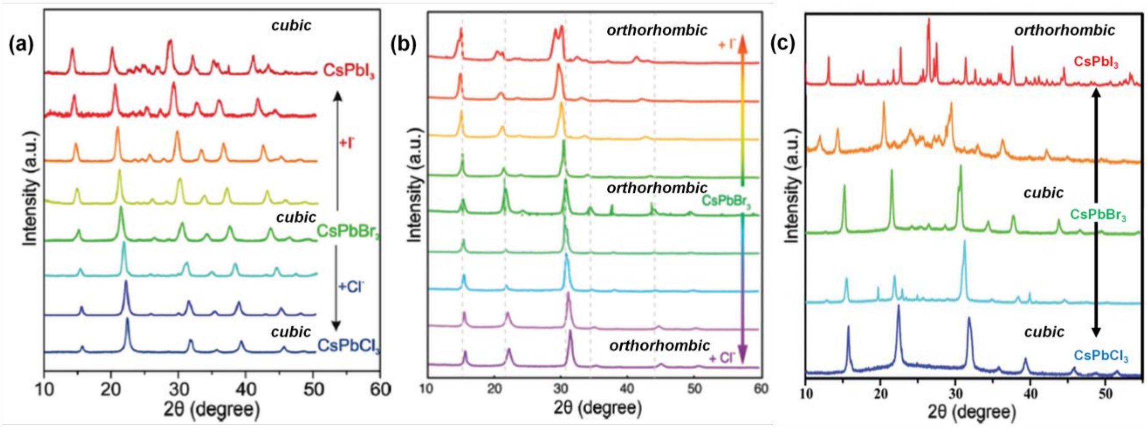

Figure 28. XRD patterns of the parent $CsPbBr_3$ nanocrystals with (a) cubic structure (Reprinted with permission from Ref. [387], copyright 2015, American Chemistry Society.) and (b) orthorhombic structure (Reprinted with permission from Ref. [390], copyright 2016, American Chemistry Society.) that retain their structures after anion-exchange processes; while in some cases (c) the structure of $CsPbBr_3$ nanocrystals gradually changes from cubic to orthorhombic when increasing the I content during their anion-exchange processes. Reprinted with permission from Ref. [388], copyright 2016, Royal Society of Chemistry.

Colloidal metal halide perovskite nanocrystals display fast exchange dynamics in solution, even in the absence of an excess halide source. Simply mixing two different colloidal halide perovskite nanocrystal suspensions in one vial would result in anion-exchange between these two nanocrystals. [386, 387] Solution-phase is not a prerequisite for anion exchange, as solid-state anion exchange was also observed when mixing two different halide perovskite dried powders or mixing perovskite powders with other halide containing solids (e.g., KCl, KBr, KI). [396] Only Cl−Br and Br−I couples (and never for Cl−I couples) are attainable in halide exchange. Attempts to yield $CsPbCl_3$ directly from $CsPbI_3$ nanocrystals (or vice versa) through anion-exchange or mixing $CsPbCl_3$ and $CsPbI_3$ nanocrystals together to obtain intermediate $CsPb(Cl/I)_3$ nanocrystals have yet to be succeeded. Generally, the PL is completely diminished, suggesting a total dissolution of particles. One possible explanation is that due to the large difference in ionic radii between Cl^- and I^-, the direct exchange between Cl^- and I^- would involve a structural stress on the lattice that cannot be tolerated, resulting in destruction of perovskite nanocrystals. [386] Researchers have demonstrated heterojunction cesium lead halide perovskite nanowires, where different segments of the same nanowire contain of different halide ions. For example, half of the nanowire could be $CsPbBr_3$ while the other half is $CsPbI_3$ or $CsPbCl_3$ (Figure 29A-G). This heterojunction structure perovskite was achieved by a very delicately controlled anion exchange process where a segment of a nanowire was partially coated in poly(methyl methacrylate) (PMMA) while the other segment underwent anion exchange. [391] Besides using delicate PMMA masking to achieve desired anion exchange patterning, anion exchange patterning via photo-excitation has also been demonstrated. Light can trigger photoinduced anion exchange in $CsPbX_3$ nanocrystal-dihalomethane solutions (Figure 30). [397] The accepted mechanism for this novel phenomenon is that photoexcited $CsPbX_3$ nanocrystals transfer an interfacial electron to a dihalomethane (e.g., dichloromethane (DCM) or dibromomethane (DBM)) solvent molecule, and halide anions are produced in-situ by the reductive dissociation due to the transferred electron. The extent of photoinduced anion-exchange reaction can be precisely controlled by either changing the photon dose or wavelength of the excitation light. [397]

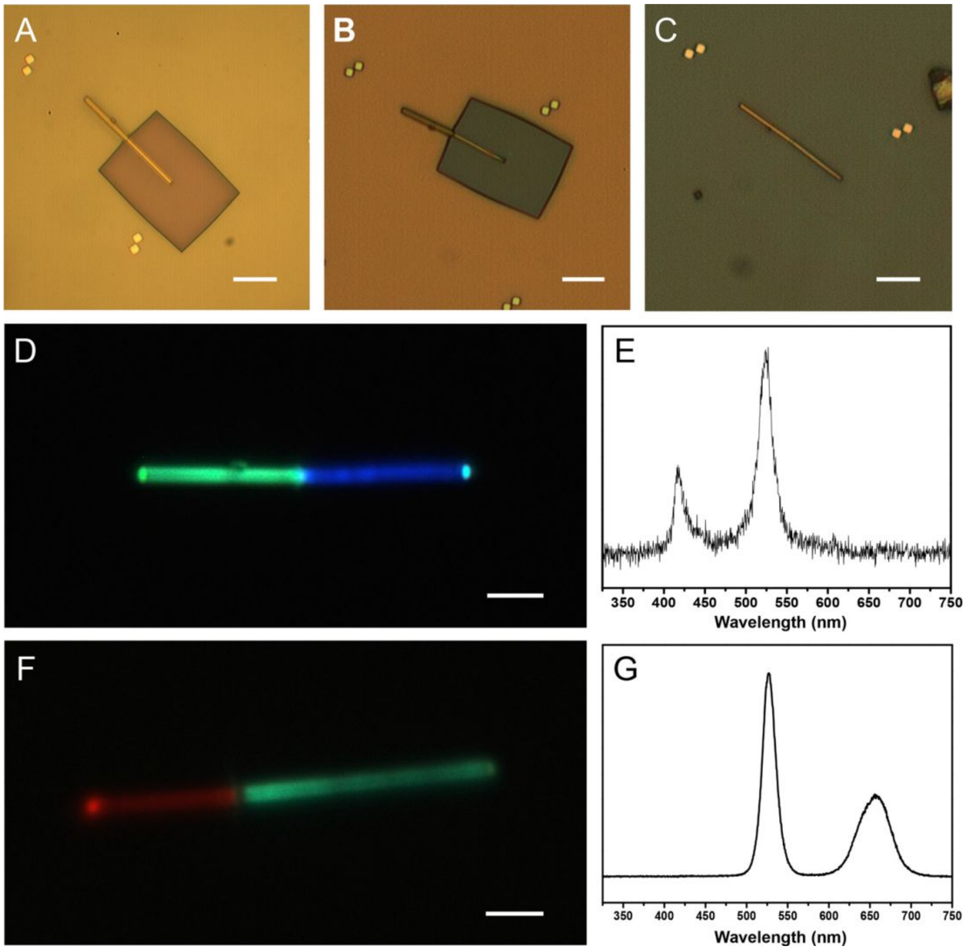

Figure 29. Fabrication and PL characterization of cesium lead halide perovskite nanowire heterojunctions. (A) Optical microscope image of a $CsPbBr_3$ nanowire partially coated with PMMA before anion exchange. (B) Optical image of the $CsPbBr_3$ nanowire partially coated with PMMA after anion exchange. (C) Optical image of the $CsPbBr_3$ nanowire after anion exchange and after removal of PMMA. (D) Optical image of the partial bromide/partial chloride nanowire under laser excitation, and (E) the corresponding PL emission spectrum. (F) Optical image of the partial iodide/partial bromide nanowire under laser excitation, and (G) the corresponding PL emission spectrum. Scale bars for (A)–(C) are 10 μm, while scale bars for (D) and (F) are 3 μm. Reprinted with permission from Ref. [391], copyright 2017, National Academy of Sciences.

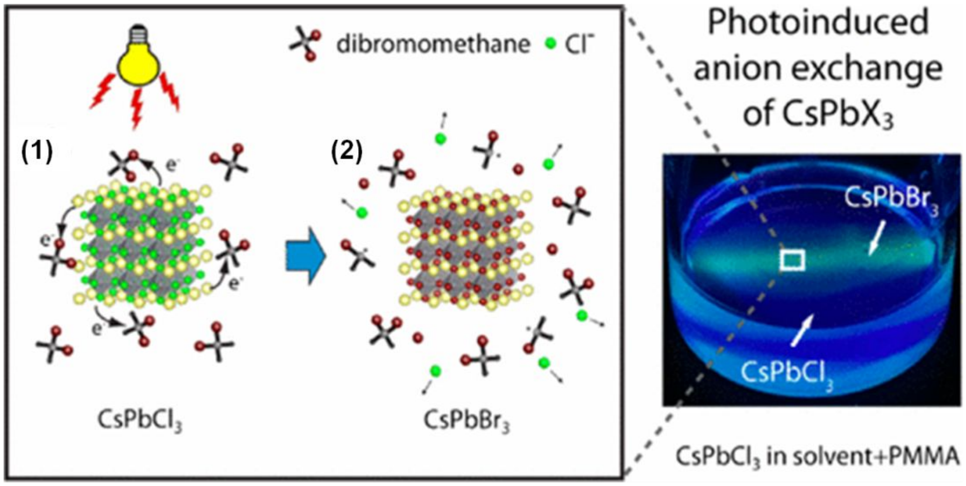

Figure 30. Optical image of the photoinduced anion exchange of $CsPbX_3$ (X=Cl to Br) nanocrystals in dibromomethane solution (right figure), and schematic of the proposed mechanism for photoinduced anion exchange reaction (left figure): (1) photoinduced electron transfer from $CsPbCl_3$ nanocrystals to dibromomethane solvent, (2) halides from reductive dissociation of solvent causing the anion exchange of perovskite nanocrystals to $CsPbBr_3$. Reprinted with permission from Ref. [397], copyright 2017, American Chemistry Society.

4-2. SCN-based Perovskite Nanocrystals

Pseudo-halide thiocyanate ions (SCN^-, which has a similar ionic radius to I^-) were first introduced to partially replace the iodide ions in $MAPbI_3$ thin film solar cells to improve the stability/moisture tolerance of the cells and were found to also increase the crystal size. [398-402] It was found that individual $MAPbI_{3-x}(SCN)_x$ crystals demonstrate spatially heterogeneous PL emission, with substantially higher intensity at the grain boundaries as compared to the interior regions of the crystals. [403] Studies have since revealed that the proposed $MAPbI_{3-x}(SCN)_x$ 3D-connected perovskite structure may actually be $(MA)_2Pb(SCN)_2I_2$ 2D-layered orthorhombic structure instead, where Pb is octahedrally coordinated by four I^- ions and two S-bonded SCN^- ligands, while the MA^+ cations are situated between the layers of $Pb(SCN)_2I_4$ octahedra (similar to a K_2NiF_4-type structure). [404] DFT calculation has shown that $(MA)_2Pb(SCN)_2I_2$ has improved chemical stability against phase separation and does not spontaneously decompose into either MAI + $Pb(SCN)_2$ (with ΔH= 0.38 eV) or MA(SCN) + PbI_2 (with ΔH= 1.97 eV). As a comparison, it is thermodynamically favorable for $MAPbI_3$ to spontaneously decompose into MAI + PbI_2 (with ΔH= -0.09 eV). [405] Another study claimed, because of their observation of red solid phase decomposing into black solid under ambient humidity, that it is possible for $3(MA)_2Pb(SCN)_2I_2$ to decompose into $2MAPbI_3$ + 4MA(SCN) + $Pb(SCN)_2$ by hydration. [406] These 2D-layered $(MA)_2Pb(SCN)_2I_2$ single crystals displays a reversible piezochromism phenomena. When compressed in a diamond-anvil cell, the color of single crystals changes from translucent red (1 GPa) to opaque black (2.6 GPa), then to translucent yellow (3.9 GPa), and finally retains this color up to 4.3 GPa, suggesting a substantial change in the corresponding band gap. [406] A'A"$Pb(SCN)_2I_2$-type 2D perovskite films have been systematically studied by replacing the cation species (A'A") with combinations of MA, FA, and Cs cations. [407] Despite the wide study of thiocyanate-based perovskite films, thiocyanate-based perovskite nanocrystals are rarely studied. SCN-doped $CsPbBr_3$ nanocrystals have been achieved by replacing a small amount of Br^- ions with SCN^- ions forming $CsPbBr_{3-x}(SCN)_x$ nanocrystals. This substitution led to an increase in the crystallinity and a slightly blue-shifted PL peak, without significant change in their shapes or crystal structures. [162]

4-3. Split-anion-based Perovskite Nanocrystals

Some scientists have proposed partially replacing some of the halide anions (Cl, Br, I) in perovskite with chalcogen anions (S, Se, Te), forming a so-called "split-anion" system with mixed chalcogen and halogen anions. This strategy is mostly employed in antimony or bismuth-based perovskites (e.g., $MASbI_2S$, [408] and $MABiI_2S$ [409]). [410, 411] The potential benefit of such Pb-free perovskites with mixed chalcogen and halogen anions, $AB(Ch,X)_3$ (A = Cs or Ba; B = Sb or Bi; Ch = chalcogen (S, Se, Te); X = halogen (Cl, Br, I)), is that the metal–chalcogenide bonds are more covalent than metal-halide bonds and as such may exhibit an enhanced stability under ambient conditions. [411] Solar cells fabricated from Pb-free perovskites with mixed chalcogen and halogen anions exist, [408] but this field is still relatively new for colloidal nanocrystals. This new class of split-anion perovskites may broaden the selection pool of elements for designing perovskite nanocrystals by allowing higher valence cations (such as 3^+ or 4^+ cations instead of 2^+) in the place of B-site cation (e.g., $MABiSI_2$ or $CsSnS_2Cl$) due to the introduction of divalent chalcogen anions. [410, 411]

5. Applications

Owing to their outstanding optoelectronic properties, doped and ion-substituted colloidal metal halide perovskite nanocrystals show promising potential for many practical applications, including light emitting diodes (LEDs), lasing, perovskite solar cells, photodetectors, among many others.

5-1. LEDs based on Doped or Ion-Substituted Perovskite Nanocrystals

Due to the excellent stability and appealing optoelectronic perperties of Cs-based perovskite nanocystals, A site doping using Cs^+ is recognized as an effective strategy for improving the performance of organic-inorganic perovskite-based LEDs. Cs doped perovskite $FA_{(1-x)}Cs_xPbBr_3$ nanocrystals with specific Cs content (x = 0, 0.1, 0.2, and 0.3) have been applied as the emissive material for LED devices. The device structure consists of a transparent conductive indium tin oxide (ITO)-coated glass substrate, a hole-transporting layer of poly(3,4-ethylenedioxythiophene):poly(styrenesulfonate) (PEDOT:PSS) and poly[(9,9-dioctylfluorenyl-2,7-diyl)-co-(4,4'-(N-(4secbutylphenyl)diphenylamine)] (TFB), a photoactive layer of $FA_{(1-x)}Cs_xPbBr_3$ perovskite nanocrystals, an electron-transporting layer of 1,3,5-Tris(1-phenyl-1H-benzimidazol-2-yl)benzene (TPBi), an electron injection layer of LiF and a cathode layer of Al (Figure 31a). [42] The electroluminescence (EL) mechanism of the LED device is described as follows (Figure 31b): electrons are injected from the lowest unoccupied molecular orbital (LUMO) level of TPBi into the conduction band (CB) of perovskite nanocrystals. Holes are transferred from the highest occupied molecular orbital (HOMO) level of TFB into the valance band (VB) of perovskite nanocrystals, followed by radiative recombination of electron-hole pairs inside the active perovskite layer. [42] Alignment of the energy levels of different components in the LED device is a key factor that significantly affects the performance of LEDs. With increasing Cs content (x = 0, 0.1, 0.2, and 0.3), the VB levels of $FA_{(1-x)}Cs_xPbBr_3$ gradually decreased from −5.88 ev to −5.25 eV which facilitating the hole injection due to the reduced hole injection barrier at the interface between the perovskite and the hole transport layer. The electroluminescence (EL) spectra (Figure 31c) of the $FA_{(1-x)}Cs_xPbBr_3$-based perovskite LEDs exhibits gradual blue-shifts as a function of increasing Cs, which is consistent with the PL spectra of the corresponding nanocrystals (Figure 5e). The inset of Figure 31c shows a photograph of the best performacne LED device based on $FA_{0.8}Cs_{0.2}PbBr_3$ with a luminance of 55,005 cd m^{-2} (Figure 31d) and a current efficiency (CE) of 10.09 cd A^{-1} (Figure 31e), exhibiting 6.4-fold and 3.6-fold improvement, respectively, over those of undoped $FAPbBr_3$. [42] Further increasing the Cs doping ratio from x=0.2 to 0.3 did not improve device performance, indicating an optimized doping content of Cs is crucial in achieving good device performance. The excellent performance of $FA_{0.8}Cs_{0.2}PbBr_3$-based LEDs may be attributed to the high crystallinity, large quantum efficiency and efficient hole injection of Cs-doped $FAPbBr_3$. In another case of Cs-doped $FAPbBr_3$ perovskite, colloidal $FA_{0.8}Cs_{0.2}Pb_xBr_3$ nanocrystals with varied Pb content (x = 1.0, 0.8, 0.7, and 0.6) were fabricated forming stoichiometrically “less-lead” perovskite. [43] As the x value decreased from 1.0, 0.8 to 0.7, the maximum luminance, current efficiency (CE), and external quantum efficiency (EQE) are greatly enhanced (the maximum luminance, CE, and EQE for x = 0.7 is 45,440 cd m^{-2}, 28.61 cd A^{-1}, and 6.75%, respectively, while for x =1.0 is 23720 cd m^{-2}, 9.38 cd A^{-1}, and 2.67%, respectively, Figure 31f-31h), probably due to improved hole injection resulting from the reduced hole injection barrier between the perovskite and hole transport layer. Further decreasing the Pb ratio from 0.7 to 0.6 did not further improve the device performance, indicating the best LED performance stems from the optimized Pb ratio in $FA_{0.8}Cs_{0.2}Pb_{0.7}Br_3$. [43] It was suggested that the “less-lead” configuration can inhibit nonradiative recombination by diminishing the presence of uncoordinated metallic Pb atoms. It was also found that the improved stability of $FA_{0.8}Cs_{0.2}Pb_{0.7}Br_3$-based LED device can be attributed to the hydrogen-bonding interactions between the organic cation and halide anions, induced by the moderate ambient moisture. [43] When Cs was doped into

MAPbBr$_3$ nanocrystals, the performance of MA$_{1-x}$Cs$_x$PbBr$_3$-based LEDs were also highly correlated with the Cs content. Notably, MA$_{0.7}$Cs$_{0.3}$PbBr$_3$-based LEDs displayed a maximum luminescence of 24500 cd m^{-2}, nearly 10-fold higher than that of previously reported MAPbBr$_3$ nanocrystals. [206] Interestingly, through doping FA into CsPbI$_3$ nanocrystals, it is feasible to achieve stable red-emitting LED. [202]

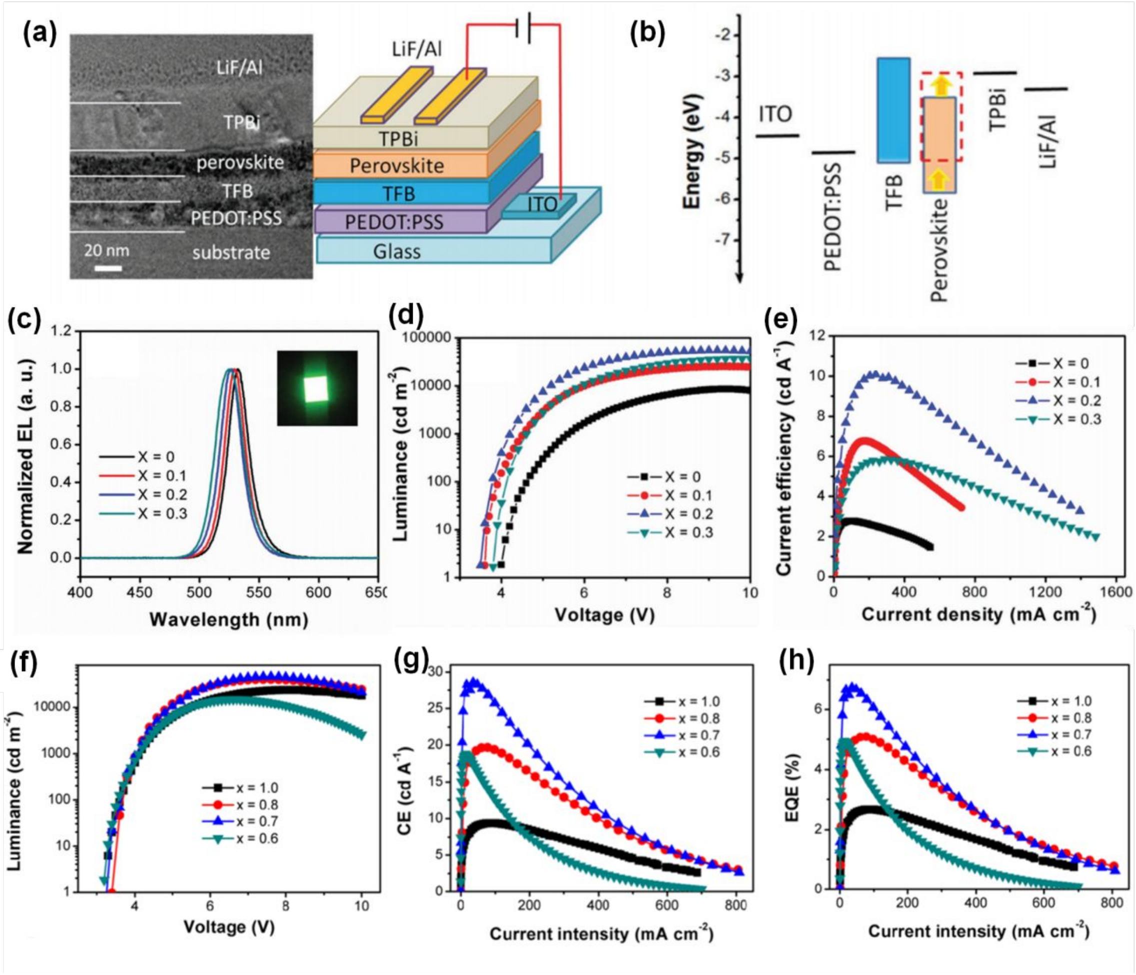

Figure 31. (a) Cross-section SEM image (left) and schematic illustration (right) of the FA$_{(1-x)}$Cs$_x$PbBr$_3$-based perovskite LED device structure. (b) The flat-band energy levels of the different layers in the perovskite LED devices. (c) Electroluminescence (EL) spectra and photograph (inset) of FA$_{(1-x)}$Cs$_x$PbBr$_3$-based perovskite LEDs driven at a bias potential of 4 V. (d) luminance–voltageand (e) current efficiency–current density characteristics of perovskite LEDs, based on FA$_{(1-x)}$Cs$_x$PbBr$_3$ (x = 0, 0.1, 0.2, and 0.3). Reprinted with

permission from Ref. [42], copyright 2017, Wiley-VCH. (f) Luminance−voltage, (g) current efficiency (CE)−current density, and (h) external quantum efficiency (EQE)−current density characteristics of $FA_{0.8}Cs_{0.2}Pb_xBr_3$ less-lead perovskite LEDs (x = 1.0, 0.8, 0.7, and 0.6). Reprinted with permission from Ref. [43], copyright 2018, American Chemistry Society.

B-site doped lead halide perovskite nanocrystals have also been used as the active light emitting layer of LEDs. LED devices made from 2.6 mol % Mn-doped $CsPbBr_3$ and 3.8 mol % Mn-doped $CsPbBr_3$ nanocrystals possessed improved maximum luminance of 9,971 and 9,717 cd m^{-2} under the applied voltages of 6.2 and 6.5 V, respectively. Their pure $CsPbBr_3$ counterpart had a maximum luminance of 7,493 cd m^{-2} under 6.6 V of applied voltage. The EQE and CE values of 2.6 mol % Mn-doped $CsPbBr_3$ device (0.95 % and 4.33 cd/A) and 3.8 mol % Mn-doped $CsPbBr_3$ device (1.49 % and 6.40 cd/A) also outperform the pure $CsPbBr_3$ device (0.81 % and 3.71 cd/A). [378] The EQE and CE values of LED devices made from 7.9 mol % Mn-doped $CsPbI_3$ nanocrystals (0.51 % and 0.07 cd/A) and 21.6 mol % Mn-doped $CsPbI_3$ nanocrystals (1.04 % and 0.15 cd/A) also outperform the pure $CsPbI_3$ device (0.41 % and 0.06 cd/A). [378] Sn^{2+}-doped $CsPbBr_3$ perovskite nanocrystals have also been incorporated in LED devices. The device performance of Sn-doped $CsPbBr_3$ LEDs was found to be closely related to the Sn doping ratio. [223, 226, 233] The best device based on $CsPb_{1-x}Sn_xBr_3$ nanocrystals exhibited a low turn-on voltage of 3.6 V, maximum luminance of 12,500 cd m^{-2} and EQE of 4.13%, representing the best values among Sn-doped LEDs. [223, 230] By varying Ni^{2+} and modulating Cl/Br element ratios, Ni^{2+}-doped $CsPbCl_xBr_{3-x}$ perovskite nanocrystals with tunable emission from 508 to 432 nm were prepared via the supersaturated recrystallization method at room-temperature. As depicted in Figure 32a, a blue-emitting LED (at 470 nm) based on 2.5% Ni^{2+}-doped $CsPbCl_{0.99}Br_{2.01}$ was produced, and displayed a 6-fold improvement of luminance (Figure 32b) and a 20-fold improvement of EQE (Figure 32c) over undoped counterparts. [334] Besides isovalent cation-doping, heterovalent Ce^{3+}-doped perovskite nanocrystals have also been used in LED fabrication. While LED devices with pure $CsPbBr_3$ nanocrystals show maximum CE of 12.5 cd A^{-1} at 4 V and EQE of

1.6% at 4.2 V, LED devices with Ce^{3+}-doped $CsPbBr_3$ nanocrystals (with Ce/Pb ratio of 2.88%) displayed an enhanced maximum CE of 14.2 cd A^{-1} and much higher EQE of 4.4% at 3.8 V, which indicates that the nonradiative recombination has been strongly suppressed via the Ce^{3+}-doping. [302]

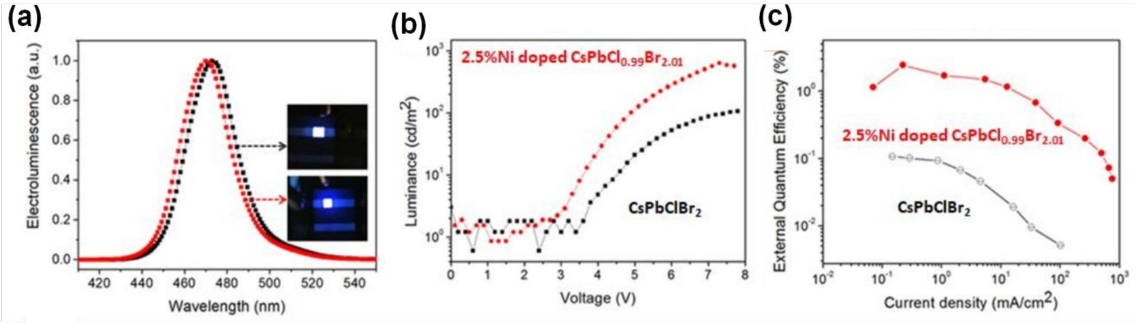

Figure 32. (a) Electroluminescence spectra, (b) brightness, and (c) EQE curves of LEDs based on $CsPbClBr_2$ (black curve) and 2.5% Ni^{2+}-doped $CsPbCl_{0.99}Br_{2.01}$ (red curve) perovskite nanocrystals, respectively. The insets in (a) are photographs of the devices at a voltage of 5V. Reprinted with permission from Ref. [334], copyright 2020, American Chemistry Society.

5-2. Lasers based on Doped or Ion-Substituted Perovskite Nanocrystals

Lead halide perovskites have been intensely investigated as optical gain materials for amplified spontaneous emissions (ASEs) due to their relatively low lasing thresholds and high optical gain. [202, 412] It is particularly challenging to obtain perovskite ASEs in the red region due to the thermodynamic instability of red-emitting iodine-containing perovskites (e.g. $MAPbI_3$, $FAPbI_3$, and $CsPbI_3$). [202] In iodide-based $CsPbX_3$ (X = Br/I) nanocrystal lasing, the lasing threshold increases as the ratio of I/Br increases (i.e., red-shifted) under the same testing conditions. [202] By using $FAPbI_3$ or FA-doped $CsPbI_3$ nanocrystals, one can observe ASEs in compact nanocrystal films deposited on glass substrates under 100 fs pulsed excitation at room temperature. ASEs appear as a narrow band with a FWHM of 10−12 nm and are 50 nm and 30 nm red-shifted fromthe PL maxima of $FAPbI_3$ and $FA_{0.1}Cs_{0.9}PbI_3$ nanocrystals, respectively (Figure 33a and 33b). A lasing threshold of 7.5 μJ cm^{-2}, one of the lowest values among red-to-NIR emitting perovskites, was achieved by 100 nm compact films of $FAPbI_3$ nanocrystals with smooth mirror-like surfaces, obtained by repetitive dip-coatings and 90 °C annealing (Figure 33a). A lasing threshold of 28 μJ cm^{-2} was achieved by films of $FA_{0.1}Cs_{0.9}PbI_3$ nanocrystals obtained by drop-casting and drying at 50 °C (Figure 33b). It was found that perovskite nanocrystal films exhibited lower lasing thresholds when films were prepared under processing conditions that favored the sintering of perovskite nanocrystals (e.g., ligand desorption by repetitive washing steps and/or annealing the films at a higher temperature of 90−100 °C). [202] Lasing from single crystal perovskite nanowires with tunable wavelength have also been studied by controlling the stoichiometry of both cations and anions. $MAPbBr_yI_{3-y}$ and $MAPbCl_xBr_{3-x}$ single crystal nanowires were synthesized by mixing different stoichiometry of iodide and bromide or bromide and chloride precursors, and the corresponding lasing emission coverd from 500 to 790 nm (Figure 33c). [23] Single-crystal $MAPbX_3$ perovskite nanowires exhibit lasing quantum yields approaching 100% with the lowest lasing thresholds (220 nJ cm^{-2}) and highest quality factors (Q factors ~3,600) yet reported for nanowire lasers. [23] Cation alloying $(FA,MA)PbI_3$ and cation/halide double alloying $(FA,MA)Pb(Br,I)_3$ single-crystal nanowires can fill the lasing gap between 580 and 670 nm which cannot be realized by MA-based perovskite nanowires and can further extend the lasing wavelength all the way to 824 nm NIR region (the wavelengths highlighted in the dashed rectangular boxes in Figure 33c). [24] The violet-blue wavelength region (420−490 nm) can be satisfied with wide band gap $CsPb(Br,Cl)_3$ nanowires (Figure 33d). [22] Compared with MA-based lasers, single crystal $FAPbX_3$ nanowire lasers feature red-shifted emission and better thermal stability. [24] Recently, continuous wave (CW) lasers were fabricated from non-stoichiometric Cs, MA and FA mixed cations perovskite thin films,[413] which is worth further studying in nanocrystals form. In addition, single-mode lasers based on $CsPbX_3$ submicron spheres are other interesting devices that merit futher investigation. [414]

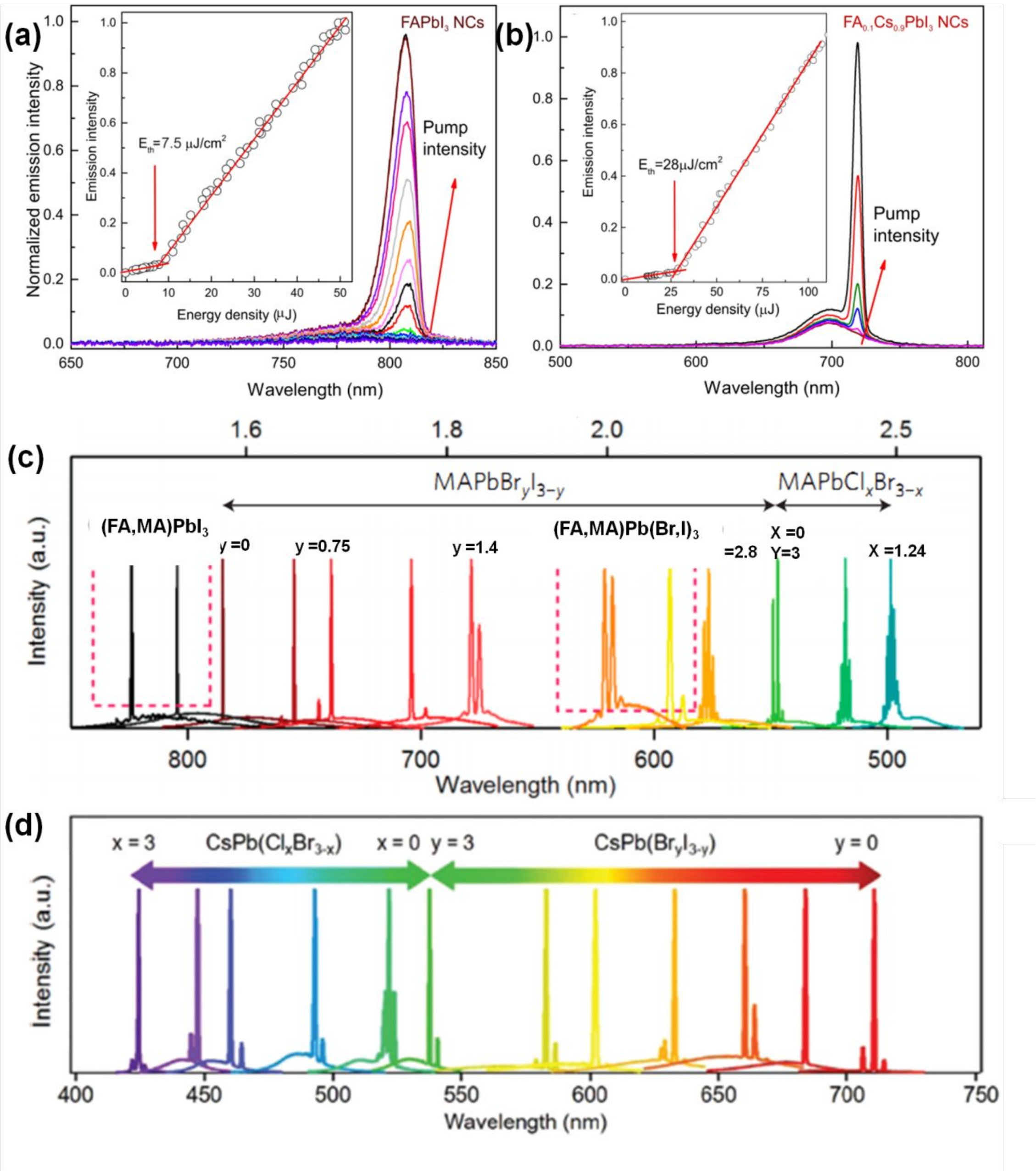

Figure 33. Amplified spontaneous emissions (ASEs) for perovskite compact films prepared from (a) $FAPbI_3$ nanocrystals using dip-coating with heat treatment at 90 °C showing a 50 nm red-shift of ASE from the PL maxima and a lasing threshold of 7.5 μJ cm^{-2} (inset), and (b) $FA_{0.1}Cs_{0.9}PbI_3$ nanocrystals using simple drop-casting and heat treatment at 50 °C dispaying a 30 nm red-shift of ASE from the PL maxima and a lasing threshold of 28 μJ cm^{-2} (inset). Reprinted with permission from Ref. [202], copyright 2017, American Chemistry Society. (c) Tunable lasing emission wavelength of single-crystal

MA-based perovskite nanowires with mixed halids. The wavelengths marked inside dashed rectangular boxes were obtained from MA-doped FA-based perovskite nanowires. Reprinted with permission from Ref. [24], copyright 2016, American Chemistry Society. (d) Tunable lasing emission wavelength of single-crystal Cs-based perovskite nanowires with mixed halids. Reprinted with permission from Ref. [22], copyright 2016, American Chemistry Society.

5-3. Solar Cells based on Doped or Ion-Substituted Perovskite Nanocrystals

Perovskite solar cells have witnessed a rapid increase in power conversion efficiency (PCE) and long-term stability over the past decade. [415] Doping with different cations in the A-site and incorporating different halids in the X-site have been regarded as feasible strategies for substantially enhancing the stability and PCE of film-based perovskite solar cells. [416] Doped perovskite nanocrystals have also been extensitvely studied in photovolatic applications. Though Sn-based perovskite solar cells are unstable due to easy oxidation, alloyed $CsSn_{1-x}Pb_xI_3$ nanocrystals possess far superior phase-stability to both parent $CsSnI_3$ and $CsPbI_3$ nanocrystals (degradation over months, not days). [10] Photoexcited electrons from alloyed $CsSn_{1-x}Pb_xI_3$ nanocrystals can be injected into TiO_2 at a fast rate of 1.12×10^{11} s^{-1}, which may facilitate high photocurrent generation when applied in solar cells. As a proof of concept, alloyed $CsSn_{1-x}Pb_xI_3$ nanocrystals have been employed as the sensitizer in a quantum dot-sensitized solar cell (QDSC) configuration, with the use of liquid-state iodide/triiodide (I^-/I_3^-) electrolyte. The device delivered a short-circuit current (J_{sc}) of 10.13 mA/cm^2, open-circuit voltage (V_{oc}) of 0.63 V, fill factor (FF) of 0.46, and an overall power conversion efficiency (PCE) of 2.9%. [10] $CsSnI_{2.95}F_{0.05}$ with and without SnF_2 doping have been used to replace the liquid-state iodide/triiodide (I^-/I_3^-) electrolyte in the dye-sensitized solar cell (DSSC) and serves as the hole conduction layer to realize a novel all-solid-state photovoltaic cell structure. [242] $CsSnX_3$ quantum rods synthesized by solvothermal process have also been used as the absorbing layer to fabricate solar cells, and those devices reached power conversion efficienies of 9.66%, 10.46%, and 12.96% from $CsSnCl_3$, $CsSnBr_3$, and $CsSnI_3$ devices, respectively. [235]

Solar cells based on colloidal perovskite nanocrystals generally have the following structure: a transparent conductive oxide (TCO) substrate (e.g., indium tin oxide (ITO) or fluorine-doped tin oxide (FTO))/electron transport layer (ETL) (e.g., TiO_2 or SnO_2)/perovskite active layer/hole transport layer (HTL) (generally Spiro-OMeTAD)/metal contact electrode (e.g., Au or Al). [8, 9] When employing colloidal quantum dots or nanocrystals in solar cell devices, the insulating ligands on the surface of colloidal nanocrystals are considered to be a major limiting factor. Due to the ionic nature of perovskite nanocrystals, the polarity of the antisolvent used for nanocrystal surface treatment needs to be deliberately chosen in order to remove the surface ligands without damaging the integrity of the nanocrystals. Water, methanol, ethanol, and isopropanol are classified as "grade I" solvents that can completely destroy the ionic bonds in $FAPbI_3$ nanocrystals; t-butanol, 2-pentanol, acetonitrile/toluene (v:v 2:3), and ethyl acetate are classified as "grade II" solvents that can gradually remove the surface ligands without destroying the integrity of $FAPbI_3$ nanocrystals; and chlorobenzene, toluene, octane, and hexane are classified as "grade III" solvents that are not able to remove the surface ligands on $FAPbI_3$ nanocrystals. [9] Therefore, a photovoltaic device using $FAPbI_3$ colloidal quantum dots (CQD) as a photoactive layer (Figure 34a) was fabricated by employing a set of three different "grade II" solvents with gradually reducing polarity, and the ligand density can be sequentially decreased while maintaining the integrity of $FAPbI_3$ nanocrystals. The J_{sc}, V_{oc}, and external quantum efficiency (EQE) of the $FAPbI_3$ CQD-based solar cell gradually increased after each surface treatment cycle due to the progressive removal of insulating surface ligands (Figure 34b and 34c). [9] A maximum PCE of 8.38 % was achieved with a J_{sc}, of 11.84 mA/cm^2, a V_{oc} of 1.10 V and a FF of 0.64. It is worth noting that the high defect tolerance of perovskite materials accounts for the large V_{oc} of $FAPbI_3$ CQD-based solar cells, which in turn leads to favorable carrier transport.

In addition to removing the surface ligands using polarity controlled antisolvents, one can also boost solar cell performance by post-treatment with an A-site cation halide salt (AX, where A = formamidinium (FA^+), methylammonium (MA^+), or cesium (Cs^+) and X = I^- or Br^-). [8] Postsynthetic addition of A-site cation halide salts (AX) (such as formamidinium iodide (FAI)) has been shown to improve the coupling between nanocrystals, passivate the surface, tune the device energetics, and improve stability of perovskite solar cells. A perovskite solar cell was fabricated by sequentially deposited $CsPbI_3$ nanocrystal film via a spin coating method. The film was immersed in a saturated lead(II) nitrate $[Pb(NO_3)_2]$ solution in methyl acetate (MeOAc) after each coating to partially remove the native ligands and allow for further layers to be deposited without re-dispersing the existing layers. After three to four deposition cycles, a $CsPbI_3$ nanocrystal film with a thickness of 200 to 400 nm was built and then immersed in a saturated AX salt solution in ethyl acetate (EtOAc) for ~10 s to yield AX coated $CsPbI_3$ active layer (Figure 34d). The highest PCE of 13.4% was obtained by FAI treatment with a J_{sc} of 14.37 mA/cm^2, which was significant higher than that of treatment in pure EtOAc (9.22 mA/cm^2). Notably, other AX salt (i.e., FABr, MAI, MABr, CsI) treatments also displayed improved J_{sc} over the control (i.e., pure EtOAc treatment) (Figure 34e). However, all AX salt treatments displayed little impact on the V_{oc} (1.17~1.22), FF (0.78~0.82), and EQE onset (~700 nm) (Figure 34f), indicating the improvement of PCE is largely attributed to the increased J_{sc}. The possible reason for the increased J_{sc} was found to be related to the higher charge carrier collection efficiency in the $CsPbI_3$ quantum dot films after post-treatment by AX salts. [8] Despite the fact that solar cells made from FAI-coated $CsPbI_3$ nanocrystals outperformed neat $CsPbI_3$ nanocrystals in the abovementioned study, the devices fabricated from $Cs_{1-x}FA_xPbI_3$ mixed A-site perovskite nanocrystals did not perform better than those made with $CsPbI_3$ nanocrystals. [417] Notably, surface passivation seems to play a more important role than alloying in nanocrystals-based perovskite solar cells. For instance, solar cells based on $CsPbI_3$ nanocrystals with a GeI_2 additive showed better stability than the ones without GeI_2, which was believed to be due to the efficient surface passivation of the quantum dots upon the addition of GeI_2. [418] It is notable that the best performance research cells reported by the National Renewable Energy Laboratory (NREL) [49] are all mixed perovskite cells, either employing mixed cations or mixed anions. This is likely because light absorbing films grown under iodine-rich conditions are prone to a high density of deep electronic traps, which act as recombination centers. Thus the use of bromide or chloride precursors mitigate or suppress the formation of these key defects. [144] It is important to note that although the PCEs attained from nanocrystal-based perovskite solar cells have not exceeded those of film-based cells due to the insulating ligands that results in the lower J_{sc}, the V_{oc} accessed by nanocrystal-based devices possesses a lower V_{oc} loss than film-based cells and is closer to the theoretical thermodynamic limit of single-junction cells based on the Shockley−Queisser (SQ) analysis. [417]

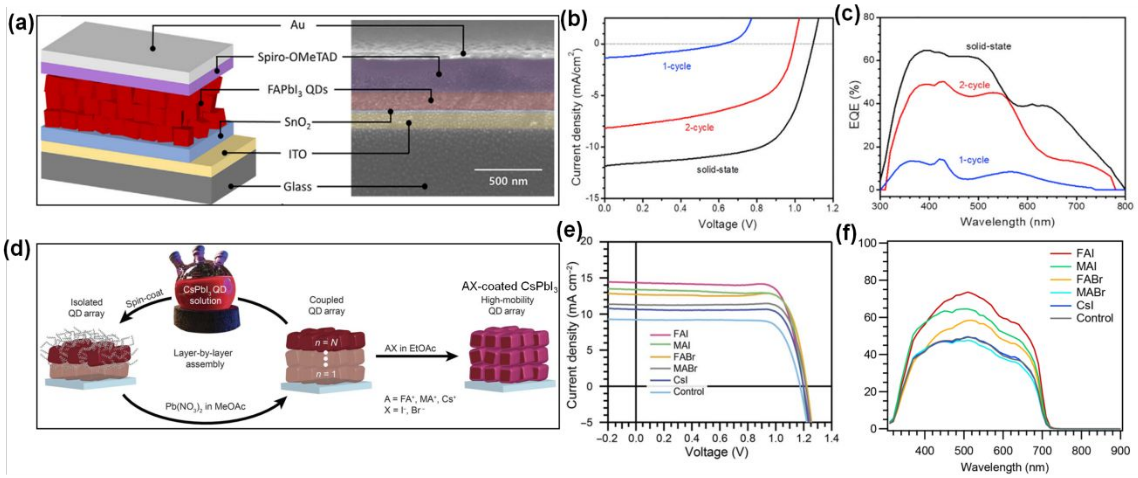

Figure 34. (a) Schematic of the $FAPbI_3$ nanocrystals-based solar cell device structure and the corresponding device cross-sectional SEM image. (b) Current density-voltage (J-V) curves, and (c) external quantum efficiency (EQE) curves of the devices based on $FAPbI_3$ colloidal nanocrystals with increasing cycles of surface treatment (two cycles in solution phase and one cycle in solid state). Reprinted with permission from Ref. [9], copyright 2018, Elsevier. (d) Schematic of layer-by-layer deposition process of $CsPbI_3$ nanocrystal film and the AX salt post-treatment. (e) J-V characteristics and (f) EQE curves of $CsPbI_3$ nanocrystals-based devices treated with different AX salts. Reprinted with permission from Ref. [8], copyright 2017, American Association for the Advancement of Science.

5-4. Energy Down-Conversion Coatings based on Doped or Ion-Subtituted Perovskite Nanocrystals

In addition, doped perovskite nanoscrystals can also be utilized as energy converting coating. For example, Mn-doped $CsPbCl_3$ (or $CsPbCl_3$:Mn) nanocrystals were used as energy down-converters to change the normally un-harvestable ultraviolet (UV) radiation (wavelengths 300−400 nm) into harvestable visible light. [67] $CsPbCl_3$:0.1Mn (meaning 10% Mn substitution) nanocrystals were synthesized via a hot-injection method by swiftly injecting Cs-oleate precursor into a mixture of $PbCl_2$ and $MnCl_2$. These $CsPbCl_3$:0.1Mn nanocrystals displayed a large Stokes shift (>200 nm) and had yellow emission centered at ~590 nm. The Stokes shift can be explained by the energy transferred from the conduction band (CB) of $CsPbCl_3$ host to Mn^{2+} ions via $^4T_1$−$^6A_1$ transition. [67] Different concentrations of $CsPbCl_3$:0.1Mn nanocrystal solutions were spin-coated onto the transparent side of $CH_3NH_3PbI_3$ perovskite solar cells (Figure 35a), and it was found that devices with the optimized concentration of 5 mg/mL saw a 3.34% improvement in PCE (increased from 17.97% to 18.57%) (Figure 35b). Devices coated with $CsPbCl_3$:0.1Mn nanocrystal also showed enhanced stability, illustrated by their 97% retention of initial PCE after 100 h of continuous UV LED irradiation while the PCE for devices without coating dropped to 85% of its initial efficiency (Figure 35c). It is possible that the energy-down-converting $CsPbCl_3$:0.1Mn coating can reduce the UV-induced degradation and therefore improve the device stability. [67] Similar down-converting coating strategies have also been applied in photodetectors. The UV response of photodetectors can be markedly enhanced by depositing a layer of colloidal $CsPbX_3$ perovskite nanocrystals on the surface and tuning the PL emission wavelength via the halide composition to fall within the maximal EQE response region of the detector. [16]

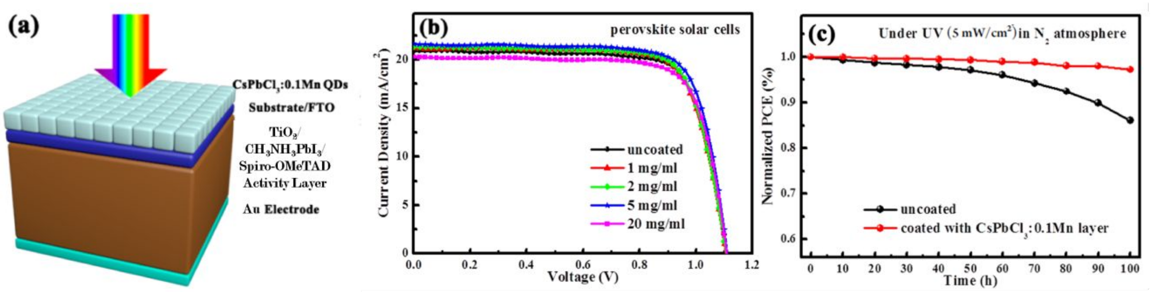

Figure 35. (a) Schematic structure of a $CH_3NH_3PbI_3$ perovskite solar cell coated with a layer of $CsPbCl_3$:0.1Mn nanocrystals. (b) Current density−voltage curves for reference and perovskite solar cells assisted with a coating of $CsPbCl_3$:0.1Mn nanocrystals with different

coating concentrations (associated with different coating layer thicknesses). (c) Aging test results of the reference perovskite solar cell and $CsPbCl_3$:0.1Mn nanocrystal-coated cell under continuous UV irradiation (5 mW/cm^2) for 100 h in a N_2 atmosphere. Reprinted with permission from Ref. [67], copyright 2017, American Chemistry Society.

5-5. Color Conversion Coatings based on Doped or Ion-Substituted Perovskite Nanocrystals

Similar to the above application as energy down-converters from UV to visible light, perovskite nanocrystals can also be used as down-conversion luminescent phosphors by down converting light from blue LED chips into different visible light (green, yellow, orange, or red) to obtain desired color temperature white lights for lighting or display applications. [68-71] Green emitting $Cs_{0.1}FA_{0.9}PbBr_3$ and red emitting $Cs_{0.1}FA_{0.9}PbBr_{1.5}I_{1.5}$ mixed-cation perovskite nanocrystals-PMMA polymer composite films have been used as color converters on a blue LED chip to achieve white light LED. [419] Likewise, a bright pure white light-emitting device (WLED), with corresponding CIE color coordinate (0.31, 0.34) (note that pure white light is (0.33, 0.33)), was assembled by stacking a 10% Mn-doped $CsPbCl_3$/PMMA composite film as an orange-red emitting layer, a $CsPbBr_3$/PMMA composite film as a green-emitting layer, and a $CsPbCl_{1.5}$ $Br_{1.5}$/PMMA composite film as a blue-emitting layer on top of a 396 nm UV LED chip (Figure 36). [420] The orange-red emission from the Mn-doped perovskite nanocrystals can be used as color conversion coatings by mixing dual emission Mn-doped $CsPbCl_3$ or Mn-doped $CsPb(Cl/Br)_3$ nanocrystals with polymer and depositing these polymer-nanocrystals composites on the surface of blue LED chips. [257, 261] In order to achieve the desired color temperature from these dual emission Mn-doped nanocrystals, sometimes it is crucial to fine tune the host perovskite emission peak position (by tuning the ratio of Cl/Br content) as well as the relative peak intensity ratio between the host perovskite emission and the dopant Mn emission. This complex design is sometimes difficult to achieve during the synthesis process and may need to be further fine-tuned through postsynthetic processes. By utilizing the distinct exchange rates of the cation (slow) and anion (fast) and control (terminate) the ion exchange by purification at different reaction times, one can easily obtain the desired color temperature from these Mn-doped $CsPb(Cl/Br)_3$ nanocrystals. [421] For lighting or display applications it is beneficial to choose a phosphor material that has a larger Stokes shift (which means there is a significant difference between the absorption and emission peak) to minimize the potential for self-absorption. $MA_3Bi_2X_9$ and $Cs_3Bi_2X_9$ systems both show a slightly larger Stokes shift, which makes them prime candidates for lighting applications. [355]

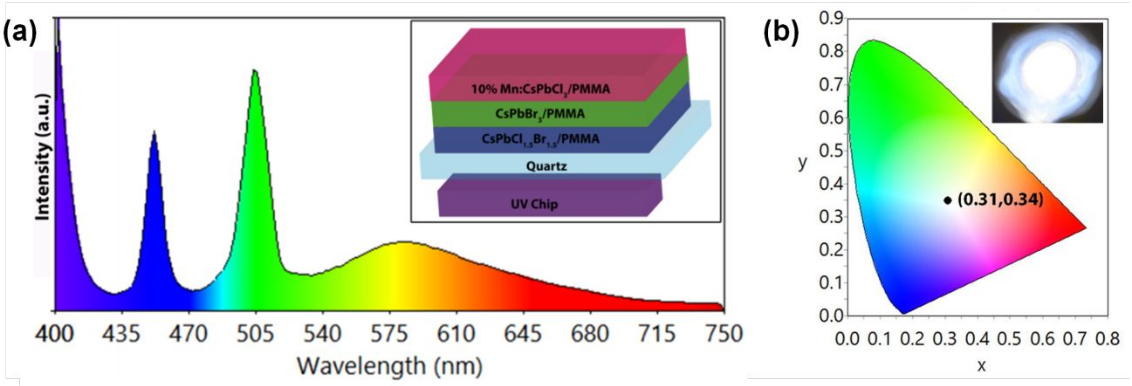

Figure 36. (a) EL spectrum of a WLED device based on a 10% Mn-doped $CsPbCl_3/CsPbBr_3/CsPbCl_{1.5}Br_{1.5}$ nanocrystals/PMMA composite film on top of a 396 nm UV LED chip. The device structure is shown as an inset. (b) Chromaticity diagram of the CIE coordinates of the WLED and its digital photograph (inset). Reprinted with permission from Ref. [420], copyright 2020, Elsevier.

There are many other applications that have capitalized on either colloidal perovskite nanocrystals or doped perovskite nanocrystals, such as $CsPbI_3$-based photodiodes, [12] Cs_2SnI_6 and Ag-doped $CsPbBr_3$-based FETs, [237, 326] $CsPbCl_3$/graphene and $FA_xMA_{1-x}PbI_3/MoO_x$ FET heterojunction photodetectors, [18, 422] $CsPbX_3$-based X-ray detection scintillators, [75] Yb^{3+}-doped $CsPbCl_3$ luminescent solar concentrators (LSCs), [307, 308] chemical probes for TNP, TOAX, or HCl detections, [72-74] hydrogen (H_2) generation, [76] photocatalytic CO_2 reduction, [77-83] fluorescent inks for anti-counterfeit/encryption printing purposes, [84-86] and luminescence probes for bioimaging applications. [87]

6. Summary and Outlooks

This review summarized the general background of perovskite nanocrystals, discussed the fundamentals of doping and ion substitution in the A-, B-, and X- site of ABX_3 type 3D perovskite nanocrystals, examined their stability, and outlined their applications. Particularly, various dopants and doping strategies have been discussed as summarized as follows: First, for A-site doping, Cs, MA, and FA are the three commonly used cations that can sustain stable 3D perovskite structure. The size and optical properties of MA lie in between those of FA and Cs cations. Introducing smaller Cs cations contracts the lattice and reduces the cubo-octahedral volume, thereby inducing stronger interaction between the cations and halides which increases (i.e. blue-shifts) the band gap, and in turn facilitates the formation of highly crystalline perovskite crystals at a low temperature. In contrast, incorporating larger FA cations causes lattice expansion, achieves a tolerance factor closer to 1, and forms hydrogen bonds which stabilize the pseudocubic structure, thus resulting in superior solar cell performance due to red-shifted absorption (i.e., reduced band gap) and improved charge transport. Moreover, Rb and Tl have also been used for A-site doping and exhibited a relatively lower PLQY. Second, for B-site doping, partial substitution of Pb^{2+} with a smaller B-site cations reduces the B-X bond length and stabilizes the lead iodide perovskite by reducing the extent of octahedral rotation or distortion, leading to: a larger tolerance factor (improved phase stability), a larger formation energy (improved thermal stability), and reducing the toxic lead content at the same time. Sn^{2+}-containing perovskite nanocrystals display relatively red-shifted optical properties (compared with their Pb-based counterparts) due to higher Pauling electronegativity for Sn^{2+} than Pb^{2+} ions. However, Sn^{2+} easily oxidizes to Sn^{4+} causing their persistent instability. Intriguingly, Mn-doping and lanthanide-doping both demonstrate multi-peak emission with PL peaks related to transitions from energy levels of the dopant ions. Depending on the dopant levels, Mn^{2+}-doped perovskites possess a dopant PL at ~600 nm while Yb^{3+}-doped perovskites show a dopant PL at ~1000 nm with PLQY exceeding 100%

due to the quantum-cutting effect. Notably, metal(II) halide salts (MX_2) have been commonly employed for isovalent substitutions such as doping alkaline-earth metals and transition metals, and have various impacts based on the size of the metal ions. Furthermore, heterovalent substitutions also exert very different influences, depending on the ion used, and occasionally may produce structures other than ABX_3 (e.g., $A_3B_2X_9$ or $A_2B'B''X_6$) in order to satisfy charge neutrality. Finally, for X-site doping, halide substitution has been widely exploited for tailoring the band gap of perovskite nanocrystals as it can readily change the optical responses throughout the whole visible range (~300 nm); this contrasts greatly the range that can be tuned via the quantum confinement effect (only roughly 100 nm). In particular, the incorporation of Cl^- or I^- anions blue-shifts or red-shifts the optical properties of Br^--based perovskite nanocrystals, respectively. It is also noteworthy that SCN^--doped and chalcohalide split-anion perovskites have been investigated in thin film solar cells yet are relatively new for colloidal nanocrystals.

Doping and ion substitution has been shown to alter the optical properties of perovskite nanocrystals, improve their stability, and reduce their toxic lead content. The extremely high PLQY, ease of synthesis, and the potential of roll-to-roll printing or low temperature solution mass production of perovskite nanocrystals render them as promising candidates for next-generation optoelectronic devices. Nonetheless, for commercialization of perovskite nanocrystals-based materials and devices, a few issues merit further investigation and improvement. The major challenges facing perovskite nanocrystals include: increasing stability, [423] broadening the bandgap (i.e., extension of absorption from visible to UV and NIR), eliminating toxic lead content, [424] minimizing phase segregation (ion migration and hysteresis), [194, 425] and reducing self-absorption (i.e., increasing Stokes shift). [426, 427] Peculiarly, the stability remains a key issue among all challenges, including colloidal stability, color stability, structural stability, phase stability, photo (UV) stability, thermal stability, as well as moisture and air stability. [428] Generally, the stability of colloidal perovskite nanocrystals could be largely raised by the following strategies: (1) Deliberate selection of low polarity solvent/anti-solvent and stronger binding ligands to minimize the detachment of ligands and reduce the number of surface defects. [429] (2) Encapsulation via creating core-shell (or core/shell 1/shell 2) structures or impregnating in water resistant organic or inorganic matrix to prevent direct contact with the surrounding environment and passivate surface defect sites. [430] (3) Intrinsic structural engineering (e.g. compositional tuning, double perovskite, or other low-dimensional structures) to tailor the tolerance factor and thus enhance the formation energy. The desorption of surface ligands during washing is recognized as one of the main causes for the instability in colloidal perovskite nanocrystals. Stronger binding ligands such as multidentate ligands (e.g., compounds with concurrent polyamine and polyacid functional groups), [431] pre-formed alkylammonium halide salts, [432, 433] or ligated star-like polymer nanoreactors [99, 100] represent promising research directions for enhanced stability. [434] Seeking alternative solvents that do not require the removal of solvent prior to employing nanocrystals for applications may stand out as the other possible research effort to avoid ligand detachment. [435]

We note that the general research endeavors towards mixed-cation/anion colloidal metal halide perovskite nanocrystals practically follow that of thin film perovskites, including multi-site ion substitutions (i.e., simultaneous substitution of A-site & B-site ions, e.g., (FA/Cs)(Pb/Sn)X_3 [436] and (MA/FA)(Pb/Sn)X_3 [437, 438]; A-site & X-site ions, e.g., (FA/Cs)Pb(I/Br)$_3$ [203, 204, 439] and (FA/MA)Pb(I/Br)$_3$ [201, 440-442]; or B-site & X-site ions, e.g., MA(Pb/Sn)(I/Br)$_3$ [443] and MA(Pb/Sn)(I/Cl)$_3$ [444]), and can be further expanded to concurrent substitution of all three sites (A-site, B-site, and X-site) such as (FA/MA)(Pb/Zn)(I/Br)$_3$ [445]. Triple-cation perovskite (e.g., (Cs/MA/FA)PbX_3 [446-448] and (K/MA/FA)PbX_3 [449]) and quadruple-cation perovskite (e.g., (Rb/Cs/MA/FA)PbX_3 [156, 447, 448] and (K/Cs/MA/FA)PbX_3 [450]) have already been widely studied in thin film solar cells to improve device performance, enhance thermal stability, and reduce hysteresis. Nonetheless, to date no colloidal perovskite nanocrystals based on triple- or quadruple-cation have been synthesized. Exotic A-site cations $C_4H_9NH_3^+$ (n-butylammonium, BA), [451] $(CH_2)_3NH_2^+$ (azetidinium, Az), [452] $C_2H_4(NH_3)_2^{2+}$ (ethylenediamine, EDA^{2+}), [453] $C(NH_2)_3^+$ (guanidinium, Gua), [454] $C_6H_{13}NH_3^+$ (n-hexylammonium, HA), [455] $C_8H_9NH_3^+$ (phenylethylammonium, PEA), [456] thiourea (TU), [457] and aromatic derivatives (R-NH_3^+, where R is naphthalene, fluorine, anthracene, pyrene, or perylene) [458-460]) have been exercised in mixed-cation perovskite thin film solar cells. However, the synthesis in the form of perovskite nanocrystals containing these A-site cations noted above has not yet been explored. This represents an important area and can be pursued. It is worth noting that the incorporation of some of these complex yet bigger organic cations may induce low-dimensional (quasi-2D layered, 2D, 1D, and 0D) structures instead of 3D structure.

On the other hand, the concrete mechanisms of doping and ion substitution remain elusive and merits more thorough investigation. For example, it is challenging to pinpoint the exact location or distribution of the dopant within the host matrix. To this end, it invokes a combination of several different techniques such as X-ray photoelectron spectroscopy (XPS), extended X-ray absorption fine structure (EXAFS) spectroscopy, and high-resolution synchrotron XRD, in conjuncton with the first-principles calculations to clarify the underlying doping mechanism. [328] The ability to scrutinize the actual position of dopant ions in the lattice is the key to derive accurate conclusions. For example, when adding metal halide salts (e.g., $SbCl_3$, $BiCl_3$, VCl_3, $NiCl_2$, $ZnCl_2$, $SnCl_2$, $SnCl_4$, $PbCl_2$, and CuCl) as dopants to $CsPbCl_3$ nanocrystals, the difference in the PLQY enhancements are not due to the doping of these dissimilar metal ions, yet because of the varied ability of these metal salts to release active chloride ions for surface passivation, as proven by control experiments with metal acetate salts showing no increase in the PLQY. [433]

Investigation into the PL decay kinetics is also of key importance in determining how surface defects, functioning as recombination centers, affect the PLQY of perovskite nanocrystals. For instance, a biexponential PL decay transforming to a monoexponential decay signifies the efficient passivation of surface defects. [327, 461] Transient absorption, time-resolved PL, and time-resolved fluorescence quenching spectroscopies represent some roubust techniques to explore the energy transfer process in perovskite nanocrystals, including examining the exciton diffusion length and probing the energy transfer rate between neighboring nanocrystals. Nonetheless, these are critical measurements to identify whether these nanocrystals are suitable to be utilized in certain applications. [462] Such fundamental studies may also be beneficial for improving the PLQY of Cl-based and lead-free perovskite nanocrystals as they possess low PLQY. [335] The ferroelectric and piezoelectric properties of perovskite nanocrystals and their corresponding applications may also be worth further study. [463]

Colloidal nanocrystals afford many unique tunable physical properties rendered by the control over their size, shape, architecture (e.g., core-shell structure, Janus structure, nanowire/nanorod, etc.), and surface capping ligands. Clearly, advanced architecture engineering integrated with composition tailoring may constitute a future research direction. For example, some interesting future exploration may involve doping one material in the core and doping the other material in the shell in core/shell nanocrystals [464] or doping two dissimilar materials of interest in the respective half of a Janus nanostructures (e.g., Janus nanoparticles and nanorods) to yield interesting polarized optic or catalytic effects. [465] In addition to fine tuning the doping condition to improve the doping efficiency, the ability to capitalize on doping and ion substitution to alter the optoelectronic properties, enhance the stability, and reduce the toxicity of colloidal metal halide perovskite nanocrystals makes them very appealing for broadened use in many future applications. For instance, due to the ease of wavelength tuning and near unity PLQY, perovskite nanocrystals are ideal candidates as luminescence probes for bioimaging. [87-94] Unfortunately, only toxic lead-containing perovskite nanocrystals are found to possess a sufficiently high PLQY, with safer lead-free perovskite nanocrystals usually displaying a relatively low PLQY. Doped or ion-substituted perovskite nanocrystals with lower cytotoxicity yet retaining high PLQY may stand out as outstanding alternatives for use in bioimaging when they are well-encapsulated within water-resistance matrix.

Acknowledgments: This work is supported by by the AFOSR (FA9550-19-1-0317), the NSF (CMMI 1914713, DMR 1903990 and ECCS 1914562), and the DOD-DTRA (HDTRA1-18-1-0004).

References

1. Seth, S. and A. Samanta, *A Facile Methodology for Engineering the Morphology of $CsPbX_3$ Perovskite Nanocrystals under Ambient Condition.* Scientific Reports, 2016. **6**: p. 37693.
2. Sun, S., et al., *Ligand-Mediated Synthesis of ShapeControlled Cesium Lead Halide Perovskite Nanocrystals via Reprecipitation Process at Room Temperature.* ACS Nano, 2016. **10**: p. 3648-3657.

3. Liang, Z., et al., *Shape-Controlled Synthesis of All-Inorganic $CsPbBr_3$ Perovskite Nanocrystals with Bright Blue Emission.* ACS Appl. Mater. Interfaces, 2016. **8**: p. 28824-28830.
4. Udayabhaskararao, T., et al., *Nucleation, Growth, and Structural Transformations of Perovskite Nanocrystals.* Chem. Mater. , 2017. **29**: p. 1302-1308.
5. Protesescu, L., et al., *Nanocrystals of Cesium Lead Halide Perovskites ($CsPbX_3$, X = Cl, Br, and I): Novel Optoelectronic Materials Showing Bright Emission with Wide Color Gamut.* Nano Lett., 2015. **15**(6): p. 3692-3696.
6. Tyagi, P., S.M. Arveson, and W.A. Tisdale, *Colloidal Organohalide Perovskite Nanoplatelets Exhibiting Quantum Confinement.* J. Phys. Chem. Lett., 2015. **6**: p. 1911-1916.
7. Swarnkar, A., et al., *Quantum dot-induced phase stabilization of α-$CsPbI_3$ perovskite for high-efficiency photovoltaics.* Science, 2016. **354**(6308): p. 92-95.
8. Sanehira, E.M., et al., *Enhanced mobility $CsPbI_3$ quantum dot arrays for record-efficiency, high-voltage photovoltaic cells.* Science Advances 2017. **3**(10): p. eaao4204.
9. Xue, J., et al., *Surface Ligand Management for Stable $FAPbI_3$ Perovskite Quantum Dot Solar Cells.* Joule, 2018. **2**(9): p. 1866-1878.
10. Liu, F., et al., *Colloidal Synthesis of Air-Stable Alloyed $CsSn_{1-x}Pb_xI_3$ Perovskite Nanocrystals for Use in Solar Cells.* J. Am. Chem. Soc., 2017. **139**: p. 16708-16719.
11. Ramasamy, P., et al., *All-inorganic cesium lead halide perovskite nanocrystals for photodetector applications.* Chem. Commun., 2016. **52**: p. 2067-2070.
12. Sim, K.M., et al., *Phase Stabilized α-$CsPbI_3$ Perovskite Nanocrystals for Photodiode Applications.* Laser Photonics Rev. , 2018. **12**: p. 1700209.
13. Zhou, L., et al., *Insight into the effect of ligand-exchange on colloidal $CsPbBr_3$ perovskite quantum dot/mesoporous-TiO_2 composite-based photodetectors: much faster electron injection.* J. Mater. Chem. C, 2017. **5**: p. 6224-6233.
14. Zhou, L., et al., *All-inorganic perovskite quantum dot/mesoporous TiO_2 composite-based photodetectors with enhanced performance.* Dalton Trans., 2017. **46**: p. 1766-1769.
15. Dong, Y., et al., *Improving All-Inorganic Perovskite Photodetectors by Preferred Orientation and Plasmonic Effect.* small 2016. **12**(40): p. 5622-5632.
16. Lu, J., et al., *Ultrafast Solar-Blind Ultraviolet Detection by Inorganic Perovskite $CsPbX_3$ Quantum Dots Radial Junction Architecture.* Adv. Mater., 2017. **29**: p. 1700400.
17. Jang, D.M., et al., *Ultrasound synthesis of lead halide perovskite nanocrystals.* J. Mater. Chem. C, 2016. **4**: p. 10625-10629.
18. Gong, M., et al., *High-Performance All-Inorganic $CsPbCl_3$ Perovskite Nanocrystal Photodetectors with Superior Stability.* ACS Nano, 2019. **13**: p. 1772-1783.
19. Wang, Y., et al., *All-Inorganic Colloidal Perovskite Quantum Dots: A New Class of Lasing Materials with Favorable Characteristics.* Adv. Mater., 2015. **27**: p. 7101-7108.
20. Yakunin, S., et al., *Low-threshold amplified spontaneous emission and lasing from colloidal nanocrystals of caesium lead halide perovskites.* Nature Communications, 2015. **6**: p. 8056.
21. Xu, Y., et al., *Two-Photon-Pumped Perovskite Semiconductor Nanocrystal Lasers.* J. Am. Chem. Soc., 2016. **138**: p. 3761-3768.
22. Fu, Y., et al., *Broad Wavelength Tunable Robust Lasing from Single-Crystal Nanowires of Cesium Lead Halide Perovskites ($CsPbX_3$, X = Cl, Br, I).* ACS Nano, 2016. **10**: p. 7963-7972.
23. Zhu, H., et al., *Lead halide perovskite nanowire lasers with low lasing thresholds and high quality factors.* Nature Materials, 2015. **14**: p. 636-642.
24. Fu, Y., et al., *Nanowire Lasers of Formamidinium Lead Halide Perovskites and Their Stabilized Alloys with Improved Stability.* Nano Lett., 2016. **16**: p. 1000-1008.

25. Lin, C.H., et al., *Large-Area Lasing and Multicolor Perovskite Quantum Dot Patterns.* Adv. Optical Mater., 2018. **6**: p. 1800474.
26. Song, J., et al., *Quantum Dot Light-Emitting Diodes Based on Inorganic Perovskite Cesium Lead Halides ($CsPbX_3$).* Adv. Mater., 2015. **27**(44): p. 7162-7167.
27. Ling, Y., et al., *Bright Light-Emitting Diodes Based on Organometal Halide Perovskite Nanoplatelets.* Adv. Mater., 2016. **28**: p. 305-311.
28. Zhang, X., et al., *Enhancing the Brightness of Cesium Lead Halide Perovskite Nanocrystal Based Green Light-Emitting Devices through the Interface Engineering with Perfluorinated Ionomer.* Nano Lett., 2016. **16**: p. 1415-1420.
29. Li, G., et al., *Highly Efficient Perovskite Nanocrystal Light-Emitting Diodes Enabled by a Universal Crosslinking Method.* Adv. Mater. , 2016. **28**: p. 3528-3534.
30. Huang, H., et al., *Emulsion Synthesis of Size-Tunable $CH_3NH_3PbBr_3$ Quantum Dots: An Alternative Route toward Efficient Light-Emitting Diodes.* ACS Appl. Mater. Interfaces 2015. **7**: p. 28128-28133.
31. Du, X., et al., *High-quality $CsPbBr_3$ perovskite nanocrystals for quantum dot light-emitting diodes.* RSC Adv., 2017. **7**: p. 10391-10396.
32. Sun, H., et al., *Chemically Addressable Perovskite Nanocrystals for Light-Emitting Applications.* Adv. Mater., 2017. **29**: p. 1701153.
33. Pan, J., et al., *Highly Efficient Perovskite-Quantum-Dot Light-Emitting Diodes by Surface Engineering.* Adv. Mater., 2016. **28**: p. 8718-8725.
34. Li, J., et al., *50-Fold EQE Improvement up to 6.27% of Solution-Processed All-Inorganic Perovskite $CsPbBr_3$ QLEDs via Surface Ligand Density Control.* Adv. Mater., 2017. **29**: p. 1603885.
35. Xing, J., et al., *High-Efficiency Light-Emitting Diodes of Organometal Halide Perovskite Amorphous Nanoparticles.* ACS Nano, 2016. **10**: p. 6623-6630.
36. Kumar, P., et al., *Quantum Confinement Effects in Organic Lead Tribromide Perovskite Nanoparticles.* J. Phys. Chem. C, 2016. **120**: p. 18333-18339.
37. Sadhanala, A., et al., *Blue-Green Color Tunable Solution Processable Organolead Chloride-Bromide Mixed Halide Perovskites for Optoelectronic Applications.* Nano Lett., 2015. **15**: p. 6095-6101.
38. Li, G., et al., *Efficient Light-Emitting Diodes Based on Nanocrystalline Perovskite in a Dielectric Polymer Matrix.* Nano Lett. , 2015. **15**: p. 2640-2644.
39. Perumal, A., et al., *High brightness formamidinium lead bromide perovskite nanocrystal light emitting devices.* Scientific Reports, 2016. **6**: p. 36733.
40. Aygüler, M.F., et al., *Light-Emitting Electrochemical Cells Based on Hybrid Lead Halide Perovskite Nanoparticles.* J. Phys. Chem. C, 2015. **119**: p. 12047-12054.
41. Yu, J.C., et al., *Enhancing the Performance and Stability of Perovskite Nanocrystal Light-Emitting Diodes with a Polymer Matrix.* Adv. Mater. Technol., 2017. **2**: p. 1700003.
42. Zhang, X., et al., *Hybrid Perovskite Light-Emitting Diodes Based on Perovskite Nanocrystals with Organic-Inorganic Mixed Cations.* Adv. Mater., 2017. **29**: p. 1606405.
43. Zhang, X., et al., *Less-Lead Control toward Highly Efficient Formamidinium-Based Perovskite Light-Emitting Diodes.* ACS Appl. Mater. Interfaces, 2018. **10**: p. 24242-24248.
44. Kim, Y.-H., et al., *High efficiency perovskite light-emitting diodes of ligand-engineered colloidal formamidinium lead bromide nanoparticles.* Nano Energy, 2017. **38**: p. 51-58.
45. Tong, Y., et al., *Spontaneous Self-Assembly of Perovskite Nanocrystals into Electronically Coupled Supercrystals: Toward Filling the Green Gap.* Adv. Mater., 2018. **30**: p. 1801117.
46. Møller, C.K., *Crystal Structure and Photoconductivity of Caesium Plumbohalides.* Nature, 1958. **182**: p. 1436-1436.

47. Weber, D., *$CH_3NH_3PbX_3$, a Pb(II)-System with Cubic Perovskite Structure.* Zeitschrift für Naturforschung B, 1978. **33**(12): p. 1443-1445.
48. Kojima, A., et al., *Novel Photoelectrochemical Cell with Mesoscopic Electrodes Sensitized by Lead-halide Compounds (2).* 210th ECS Meeting, The Electrochemical Society, 2006.
49. *Best Research-Cell Efficiencies (Rev. 04-06-2020).* National Renewable Energy Laboratory (NREL). **https://www.nrel.gov/pv/cell-efficiency.html**.
50. Stranks, S.D., et al., *Electron-Hole Diffusion Lengths Exceeding 1 Micrometer in an Organometal Trihalide Perovskite Absorber.* Science, 2013. **342**(6156): p. 341-344.
51. Dong, Q., et al., *Electron-hole diffusion lengths > 175 um in solution-grown $CH_3NH_3PbI_3$ single crystals.* Science, 2015. **347**(6225): p. 967-970.
52. Herz, L.M., *Charge-Carrier Mobilities in Metal Halide Perovskites: Fundamental Mechanisms and Limits.* ACS Energy Lett., 2017. **2**: p. 1539-1548.
53. Xing, G., et al., *Long-Range Balanced Electronand Hole-Transport Lengths in Organic-Inorganic $CH_3NH_3PbI_3$.* Science, 2013. **342**(6156): p. 344-347.
54. Shi, D., et al., *Low trap-state density and long carrier diffusion in organolead trihalide perovskite single crystals.* Science, 2015. **347**(6221): p. 519-522.
55. Wang, Y., et al., *Nonlinear Absorption and Low-Threshold Multiphoton Pumped Stimulated Emission from All-Inorganic Perovskite Nanocrystals.* Nano Lett. , 2016. **16**: p. 448-453.
56. Walters, G., et al., *Two-Photon Absorption in Organometallic Bromide Perovskites.* ACS Nano, 2015. **9**(9): p. 9340-9346.
57. Yamada, Y., et al., *Dynamic Optical Properties of $CH_3NH_3PbI_3$ Single Crystals As Revealed by One- and Two-Photon Excited Photoluminescence Measurements.* J. Am. Chem. Soc. , 2015. **137**: p. 10456-10459.
58. Yang, D., et al., *Amplified Spontaneous Emission from Organic-Inorganic Hybrid Lead Iodide Perovskite Single Crystals under Direct Multiphoton Excitation.* Adv. Optical Mater., 2016. **4**: p. 1053-1059.
59. Schmidt, L.C., et al., *Nontemplate Synthesis of $CH_3NH_3PbBr_3$ Perovskite Nanoparticles.* J. Am. Chem. Soc., 2014. **136**: p. 850-853.
60. Gonzalez-Carrero, S., R.E. Galian, and J. P´erez-Prieto, *Maximizing the emissive properties of $CH_3NH_3PbBr_3$ perovskite nanoparticles.* J. Mater. Chem. A, 2015. **3**: p. 9187-9193.
61. Gonzalez-Carrero, S., et al., *The Luminescence of $CH_3NH_3PbBr_3$ Perovskite Nanoparticles Crests the Summit and Their Photostability under Wet Conditions is Enhanced.* small, 2016. **12**(38): p. 5245-5250.
62. Liu, F., et al., *Highly Luminescent Phase-Stable $CsPbI_3$ Perovskite Quantum Dots Achieving Near 100% Absolute Photoluminescence Quantum Yield.* ACS Nano, 2017. **11**(10): p. 10373-10383.
63. Jang, D.M., et al., *Reversible Halide Exchange Reaction of Organometal Trihalide Perovskite Colloidal Nanocrystals for Full-Range Band Gap Tuning.* Nano Lett., 2015. **15**: p. 5191-5199.
64. Sidhik, S., et al., *Enhanced Photovoltaic Performance of Mesoscopic Perovskite Solar Cells by Controlling the Interaction between $CH_3NH_3PbI_3$ Films and $CsPbX_3$ Perovskite Nanoparticles.* J. Phys. Chem. C, 2017. **121**: p. 4239-4245.
65. Cha, M., et al., *Enhancing Perovskite Solar Cell Performance by Interface Engineering Using $CH_3NH_3PbBr_{0.9}I_{2.1}$ Quantum Dots.* J. Am. Chem. Soc., 2016. **138**: p. 8581-8587.
66. Li, X., et al., *Healing All-Inorganic Perovskite Films via Recyclable Dissolution-Recyrstallization for Compact and Smooth Carrier Channels of Optoelectronic Devices with High Stability.* Adv. Funct. Mater., 2016. **26**: p. 5903-5912.

67. Wang, Q., et al., *Energy-Down-Shift $CsPbCl_3$:Mn Quantum Dots for Boosting the Efficiency and Stability of Perovskite Solar Cells.* ACS Energy Lett., 2017. **2**: p. 1479-1486.
68. Zhou, Q., et al., *In Situ Fabrication of Halide Perovskite Nanocrystal-Embedded Polymer Composite Films with Enhanced Photoluminescence for Display Backlights.* Adv. Mater. , 2016. **28**: p. 9163-9168.
69. Wang, Y., et al., *Ultrastable, Highly Luminescent Organic-Inorganic Perovskite-Polymer Composite Films.* Adv. Mater., 2016. **28**: p. 10710-10717.
70. Zhang, Y.-W., et al., *Multicolored Mixed-Organic-Cation Perovskite Quantum Dots ($FA_xMA_{1-x}PbX_3$, X = Br and I) for White Light-Emitting Diodes.* Ind. Eng. Chem. Res., 2017. **56**: p. 10053-10059.
71. Leng, M., et al., *All-Inorganic Bismuth-Based Perovskite Quantum Dots with Bright Blue Photoluminescence and Excellent Stability.* Adv. Funct. Mater., 2018. **28**: p. 1704446.
72. Muthu, C., S.R. Nagamma, and V.C. Nair, *Luminescent hybrid perovskite nanoparticles as a new platform for selective detection of 2,4,6-trinitrophenol.* RSC Adv., 2014. **4**: p. 55908-55911.
73. Doane, T.L., et al., *Using Perovskite Nanoparticles as Halide Reservoirs in Catalysis and as Spectrochemical Probes of Ions in Solution.* ACS Nano, 2016. **10**: p. 5864-5872.
74. Chen, X., et al., *$CsPbBr_3$ perovskite nanocrystals as highly selective and sensitive spectrochemical probes for gaseous HCl detection.* J. Mater. Chem. C, 2017. **5**: p. 309-313.
75. Chen, Q., et al., *All-inorganic perovskite nanocrystal scintillators.* Nature, 2018. **561**: p. 88-93.
76. Park, S., et al., *Photocatalytic hydrogen generation from hydriodic acid using methylammonium lead iodide in dynamic equilibrium with aqueous solution.* Nature Energy, 2016. **2**: p. 16185.
77. Xu, Y.-F., et al., *A $CsPbBr_3$ Perovskite Quantum Dot/Graphene Oxide Composite for Photocatalytic CO_2 Reduction.* J. Am. Chem. Soc., 2017. **139**: p. 5660-5663.
78. Hou, J., et al., *Inorganic Colloidal Perovskite Quantum Dots for Robust Solar CO_2 Reduction.* Chem. Eur. J., 2017. **23**: p. 9481-9485.
79. Zhou, L., et al., *Synthesis and Photocatalytic Application of Stable Lead-Free $Cs_2AgBiBr_6$ Perovskite Nanocrystals.* Small, 2018. **14**: p. 1703762.
80. Mu, Y.-F., et al., *Water-Tolerant Lead Halide Perovskite Nanocrystals as Efficient Photocatalysts for Visible-Light-Driven CO_2 Reduction in Pure Water.* ChemSusChem, 2019. **12**: p. 4769-4774.
81. Wu, L.-Y., et al., *Encapsulating Perovskite Quantum Dots in Iron-Based Metal-Organic Frameworks (MOFs) for Efficient Photocatalytic CO_2 Reduction.* Angew. Chem. Int. Ed., 2019. **58**: p. 9491-9495.
82. Shyamal, S., S.K. Dutta, and N. Pradhan, *Doping Iron in $CsPbBr_3$ Perovskite Nanocrystals for Efficient and Product Selective CO_2 Reduction.* J. Phys. Chem. Lett. , 2019. **10**: p. 7965-7969.
83. Pan, A., et al., *$CsPbBr_3$ Perovskite Nanocrystal Grown on MXene Nanosheets for Enhanced Photoelectric Detection and Photocatalytic CO_2 Reduction.* J. Phys. Chem. Lett. , 2019. **10**: p. 6590-6597.
84. Shao, H., et al., *Highly efficient and stable blue-emitting $CsPbBr_3$@SiO_2 nanospheres through low temperature synthesis for nanoprinting and WLED.* Nanotechnology, 2018. **29**: p. 285706.
85. Zhang, C., et al., *Conversion of invisible metal-organic frameworks to luminescent perovskite nanocrystals for confidential information encryption and decryption.* Nature Communications, 2017. **8**: p. 1138.

86. Xu, L., et al., *Double-Protected All-Inorganic Perovskite Nanocrystals by Crystalline Matrix and Silica for Triple-Modal Anti-Counterfeiting Codes.* ACS Appl. Mater. Interfaces, 2017. **9**: p. 26556-26564.
87. Zhang, H., et al., *Embedding Perovskite Nanocrystals into a Polymer Matrix for Tunable Luminescence Probes in Cell Imaging.* Adv. Funct. Mater., 2017. **27**: p. 1604382.
88. Pramanik, A., et al., *Water-Soluble and Bright Luminescent Cesium-Lead-Bromide Perovskite Quantum Dot-Polymer Composites for Tumor-Derived Exosome Imaging.* ACS Appl. Bio Mater., 2019. **2**: p. 5872-5879.
89. Lou, S., et al., *Chemical Transformation of Lead Halide Perovskite into Insoluble, Less Cytotoxic, and Brightly Luminescent $CsPbBr_3$/$CsPb_2Br_5$ Composite Nanocrystals for Cell Imaging.* ACS Appl. Mater. Interfaces, 2019. **11**: p. 24241-24246.
90. Yang, Z., et al., *Lead Halide Perovskite Nanocrystals-Phospholipid Micelles and Their Biological Applications: Multiplex Cellular Imaging and in Vitro Tumor Targeting.* ACS Appl. Mater. Interfaces, 2019. **11**: p. 47671-47679.
91. Wang, Y., et al., *Spray-Assisted Coil-Globule Transition for Scalable Preparation of Water-Resistant $CsPbBr_3$@PMMA Perovskite Nanospheres with Application in Live Cell Imaging.* Small, 2018. **14**: p. 1803156.
92. Wei, Y., et al., *Enhancing the Stability of Perovskite Quantum Dots by Encapsulation in Crosslinked Polystyrene Beads via a Swelling-Shrinking Strategy toward Superior Water Resistance.* Adv. Funct. Mater., 2017. **27**(39): p. 1703535.
93. Tan, M.J.H., et al., *Magneto-Fluorescent Perovskite Nanocomposites for Directed Cell Motion and Imaging.* Adv. Healthcare Mater., 2019. **8**(23): p. 1900859.
94. Ding, N., et al., *Highly stable and water-soluble monodisperse $CsPbX_3$/SiO_2 nanocomposites for white-LED and cells imaging.* Nanotechnology, 2018. **29**: p. 345703.
95. He, X., Y. Qiu, and S. Yang, *Fully-Inorganic Trihalide Perovskite Nanocrystals: A New Research Frontier of Optoelectronic Materials.* Adv. Mater., 2017. **29**: p. 1700775.
96. Zhang, F., et al., *Brightly Luminescent and Color-Tunable Colloidal $CH_3NH_3PbX_3$ (X = Br, I, Cl) Quantum Dots: Potential Alternatives for Display Technology.* ACS Nano, 2015. **9**(4): p. 4533-4542.
97. Hou, S., et al., *Synthesis and Stabilization of Colloidal Perovskite Nanocrystals by Multidentate Polymer Micelles.* ACS Appl. Mater. Interfaces, 2017. **9**: p. 18417-18422.
98. Hintermayr, V.A., et al., *Polymer Nanoreactors Shield Perovskite Nanocrystals from Degradation.* Nano Lett., 2019. **19**: p. 4928-4933.
99. Yoon, Y.J., et al., *Enabling Tailorable Optical Properties and Markedly Enhanced Stability of Perovskite Quantum Dots by Permanently Ligating with Polymer Hairs.* Adv. Mater., 2019: p. 1901602.
100. He, Y., et al., *Unconventional route to dual-shelled organolead halide perovskite nanocrystals with controlled dimensions, surface chemistry, and stabilities.* Sci. Adv., 2019. **5**: p. eaax4424.
101. Chen, Z., et al., *A Confined Fabrication of Perovskite Quantum Dots in Oriented MOF Thin Film.* ACS Appl. Mater. Interfaces, 2016. **8**: p. 28737-28742.
102. Ren, J., et al., *Encapsulating all-inorganic perovskite quantum dots into mesoporous metal organic frameworks with significantly enhanced stability for optoelectronic applications.* Chemical Engineering Journal, 2019. **358**: p. 30-39.
103. Li, Y., et al., *Revealing the Formation Mechanism of $CsPbBr_3$ Perovskite Nanocrystals Produced via a Slowed-Down Microwave-Assisted Synthesis.* Angew. Chem. Int. Ed., 2018. **57**: p. 5833-5837.

104. Long, Z., et al., *High-throughput and tunable synthesis of colloidal $CsPbX_3$ perovskite nanocrystals in a heterogeneous system by microwave irradiation.* Chem. Commun., 2017. **53**: p. 9914-9917.
105. Shamsi, J., et al., *Bright-Emitting Perovskite Films by Large-Scale Synthesis and Photoinduced Solid-State Transformation of $CsPbBr_3$ Nanoplatelets.* ACS Nano, 2017. **11**: p. 10206-10213.
106. Tong, Y., et al., *Highly Luminescent Cesium Lead Halide Perovskite Nanocrystals with Tunable Composition and Thickness by Ultrasonication.* Angew. Chem. Int. Ed., 2016. **55**: p. 13887-13892.
107. Kumar, V.B., et al., *Sonochemical synthesis of $CH_3NH_3PbI_3$ perovskite ultrafine nanocrystal sensitizers for solar energy applications.* Ultrasonics Sonochemistry, 2016. **32**: p. 54-59.
108. Huang, H., et al., *Top-Down Fabrication of Stable Methylammonium Lead Halide Perovskite Nanocrystals by Employing a Mixture of Ligands as Coordinating Solvents.* Angew. Chem. Int. Ed., 2017. **56**: p. 9571-9576.
109. Rao, L., et al., *Ultrasonication-assisted synthesis of $CsPbBr_3$ and Cs_4PbBr_6 perovskite nanocrystals and their reversible transformation.* Beilstein J. Nanotechnol., 2019. **10**: p. 666-676.
110. Rao, L., et al., *Polar-Solvent-Free Synthesis of Highly Photoluminescent and Stable $CsPbBr_3$ Nanocrystals with Controlled Shape and Size by Ultrasonication.* Chem. Mater., 2019. **31**: p. 365-375.
111. Tong, Y., et al., *From Precursor Powders to $CsPbX_3$ Perovskite Nanowires: One-Pot Synthesis, Growth Mechanism, and Oriented Self-Assembly.* Angew. Chem. Int. Ed., 2017. **56**: p. 13887-13892.
112. Li, C., et al., *Ultrasonic synthesis of Mn-doped $CsPbCl_3$ quantum dots (QDs) with enhanced photoluminescence.* Optical Materials, 2019. **94**: p. 41-46.
113. Tong, Y., et al., *Dilution-Induced Formation of Hybrid Perovskite Nanoplatelets.* ACS Nano, 2016. **10**: p. 10936-10944.
114. Chen, M., et al., *Solvothermal Synthesis of High-Quality All-Inorganic Cesium Lead Halide Perovskite Nanocrystals: From Nanocube to Ultrathin Nanowire.* Adv. Funct. Mater., 2017. **27**: p. 1701121.
115. Huang, H., et al., *Growth mechanism of strongly emitting $CH_3NH_3PbBr_3$ perovskite nanocrystals with a tunable bandgap.* Nature Communications, 2017. **8**: p. 996.
116. Lignos, I., et al., *Synthesis of Cesium Lead Halide Perovskite Nanocrystals in a Droplet-Based Microfluidic Platform: Fast Parametric Space Mapping.* Nano Lett., 2016. **16**: p. 1869-1877.
117. Wei, S., et al., *Room-temperature and gram-scale synthesis of $CsPbX_3$ (X = Cl, Br, I) perovskite nanocrystals with 50-85% photoluminescence quantum yields.* Chem. Commun., 2016. **52**: p. 7265-7268.
118. Hintermayr, V.A., et al., *Tuning the Optical Properties of Perovskite Nanoplatelets through Composition and Thickness by Ligand-Assisted Exfoliation.* Adv. Mater., 2016. **28**: p. 9478-9485.
119. Papavassiliou, G.C., et al., *Effects of organic moieties on the photoluminescence spectra of perovskite-type tin bromide based compounds.* Journal of Physics and Chemistry of Solids, 2015. **79**: p. 1-6.
120. Zhu, Z.-Y., et al., *Solvent-Free Mechanosynthesis of Composition-Tunable Cesium Lead Halide Perovskite Quantum Dots.* J. Phys. Chem. Lett., 2017. **8**: p. 1610-1614.
121. Protesescu, L., et al., *Low-Cost Synthesis of Highly Luminescent Colloidal Lead Halide Perovskite Nanocrystals by Wet Ball Milling.* ACS Appl. Nano Mater., 2018. **1**: p. 1300-1308.

122. Liu, Q., et al., *Gram-scale and solvent-free synthesis of Mn-doped lead halide perovskite nanocrystals.* Journal of Alloys and Compounds, 2020. **815**: p. 152393.
123. Du, K.-z., et al., *Heterovalent B-Site Co-Alloying Approach for Halide Perovskite Bandgap Engineering.* ACS Energy Lett., 2017. **2**: p. 2486-2490.
124. Pan, A., et al., *Insight into the Ligand-Mediated Synthesis of Colloidal $CsPbBr_3$ Perovskite Nanocrystals: The Role of Organic Acid, Base, and Cesium Precursors.* ACS Nano, 2016. **10**(8): p. 7943-7954.
125. Teunis, M.B., et al., *Programmable Colloidal Approach to Hierarchical Structures of Methylammonium Lead Bromide Perovskite Nanocrystals with Bright Photoluminescent Properties.* Chem. Mater., 2017. **29**: p. 3526-3537.
126. Bekenstein, Y., et al., *Highly Luminescent Colloidal Nanoplates of Perovskite Cesium Lead Halide and Their Oriented Assemblies.* J. Am. Chem. Soc., 2015. **137**(51): p. 16008-16011.
127. Li, J., et al., *2D Behaviors of Excitons in Cesium Lead Halide Perovskite Nanoplatelets.* J. Phys. Chem. Lett. , 2017. **8**: p. 1161-1168.
128. Shamsi, J., et al., *Colloidal Synthesis of Quantum Confined Single Crystal $CsPbBr_3$ Nanosheets with Lateral Size Control up to the Micrometer Range.* J. Am. Chem. Soc., 2016. **138**: p. 7240-7243.
129. Song, J., et al., *Monolayer and Few-Layer All-Inorganic Perovskites as a New Family of Two-Dimensional Semiconductors for Printable Optoelectronic Devices.* Adv. Mater., 2016. **28**: p. 4861-4869.
130. Zhang, D., et al., *Solution-Phase Synthesis of Cesium Lead Halide Perovskite Nanowires.* J. Am. Chem. Soc., 2015. **137**(29): p. 9230-9233.
131. Huang, H., et al., *Atomically thin cesium lead bromide perovskite quantum wires with high luminescence.* Nanoscale, 2017. **9**: p. 104-108.
132. He, H., B. Tang, and Y. Ma, *Controlled synthesis of quantum confined $CsPbBr_3$ perovskite nanocrystals under ambient conditions.* Nanotechnology, 2018. **29**: p. 055601.
133. Petrov, A.A., et al., *New Insight into the Formation of Hybrid Perovskite Nanowires via Structure Directing Adducts.* Chem. Mater., 2017. **29**: p. 587-594.
134. Sun, J.-K., et al., *Polar Solvent Induced Lattice Distortion of Cubic $CsPbI_3$ Nanocubes and Hierarchical Self-Assembly into Orthorhombic Single-Crystalline Nanowires.* J. Am. Chem. Soc., 2018. **140**: p. 11705-11715.
135. Li, M., et al., *Colloidal $CsPbX_3$ (X = Br, I, Cl) NCs: Morphology controlling, composition evolution, and photoluminescence shift.* Journal of Luminescence 2017. **190**: p. 397-402

136. Lu, C.-H., et al., *Control of morphology, photoluminescence, and stability of colloidal methylammonium lead bromide nanocrystals by oleylamine capping molecules.* Journal of Colloid and Interface Science, 2016. **484**: p. 17-23.
137. Huang, H., et al., *Control of Emission Color of High Quantum Yield $CH_3NH_3PbBr_3$ Perovskite Quantum Dots by Precipitation Temperature.* Adv. Sci., 2015. **2**: p. 1500194.
138. Tan, Y., et al., *Highly Luminescent and Stable Perovskite Nanocrystals with Octylphosphonic Acid as a Ligand for Efficient Light-Emitting Diodes.* ACS Appl. Mater. Interfaces, 2018. **10**: p. 3784-3792.
139. Almeida, G., et al., *Role of Acid-Base Equilibria in the Size, Shape, and Phase Control of Cesium Lead Bromide Nanocrystals.* ACS Nano, 2018. **12**: p. 1704-1711.
140. Kang, J. and L.-W. Wang, *High Defect Tolerance in Lead Halide Perovskite $CsPbBr_3$.* J. Phys. Chem. Lett. , 2017. **8**: p. 489-493.

141. Brandt, R.E., et al., *Identifying defect-tolerant semiconductors with high minority-carrier lifetimes: beyond hybrid lead halide perovskites.* MRS Communications, 2015. **5**: p. 265-275.

142. Swarnkar, A., V.K. Ravi, and A. Nag, *Beyond Colloidal Cesium Lead Halide Perovskite Nanocrystals: Analogous Metal Halides and Doping.* ACS Energy Lett. , 2017. **2**: p. 1089-1098.

143. Dirin, D.N., et al., *Harnessing Defect-Tolerance at the Nanoscale: Highly Luminescent Lead Halide Perovskite Nanocrystals in Mesoporous Silica Matrixes.* Nano Lett., 2016. **16**: p. 5866-5874.

144. Buin, A., et al., *Materials Processing Routes to Trap-Free Halide Perovskites.* Nano Lett., 2014. **14**: p. 6281-6286.

145. Brinck, S.t. and I. Infante, *Surface Termination, Morphology, and Bright Photoluminescence of Cesium Lead Halide Perovskite Nanocrystals.* ACS Energy Lett., 2016. **1**(6): p. 1266-1272.

146. Ono, L.K., E.J. Juarez-Perez, and Y. Qi, *Progress on Perovskite Materials and Solar Cells with Mixed Cations and Halide Anions.* ACS Appl. Mater. Interfaces, 2017. **9**: p. 30197-30246.

147. Goldschmidt, V.M., *Die Gesetze der Krystallochemie.* Naturwissenschaften, 1926. **14**(21): p. 477-485.

148. Stoumpos, C.C. and M.G. Kanatzidis, *The Renaissance of Halide Perovskites and Their Evolution as Emerging Semiconductors.* Acc. Chem. Res., 2015. **48**: p. 2791-2802.

149. Green, M.A., A. Ho-Baillie, and H.J. Snaith, *The emergence of perovskite solar cells.* Nature Photonics, 2014. **8**: p. 506-514.

150. Akkerman, Q.A., et al., *Genesis, challenges and opportunities for colloidal lead halide perovskite nanocrystals.* Nature Materials, 2018: p. doi:10.1038/s41563-018-0018-4.

151. Saparov, B. and D.B. Mitzi, *Organic-Inorganic Perovskites: Structural Versatility for Functional Materials Design.* Chem. Rev., 2016. **116**: p. 4558-4596.

152. Mitzi, D.B., *Templating and structural engineering in organic-inorganic perovskites.* J. Chem. Soc., Dalton Trans., 2001. **0**: p. 1-12.

153. Huang, H., et al., *Lead Halide Perovskite Nanocrystals in the Research Spotlight: Stability and Defect Tolerance.* ACS Energy Lett. , 2017. **2**: p. 2071-2083.

154. Li, C., et al., *Formability of ABX_3 (X = F, Cl, Br, I) halide perovskites.* Acta Cryst. , 2008. **B64**: p. 702-707.

155. Zhang, T., et al., *Bication lead iodide 2D perovskite component to stabilize inorganic α-$CsPbI_3$ perovskite phase for high-efficiency solar cells.* Sci. Adv., 2017. **3**(9): p. e1700841.

156. Saliba, M., et al., *Incorporation of rubidium cations into perovskite solar cells improves photovoltaic performance.* Science, 2016. **354**(6309): p. 206-209.

157. Hoefler, S.F., G. Trimmel, and T. Rath, *Progress on lead-free metal halide perovskites for photovoltaic applications: a review.* Monatsh Chem, 2017. **148**(5): p. 795-826.

158. Walsh, A., *Principles of Chemical Bonding and Band Gap Engineering in Hybrid Organic-Inorganic Halide Perovskites.* J. Phys. Chem. C, 2015. **119**: p. 5755-5760.

159. Kieslich, G., S. Sun, and A.K. Cheetham, *An extended Tolerance Factor approach for organic-inorganic perovskites.* Chem. Sci., 2015. **6**: p. 3430-3433.

160. Travis, W., et al., *On the application of the tolerance factor to inorganic and hybrid halide perovskites: a revised system.* Chem. Sci., 2016. **7**: p. 4548-4556.

161. Sani, F., et al., *Advancement on Lead-Free Organic-Inorganic Halide Perovskite Solar Cells: A Review.* Materials, 2018. **11**(6): p. 1008.

162. Lou, Y., et al., *Rod-shaped thiocyanate-induced abnormal band gap broadening in SCN-doped $CsPbBr_3$ perovskite nanocrystals.* Nano Research, 2018. **11**(5): p. 2715-2723.
163. Wu, Y., et al., *The Impact of Hybrid Compositional Film/Structure on Organic-Inorganic Perovskite Solar Cells.* Nanomaterials, 2018. **8**(6): p. 356.
164. Toshniwal, A. and V. Kheraj, *Development of organic-inorganic tin halide perovskites: A review.* Solar Energy, 2017. **149**: p. 54-59.
165. Ning, C.-Z., L. Dou, and P. Yang, *Bandgap engineering in semiconductor alloy nanomaterials with widely tunable compositions.* Nature Reviews Materials, 2017. **2**: p. 17070.
166. Eperon, G.E., et al., *Formamidinium lead trihalide: a broadly tunable perovskite for efficient planar heterojunction solar cells.* Energy Environ. Sci., 2014. **7**: p. 982-988.
167. Salado, M., et al., *Influence of the mixed organic cation ratio in lead iodide based perovskite on the performance of solar cells* Phys. Chem. Chem. Phys., 2016. **18**: p. 27148-27157.
168. Pellet, N., et al., *Mixed-Organic-Cation Perovskite Photovoltaics for Enhanced Solar-Light Harvesting.* Angew. Chem. Int. Ed., 2014. **53**: p. 3151-3157.
169. Xu, F., et al., *Mixed cation hybrid lead halide perovskites with enhanced performance and stability.* J. Mater. Chem. A, 2017. **5**: p. 11450-11461.
170. Dong, Y., et al., *Recent advances toward practical use of halide perovskite nanocrystals.* J. Mater. Chem. A, 2018. **6**: p. 21729-21746.
171. Shamsi, J., et al., *Metal Halide Perovskite Nanocrystals: Synthesis, Post-Synthesis Modifications, and Their Optical Properties.* Chem. Rev., 2019. **119**: p. 3296-3348.
172. Zhang, X., et al., *Rational chemical doping of metal halide perovskites.* Chem. Soc. Rev., 2019. **48**: p. 517-539.
173. Kumawat, N.K., et al., *Metal Doping/Alloying of Cesium Lead Halide Perovskite Nanocrystals and their Applications in Light-Emitting Diodes with Enhanced Efficiency and Stability.* Isr. J. Chem. , 2019. **59**: p. 695-707.
174. Xu, L., et al., *A comprehensive review of doping in perovskite nanocrystals/quantum dots: evolution of structure, electronics, optics, and lightemitting diodes.* Materials Today Nano, 2019. **6**: p. 100036.
175. Li, M.-Q., et al., *Structure Tunable Organic-Inorganic Bismuth Halides for an Enhanced Two-Dimensional Lead-Free Light-Harvesting Material.* Chem. Mater., 2017. **29**: p. 5463-5467.
176. Cortecchia, D., et al., *Lead-Free $MA_2CuCl_xBr_{4-x}$ Hybrid Perovskites.* Inorg. Chem., 2016. **55**: p. 1044-1052.
177. Nasilowski, M., et al., *Two-Dimensional Colloidal Nanocrystals.* Chem. Rev., 2016. **116**: p. 10934-10982.
178. Weidman, M.C., et al., *Highly Tunable Colloidal Perovskite Nanoplatelets through Variable Cation, Metal, and Halide Composition.* ACS Nano, 2016. **10**: p. 7830-7839.
179. Weidman, M.C., A.J. Goodman, and W.A. Tisdale, *Colloidal Halide Perovskite Nanoplatelets: An Exciting New Class of Semiconductor Nanomaterials.* Chem. Mater., 2017. **29**: p. 5019-5030.
180. Adhikari, S.D., et al., *Layered Perovskites $L_2(Pb_{1-x}Mn_x)Cl_4$ to Mn-Doped $CsPbCl_3$ Perovskite Platelets.* ACS Energy Lett., 2018. **3**: p. 1247-1253.
181. Hassan, Y., et al., *Structure-Tuned Lead Halide Perovskite Nanocrystals.* Adv. Mater., 2016. **28**: p. 566-573.
182. Saidaminov, M.I., O.F. Mohammed, and O.M. Bakr, *Low-Dimensional-Networked Metal Halide Perovskites: The Next Big Thing.* ACS Energy Lett., 2017. **2**: p. 889-896.

183. Liu, Z., et al., *Ligand Mediated Transformation of Cesium Lead Bromide Perovskite Nanocrystals to Lead Depleted Cs_4PbBr_6 Nanocrystals.* J. Am. Chem. Soc., 2017,. **139**: p. 5309-5312.

184. Stoumpos, C.C., et al., *Ruddlesden-Popper Hybrid Lead Iodide Perovskite 2D Homologous Semiconductors.* Chem. Mater., 2016. **28**: p. 2852-2867.

185. Amat, A., et al., *Cation-Induced Band-Gap Tuning in Organohalide Perovskites: Interplay of Spin-Orbit Coupling and Octahedra Tilting.* Nano Lett., 2014. **14**: p. 3608-3616.

186. El-Mellouhi, F., et al., *Enhancing Intrinsic Stability of Hybrid Perovskite Solar Cell by Strong, yet Balanced, Electronic Coupling.* Scientific Reports, 2016. **6**: p. 30305.

187. Protesescu, L., et al., *Monodisperse Formamidinium Lead Bromide Nanocrystals with Bright and Stable Green Photoluminescence.* J. Am. Chem. Soc., 2016. **138**(43): p. 14202-14205.

188. Lignos, I., et al., *Unveiling the Shape Evolution and Halide-Ion-Segregation in Blue-Emitting Formamidinium Lead Halide Perovskite Nanocrystals Using an Automated Microfluidic Platform.* Nano Lett., 2018. **18**: p. 1246-1252.

189. Imran, M., et al., *Benzoyl Halides as Alternative Precursors for the Colloidal Synthesis of Lead-Based Halide Perovskite Nanocrystals.* J. Am. Chem. Soc., 2018. **140**: p. 2656-2664.

190. Levchuk, I., et al., *Brightly Luminescent and Color-Tunable Formamidinium Lead Halide Perovskite $FAPbX_3$ (X = Cl, Br, I) Colloidal Nanocrystals.* Nano Lett., 2017. **17**: p. 2765-2770.

191. Minh, D.N., et al., *Room-Temperature Synthesis of Widely Tunable Formamidinium Lead Halide Perovskite Nanocrystals.* Chem. Mater. , 2017. **29**: p. 5713-5719.

192. Hoke, E.T., et al., *Reversible photo-induced trap formation in mixedhalide hybrid perovskites for photovoltaics.* Chem. Sci., 2015. **6**: p. 613-617.

193. Vashishtha, P. and J.E. Halpert, *Field-Driven Ion Migration and Color Instability in Red-Emitting Mixed Halide Perovskite Nanocrystal Light-Emitting Diodes.* Chem. Mater., 2017. **29**: p. 5965-5973.

194. Zhang, H., et al., *Phase segregation due to ion migration in all-inorganic mixed-halide perovskite nanocrystals.* Nature Communications, 2019. **10**: p. 1088.

195. Unger, E.L., et al., *Hysteresis and transient behavior in current-voltage measurements of hybrid-perovskite absorber solar cells.* Energy Environ. Sci., 2014. **7**: p. 3690-3698.

196. Eames, C., et al., *Ionic transport in hybrid lead iodide perovskite solar cells.* Nature Communications, 2015. **6**: p. 7497.

197. Yarita, N., et al., *Impact of Postsynthetic Surface Modification on Photoluminescence Intermittency in Formamidinium Lead Bromide Perovskite Nanocrystals.* J. Phys. Chem. Lett., 2017. **8**: p. 6041-6047.

198. Hills-Kimball, K., et al., *Synthesis of formamidinium lead halide perovskite nanocrystals through solid-liquid-solid cation exchange.* J. Mater. Chem. C, 2017. **5**: p. 5680-5684.

199. Motta, C., F. El-Mellouhi, and S. Sanvito, *Exploring the cation dynamics in lead-bromide hybrid perovskites.* Physical Review B, 2016. **93**: p. 235412.

200. Zhou, Y., et al., *Exceptional Morphology-Preserving Evolution of Formamidinium Lead Triiodide Perovskite Thin Films via Organic-Cation Displacement.* J. Am. Chem. Soc., 2016. **138**: p. 5535-5538.

201. Zheng, X., et al., *Improved Phase Stability of Formamidinium Lead Triiodide Perovskite by Strain Relaxation.* ACS Energy Lett., 2016. **1**: p. 1014-1020.

202. Protesescu, L., et al., *Dismantling the "Red Wall" of Colloidal Perovskites: Highly Luminescent Formamidinium and Formamidinium-Cesium Lead Iodide Nanocrystals.* ACS Nano, 2017. **11**(3): p. 3119-3134.

203. McMeekin, D.P., et al., *A mixed-cation lead mixed-halide perovskite absorber for tandem solar cells.* Science, 2016. **351**(6269): p. 151-155.
204. Wang, C., et al., *Controlled Synthesis of Composition Tunable Formamidinium Cesium Double Cation Lead Halide Perovskite Nanowires and Nanosheets with Improved Stability.* Chem. Mater., 2017. **29**: p. 2157-2166.
205. Lignos, I., et al., *Exploration of Near-Infrared-Emissive Colloidal Multinary Lead Halide Perovskite Nanocrystals Using an Automated Microfluidic Platform.* ACS Nano, 2018. **12**: p. 5504-5517.
206. Xu, B., et al., *Bright and efficient light-emitting diodes based on MA/Cs double cation perovskite nanocrystals.* J. Mater. Chem. C, 2017. **5**: p. 6123-6128.
207. Gallardo, J.J., et al., *Tuning the structural, optical and photoluminescence properties of hybrid perovskite quantum dots by A-site doping.* Applied Materials Today, 2020. **18**: p. 100488.
208. Zhang, R., et al., *Ni and K ion doped $CsPbX_3$ NCs for the improvement of luminescence properties by a facile synthesis method in ambient air.* Journal of Luminescence, 2020. **221**: p. 117044.
209. Linaburg, M.R., et al., *$Cs_{1-x}Rb_xPbCl_3$ and $Cs_{1-x}Rb_xPbBr_3$ Solid Solutions: Understanding Octahedral Tilting in Lead Halide Perovskites.* Chem. Mater., 2017. **29**: p. 3507-3514.
210. Amgar, D., et al., *Near ultra-violet to mid-visible band gap tuning of mixed cation $Rb_xCs_{1-x}PbX_3$ (X = Cl or Br) perovskite nanoparticles.* Nanoscale, 2018. **10**: p. 6060-6068.
211. Todorovic´, P., et al., *Spectrally Tunable and Stable Electroluminescence Enabled by Rubidium Doping of $CsPbBr_3$ Nanocrystals.* Adv. Optical Mater., 2019: p. 1901440.
212. Vashishtha, P., et al., *Shape-, Size-, and Composition-Controlled Thallium Lead Halide Perovskite Nanowires and Nanocrystals with Tunable Band Gaps.* Chem. Mater., 2018. **30**: p. 2973-2982.
213. Mir, W.J., et al., *Colloidal thallium halide nanocrystals with reasonable luminescence, carrier mobility and diffusion length.* Chem. Sci., 2017. **8**: p. 4602-4611.
214. Swarnkar, A., W.J. Mir, and A. Nag, *Can B-Site Doping or Alloying Improve Thermal- and Phase-Stability of All-Inorganic $CsPbX_3$ (X = Cl, Br, I) Perovskites?* ACS Energy Lett., 2018. **3**(2): p. 286-289.
215. *Restriction of the use of certain hazardous substances (RoHS).* Directive 2011/65/EU.
216. Ogomi, Y., et al., *$CH_3NH_3Sn_xPb_{(1-x)}I_3$ Perovskite Solar Cells Covering up to 1060 nm.* J. Phys. Chem. Lett., 2014. **5**: p. 1004-1011.
217. Hao, F., et al., *Anomalous Band Gap Behavior in Mixed Sn and Pb Perovskites Enables Broadening of Absorption Spectrum in Solar Cells.* J. Am. Chem. Soc., 2014. **136**: p. 8094-8099.
218. Hao, F., et al., *Lead-free solid-state organic-inorganic halide perovskite solar cells.* Nature Photonics, 2014. **8**: p. 489-494.
219. Liu, C., et al., *Highly Efficient Perovskite Solar Cells with Substantial Reduction of Lead Content.* Scientific Reports, 2016. **6**: p. 35705.
220. Stoumpos, C.C., et al., *Hybrid Germanium Iodide Perovskite Semiconductors: Active Lone Pairs, Structural Distortions, Direct and Indirect Energy Gaps, and Strong Nonlinear Optical Properties.* J. Am. Chem. Soc. , 2015. **137**: p. 6804-6819.
221. Maughan, A.E., et al., *Defect Tolerance to Intolerance in the Vacancy-Ordered Double Perovskite Semiconductors Cs_2SnI_6 and Cs_2TeI_6.* J. Am. Chem. Soc. , 2016. **138**: p. 8453-8464.
222. Klug, M.T., et al., *Tailoring metal halide perovskites through metal substitution: influence on photovoltaic and material properties.* Energy Environ. Sci., 2017. **10**: p. 236-246.

223. Zhang, X., et al., *Efficient light-emitting diodes based on green perovskite nanocrystals with mixed-metal cations.* Nano Energy, 2016. **30**: p. 511-516.

224. Vegard, L., *Die Konstitution der Mischkristalle und die Raumfüllung der Atome.* Zeitschrift für Physik 1921. **5**(1): p. 17-26.

225. Vitoreti, A.B.F., et al., *Study of the Partial Substitution of Pb by Sn in Cs-Pb-Sn-Br Nanocrystals Owing to Obtaining Stable Nanoparticles with Excellent Optical Properties.* J. Phys. Chem. C, 2018. **122**: p. 14222-14231.

226. Deng, J., et al., *Room-temperature synthesis of excellent-performance* $CsPb_{1-x}Sn_xBr_3$ *perovskite quantum dots and application in light emitting diodes.* Materials & Design, 2020. **185**: p. 108246.

227. Stam, W.v.d., et al., *Highly Emissive Divalent-Ion-Doped Colloidal* $CsPb_{1-x}M_xBr_3$ *Perovskite Nanocrystals through Cation Exchange.* J. Am. Chem. Soc., 2017. **139**: p. 4087-4097.

228. Li, M., et al., *An anion-driven* Sn^{2+} *exchange reaction in* $CsPbBr_3$ *nanocrystals towards tunable and high photoluminescence.* J. Mater. Chem. C, 2018. **6**: p. 5506-5513.

229. Huang, G., et al., *Postsynthetic Doping of* $MnCl_2$ *Molecules into Preformed* $CsPbBr_3$ *Perovskite Nanocrystals via a Halide Exchange-Driven Cation Exchange.* Adv. Mater. , 2017. **29**: p. 1700095.

230. Wang, H.-C., et al., *High-Performance* $CsPb_{1-x}Sn_xBr_3$ *Perovskite Quantum Dots for Light-Emitting Diodes.* Angew. Chem. Int. Ed., 2017. **56**: p. 13650-13654.

231. Li, N., et al., *Inorganic* $CsPb_{1-x}Sn_xIBr_2$ *for Efficient Wide-Bandgap Perovskite Solar Cells.* Adv. Energy Mater., 2018. **8**: p. 1800525

232. Eperon, G.E. and D.S. Ginger, *B-Site Metal Cation Exchange in Halide Perovskites.* ACS Energy Lett. , 2017. **2**: p. 1190-1196.

233. Liu, S., et al., *Doping and surface passivation improve luminescence intensity and stability of* $CsPbI_3$ *nanocrystals for LEDs.* Materials Letters, 2020. **259**: p. 126857.

234. Jellicoe, T.C., et al., *Synthesis and Optical Properties of Lead-Free Cesium Tin Halide Perovskite Nanocrystals.* J. Am. Chem. Soc., 2016. **138**(9): p. 2941-2944.

235. Chen, L.-J., et al., *Synthesis and Optical Properties of Lead-Free Cesium Tin Halide Perovskite Quantum Rods with High-Performance Solar Cell Application.* J. Phys. Chem. Lett. , 2016. **7**: p. 5028-5035.

236. Wang, A., et al., *Controlled Synthesis of Lead-Free Cesium Tin Halide Perovskite Cubic Nanocages with High Stability.* Chem. Mater., 2017. **29**: p. 6493-6501.

237. Wang, A., et al., *Controlled Synthesis of Lead-Free and Stable Perovskite Derivative* Cs_2SnI_6 *Nanocrystals via a Facile Hot-Injection Process.* Chem. Mater., 2016. **28**: p. 8132-8140.

238. Dolzhnikov, D.S., et al., *Ligand-Free, Quantum-Confined* Cs_2SnI_6 *Perovskite Nanocrystals.* Chem. Mater., 2017. **29**: p. 7901-7907.

239. Zhang, X., et al., *Bright Orange Electroluminescence from Lead-Free Two-Dimensional Perovskites.* ACS Energy Lett. , 2019. **4**: p. 242-248.

240. Kontos, A.G., et al., *Structural Stability, Vibrational Properties, and Photoluminescence in* $CsSnI_3$ *Perovskite upon the Addition of* SnF_2*.* Inorg. Chem., 2017. **56**: p. 84-91.

241. Liu, F., et al., *Near-Infrared Emission from Tin-Lead (Sn-Pb) Alloyed Perovskite Quantum Dots by Sodium Doping.* Angew Chem Int Ed, 2020.

242. Chung, I., et al., *All-solid-state dye-sensitized solar cells with high efficiency.* Nature, 2012. **485**: p. 486-489.

243. Peedikakkandy, L. and P. Bhargava, *Recrystallization and phase stability study of cesium tin iodide for application as a hole transporter in dyesensitized solar cells.* Materials Science in Semiconductor Processing, 2015. **33**: p. 103-109.
244. Kumar, M.H., et al., *Lead-Free Halide Perovskite Solar Cells with High Photocurrents Realized Through Vacancy Modulation.* Adv. Mater., 2014. **26**: p. 7122-7127.
245. Koh, T.M., et al., *Formamidinium tin-based perovskite with low Eg for photovoltaic applications.* J. Mater. Chem. A, 2015. **3**: p. 14996-15000.
246. Lee, S.J., et al., *Fabrication of Efficient Formamidinium Tin Iodide Perovskite Solar Cells through SnF_2-Pyrazine Complex.* J. Am. Chem. Soc., 2016. **138**: p. 3974-3977.
247. Xing, G., et al., *Solution-Processed Tin-Based Perovskite for Near-Infrared Lasing.* Adv. Mater., 2016. **28**: p. 8191-8196.
248. Dimesso, L., et al., *Investigation of cesium tin/lead iodide ($CsSn_{1-x}Pb_xI_3$) systems.* Materials Research Bulletin, 2017. **85**: p. 80-89.
249. Babayigit, A., et al., *Assessing the toxicity of Pb- and Sn-based perovskite solar cells in model organism Danio rerio.* Scientific Reports, 2016. **6**: p. 18721.
250. Guria, A.K., et al., *Doping Mn^{2+} in Lead Halide Perovskite Nanocrystals: Successes and Challenges.* ACS Energy Lett., 2017. **2**: p. 1014-1021.
251. Chen, D., G. Fang, and X. Chen, *Silica-Coated Mn-Doped $CsPb(Cl/Br)_3$ Inorganic Perovskite Quantum Dots: Exciton-to-Mn Energy Transfer and Blue-Excitable Solid-State Lighting.* ACS Appl. Mater. Interfaces, 2017. **9**: p. 40477-40487.
252. Wu, W., et al., *Temperature-dependent photoluminescence of pure and Mn-doped $CsPbCl_3$ nanocrystals.* Journal of Alloys and Compounds, 2019. **787**: p. 165-172.
253. Li, F., et al., *Optical properties of Mn^{2+} doped cesium lead halide perovskite nanocrystals via a cation-anion co-substitution exchange reaction.* J. Mater. Chem. C, 2017. **5**: p. 9281-9287.
254. Gao, D., et al., *Postsynthetic, Reversible Cation Exchange between Pb^{2+} and Mn^{2+} in Cesium Lead Chloride Perovskite Nanocrystals.* J. Phys. Chem. C, 2017. **121**(37): p. 20387-20395.
255. Qiao, T., et al., *Photoinduced Mn doping in cesium lead halide perovskite nanocrystals.* Nanoscale, 2019. **11**: p. 5247-5253.
256. Hills-Kimball, K., et al., *Ligand Engineering for Mn^{2+} Doping Control in CsPbCl3 Perovskite Nanocrystals via a Quasi-Solid-Solid Cation Exchange Reaction.* 32, 2020. **Chem. Mater.**(6): p. 2489-2500.
257. Liu, H., et al., *$CsPb_xMn_{1-x}Cl_3$ Perovskite Quantum Dots with High Mn Substitution Ratio.* ACS Nano, 2017. **11**: p. 2239-2247.
258. Liu, W., et al., *Mn^{2+}-Doped Lead Halide Perovskite Nanocrystals with Dual-Color Emission Controlled by Halide Content.* J. Am. Chem. Soc., 2016. **138**: p. 14954-14961.
259. Xu, K. and A. Meijerink, *Tuning Exciton-Mn^{2+} Energy Transfer in Mixed Halide Perovskite Nanocrystals.* Chem. Mater., 2018. **30**: p. 5346-5352.
260. Parobek, D., et al., *Exciton-to-Dopant Energy Transfer in Mn-Doped Cesium Lead Halide Perovskite Nanocrystals.* Nano Lett., 2016. **16**: p. 7376-7380.
261. Zhu, J., et al., *Room-Temperature Synthesis of Mn-Doped Cesium Lead Halide Quantum Dots with High Mn Substitution Ratio.* J. Phys. Chem. Lett. , 2017. **8**: p. 4167-4171.
262. Parobek, D., et al., *Direct Hot-Injection Synthesis of Mn-Doped $CsPbBr_3$ Nanocrystals.* Chem. Mater. , 2018. **30**: p. 2939-2944.
263. Xu, K., et al., *Efficient and Stable Luminescence from Mn^{2+} in Core and Core-Isocrystalline Shell $CsPbCl_3$ Perovskite Nanocrystals.* Chem. Mater., 2017. **29**: p. 4265-4272.
264. Adhikari, S.D., et al., *Chemically tailoring the dopant emission in Manganese-doped $CsPbCl_3$ perovskite nanocrystals.* Angew. Chem. Int. Ed., 2017. **56**: p. 8746-8750.

265. Lin, C.C., et al., *Luminescent manganese-doped $CsPbCl_3$ perovskite quantum dots.* Scientific Reports, 2017. **7**: p. 45906.

266. Akkerman, Q.A., et al., *Fluorescent Alloy $CsPb_xMn_{1-x}I_3$ Perovskite Nanocrystals with High Structural and Optical Stability.* ACS Energy Lett., 2017. **2**: p. 2183-2186.

267. Wang, S., et al., *Ultrafast Dopant-Induced Exciton Auger-Like Recombination in Mn-Doped Perovskite Nanocrystals.* ACS Energy Lett., 2020. **5**: p. 328-334.

268. Rossi, D., et al., *Dynamics of Exciton-Mn Energy Transfer in Mn-Doped $CsPbCl_3$ Perovskite Nanocrystals.* J. Phys. Chem. C, 2017. **121**: p. 17143-17149.

269. Mir, W.J., et al., *Colloidal Mn-Doped Cesium Lead Halide Perovskite Nanoplatelets.* ACS Energy Lett. , 2017. **2**: p. 537-543.

270. Sun, Q., et al., *Excitation-Dependent Emission Color Tuning from an Individual Mn-Doped Perovskite Microcrystal.* J. Am. Chem. Soc., 2019. **141**(51): p. 20089-20096.

271. Akkerman, Q.A., et al., *Solution Synthesis Approach to Colloidal Cesium Lead Halide Perovskite Nanoplatelets with Monolayer-Level Thickness Control.* J. Am. Chem. Soc., 2016. **138**(3): p. 1010-1016.

272. Xu, K., et al., *First Synthesis of Mn-Doped Cesium Lead Bromide Perovskite Magic Sized Clusters at Room Temperature.* J. Phys. Chem. Lett. , 2020. **11**(3): p. 1162-1169.

273. Nag, A., S. Chakraborty, and D.D. Sarma, *To Dope Mn^{2+} in a Semiconducting Nanocrystal.* J. Am. Chem. Soc., 2008. **130**(32): p. 10605-10611.

274. Norris, D.J., A.L. Efros, and S.C. Erwin, *Doped Nanocrystals.* Science, 2008. **319**(5871): p. 1776-1779.

275. Dalpian, G.M. and J.R. Chelikowsky, *Self-Purification in Semiconductor Nanocrystals.* Phys. Rev. Lett., 2006. **96**: p. 226802.

276. Du, M.-H., et al., *Comment on "Self-Purification in Semiconductor Nanocrystals".* Phys. Rev. Lett., 2008. **100**: p. 179702.

277. Bai, D., et al., *Interstitial Mn^{2+}-Driven High-Aspect-Ratio Grain Growth for Low-Trap-Density Microcrystalline Films for Record Efficiency $CsPbI_2Br$ Solar Cells.* ACS Energy Lett., 2018. **3**: p. 970-978.

278. Pan, Y., et al., *A facile synthesis of Mn doped $CsPbCl_3$ perovskite with high photoluminescence properties.* Optik, 2019. **198**: p. 163241.

279. Liu, W., et al., *Mass production of Mn^{2+}-doped $CsPbCl_3$ perovskite nanocrystals with high quality and enhanced optical performance.* Inorg. Chem. Front., 2018. **5**: p. 2641-2647.

280. Yao, W., et al., *Room-temperature synthesis of Mn^{2+}-doped cesium lead halide perovskite nanocrystals via a transformation doping method.* Journal of Materials Science: Materials in Electronics, 2019. **30**: p. 180-188.

281. Chen, N., et al., *Yb- and Mn-Doped Lead-Free Double Perovskite Cs_2AgBiX_6 (X = Cl^-, Br^-) Nanocrystals.* ACS Appl. Mater. Interfaces, 2019. **11**: p. 16855-16863.

282. Locardi, F., et al., *Colloidal Synthesis of Double Perovskite $Cs_2AgInCl_6$ and Mn-Doped $Cs_2AgInCl_6$ Nanocrystals.* J. Am. Chem. Soc. , 2018. **140**: p. 12989-12995.

283. Xing, K., et al., *Improved Doping and Emission Efficiencies of Mn-Doped $CsPbCl_3$ Perovskite Nanocrystals via Nickel Chloride.* J. Phys. Chem. Lett. , 2019. **10**: p. 4177-4184.

284. Arunkumar, P., et al., *Colloidal Organolead Halide Perovskite with a High Mn Solubility Limit: A Step Toward Pb-Free Luminescent Quantum Dots.* J. Phys. Chem. Lett. , 2017. **8**: p. 4161-4166.

285. Li, X., Y. Guo, and B. Luo, *Improved Stability and Photoluminescence Yield of Mn^{2+}-Doped $CH_3NH_3PbCl_3$ Perovskite Nanocrystals.* Crystals, 2018. **8**(1): p. 4.

286. Pan, A., et al., *Stable Luminous Nanocomposites of Confined Mn^{2+}-Doped Lead Halide Perovskite Nanocrystals in Mesoporous Silica Nanospheres as Orange Fluorophores.* Inorg. Chem., 2019. **58**: p. 3950-3958.
287. Cortecchia, D., et al., *Defect Engineering in 2D Perovskite by Mn(II) Doping for Light-Emitting Applications.* Chem, 2019. **5**: p. 2146-2158.
288. Adhikari, S.D., et al., *Presence of Metal Chloride for Minimizing the Halide Deficiency and Maximizing the Doping Efficiency in Mn(II)-Doped $CsPbCl_3$ Nanocrystals.* J. Phys. Chem. Lett., 2019. **10**: p. 1530-1536.
289. Gangishetty, M.K., S.N. Sanders, and D.N. Congreve, *Mn^{2+} Doping Enhances the Brightness, Efficiency, and Stability of Bulk Perovskite Light-Emitting Diodes.* ACS Photonics, 2019. **6**: p. 1111-1117.
290. Zhou, S., et al., *Chlorine-additive-promoted incorporation of Mn^{2+} dopants into $CsPbCl_3$ perovskite nanocrystals.* Nanoscale, 2019. **11**: p. 12465-12470.
291. Zhang, J., et al., *Tunable photoluminescence and an enhanced photoelectric response of Mn^{2+}-doped $CsPbCl_3$ perovskite nanocrystals via pressure-induced structure evolution.* Nanoscale, 2019. **11**: p. 11660-11670.
292. Liu, W., et al., *Electron-beam irradiation-hard metal-halide perovskite nanocrystals.* J. Mater. Chem., 2019. **7**: p. 10912-10917.
293. Bai, K., et al., *Room temperature synthesis of Mn-doped $Cs_3Pb_{6.48}Cl_{16}$ perovskite nanocrystals with pure dopant emission and temperature-dependent photoluminescence.* CrystEngComm, 2019. **21**: p. 3568-3575.
294. Adhikari, S.D., A.K. Guria, and N. Pradhan, *Insights of Doping and the Photoluminescence Properties of Mn-Doped Perovskite Nanocrystals.* J. Phys. Chem. Lett., 2019. **10**: p. 2250-2257.
295. Veith, M., et al., *Low temperature synthesis of nanocrystalline $Y_3Al_5O_{12}$ (YAG) and Ce-doped $Y_3Al_5O_{12}$ via different sol-gel methods.* J. Mater. Chem., 1999. **9**: p. 3069-3079.
296. Lu, C.-H., H.-C. Hong, and R. Jagannathan, *Sol-gel synthesis and photoluminescent properties of cerium-ion doped yttrium aluminium garnet powders.* J. Mater. Chem., 2002. **12**: p. 2525-2530.
297. Wang, J., et al., *Single-Band Upconversion Emission in Lanthanide-Doped $KMnF_3$ Nanocrystals.* Angew. Chem. Int. Ed. , 2011. **50**: p. 10369-10372.
298. Shi, S., et al., *Scalable Direct Writing of Lanthanide-Doped $KMnF_3$ Perovskite Nanowires into Aligned Arrays with Polarized Up-Conversion Emission.* Nano Lett., 2018. **18**: p. 2964-2969.
299. Boyer, J.-C., L.A. Cuccia, and J.A. Capobianco, *Synthesis of Colloidal Upconverting $NaYF_4$: Er^{3+}/Yb^{3+} and Tm^{3+}/Yb^{3+} Monodisperse Nanocrystals.* Nano Lett., 2007. **7**(3): p. 847-852.
300. Zhao, J., et al., *Controlled Synthesis, Formation Mechanism, and Great Enhancement of Red Upconversion Luminescence of $NaYF_4:Yb^{3+}$, Er^{3+} Nanocrystals/Submicroplates at Low Doping Level.* J. Phys. Chem. B, 2008. **112**: p. 15666-15672.
301. Homann, C., et al., *$NaYF_4$:Yb,Er/$NaYF_4$ Core/Shell Nanocrystals with High Upconversion Luminescence Quantum Yield.* Angew. Chem. Int. Ed. , 2018. **57**: p. 8765-8769.
302. Yao, J.-S., et al., *Ce^{3+}-Doping to Modulate Photoluminescence Kinetics for Efficient $CsPbBr_3$ Nanocrystals Based Light-Emitting Diodes.* J. Am. Chem. Soc., 2018. **140**: p. 3626-3634.
303. Brown, E.E., et al., *Optical properties of Pr^{3+}-, Ce^{3+}-, and Eu^{2+}-doped ternary lead halides.* Proc. SPIE, 2015. **9359**: p. 93591U.
304. Zhou, D., et al., *Cerium and Ytterbium Codoped Halide Perovskite Quantum Dots: A Novel and Efficient Downconverter for Improving the Performance of Silicon Solar Cells.* Adv. Mater., 2017. **29**: p. 1704149.

305. Wegh, R.T., et al., *Visible Quantum Cutting in $LiGdF_4$:Eu^{3+} Through Downconversion.* Science, 1999. **283**(5402): p. 663-666.
306. Milstein, T.J., D.M. Kroupa, and D.R. Gamelin, *Picosecond Quantum Cutting Generates Photoluminescence Quantum Yields Over 100% in Ytterbium-Doped $CsPbCl_3$ Nanocrystals.* Nano Lett., 2018. **18**: p. 3792-3799.
307. Luo, X., et al., *Quantum-Cutting Luminescent Solar Concentrators Using Ytterbium-Doped Perovskite Nanocrystals.* Nano Lett., 2019. **19**: p. 338-341.
308. Cohen, T.A., et al., *Quantum-cutting Yb^{3+}-doped perovskite nanocrystals for monolithic bilayer luminescent solar concentrators.* J. Mater. Chem. A, 2019. **7**: p. 9279-9288.
309. Daniel M. Kroupa, J.Y.R., Tyler J. Milstein, Sidney E. Creutz, and Daniel R. Gamelin, *Quantum-Cutting Ytterbium-Doped $CsPb(Cl_{1-x}Br_x)_3$ Perovskite Thin Films with Photoluminescence Quantum Yields over 190%.* ACS Energy Lett., 2018. **3**: p. 2390-2395.
310. Li, X., et al., *Mechanism for the Extremely Efficient Sensitization of Yb^{3+}Luminescence in $CsPbCl_3$ Nanocrystals.* J. Phys. Chem. Lett., 2019. **10**: p. 487-492.
311. Mir, W.J., et al., *Postsynthesis Doping of Mn and Yb into $CsPbX_3$ (X = Cl, Br, or I) Perovskite Nanocrystals for Downconversion Emission.* Chem. Mater., 2018. **30**: p. 8170-8178.
312. Milstein, T.J., et al., *Anion Exchange and the Quantum-Cutting Energy Threshold in Ytterbium-Doped $CsPb(Cl_{1-x}Br_x)_3$ Perovskite Nanocrystals.* Nano Lett. , 2019. **19**: p. 1931-1937.
313. Ma, J.-P., et al., *Insights into the local structure of dopants, doping efficiency, and luminescence properties of lanthanide-doped $CsPbCl_3$ perovskite nanocrystals.* J. Mater. Chem. C, 2019. **7**: p. 3037-3048.
314. Mahor, Y., W.J. Mir, and A. Nag, *Synthesis and Near-Infrared Emission of Yb-Doped $Cs_2AgInCl_6$ Double Perovskite Microcrystals and Nanocrystals.* J. Phys. Chem. C, 2019. **123**: p. 15787-15793.
315. Erickson, C.S., et al., *Photoluminescence Saturation in Quantum-Cutting Yb^{3+}-Doped $CsPb(Cl_{1-x}Br_x)_3$ Perovskite Nanocrystals: Implications for Solar Downconversion.* J. Phys. Chem. C, 2019. **123**: p. 12474-12484.
316. Hu, Q., et al., *Rare Earth Ion-Doped $CsPbBr_3$ Nanocrystals.* Adv. Optical Mater., 2018. **6**: p. 1700864.
317. Pan, G., et al., *Doping Lanthanide into Perovskite Nanocrystals: Highly Improved and Expanded Optical Properties.* Nano Lett., 2017. **17**(12): p. 8005-8011.
318. Zheng, W., et al., *Near-infrared-triggered photon upconversion tuning in all-inorganic cesium lead halide perovskite quantum dots.* Nature Communications, 2018. **9**: p. 3462.
319. Yang, Z., et al., *Bright Blue Light-Emitting Doped Cesium Bromide Nanocrystals: Alternatives of Lead-Free Perovskite Nanocrystals for White LEDs.* Adv. Optical Mater., 2019. **7**: p. 1900108.
320. Mir, W.J., et al., *Lanthanide doping in metal halide perovskite nanocrystals: spectral shifting, quantum cutting and optoelectronic applications.* NPG Asia Materials, 2020. **12**: p. 9.
321. Son, J.-Y., et al., *Photoinduced valence transition in gold complexes $Cs_2Au_2X_6$ (X=Cl and Br) probed by x-ray photoemission spectroscopy.* Physical Review B, 2005. **72**: p. 235105.
322. Ikeda, K., et al., *P-T Phase Diagram And Gold Valence State Of New Gold Mixed-Valence Complexes, $Cs_2[Au^IX_2][Au^{III}Y_4]$(X, Y = Cl, Br, I; X = Y).* Ceramics - Silikáty, 2004. **48**(4): p. 159-164.
323. Kojima, N., *Gold Valence Transition and Phase Diagram in the Mixed-Valence Complexes, $M_2[Au^IX_2][Au^{III}X_4]$ (M = Rb, Cs; X= Cl, Br, and I).* Bull. Chem. Soc. Jpn., 2000. **73**: p. 1445-1460.

324. Balakrishnan, S.K. and P.V. Kamat, *Au-CsPbBr$_3$ Hybrid Architecture: Anchoring Gold Nanoparticles on Cubic Perovskite Nanocrystals.* ACS Energy Lett., 2017. **2**(1): p. 88-93.

325. Roman, B.J., et al., *Au Exchange or Au Deposition: Dual Reaction Pathways in Au-CsPbBr$_3$ Heterostructure Nanoparticles.* Nano Lett., 2017. **17**: p. 5561-5566.

326. Zhou, S., et al., *Ag-Doped Halide Perovskite Nanocrystals for Tunable Band Structure and Efficient Charge Transport.* ACS Energy Lett., 2019. **4**: p. 534-541.

327. Lu, M., et al., *Spontaneous Silver Doping and Surface Passivation of CsPbI$_3$ Perovskite Active Layer Enable Light-Emitting Devices with an External Quantum Efficiency of 11.2%.* ACS Energy Lett., 2018. **3**: p. 1571-1577.

328. Chen, J.-K., et al., *High-Efficiency Violet-Emitting All-Inorganic Perovskite Nanocrystals Enabled by Alkaline-Earth Metal Passivation.* Chem. Mater., 2019. **31**: p. 3974-3983.

329. Lu, M., et al., *Simultaneous Strontium Doping and Chlorine Surface Passivation Improve Luminescence Intensity and Stability of CsPbI$_3$ Nanocrystals Enabling Efficient Light-Emitting Devices.* Adv. Mater., 2018. **30**: p. 1804691.

330. Yao, J.-S., et al., *Few-Nanometer-Sized α-CsPbI$_3$ Quantum Dots Enabled by Strontium Substitution and Iodide Passivation for Efficient Red-Light Emitting Diodes.* J. Am. Chem. Soc. , 2019. **141**: p. 2069-2079.

331. Behera, R.K., et al., *Doping Smallest Shannon Radii Transition Metal Ion Ni(II) for Stabilizing α-CsPbI$_3$ Perovskite Nanocrystals.* J. Phys. Chem. Lett., 2019. **10**: p. 7916-7921.

332. Ketavath, R., et al., *Deciphering the Ultrafast Nonlinear Optical Properties and Dynamics of Pristine and Ni-Doped CsPbBr$_3$ Colloidal Two-Dimensional Nanocrystals.* J. Phys. Chem. Lett., 2019. **10**: p. 5577-5584.

333. Yong, Z.-J., et al., *Doping-Enhanced Short-Range Order of Perovskite Nanocrystals for Near-Unity Violet Luminescence Quantum Yield.* J. Am. Chem. Soc., 2018. **140**: p. 9942-9951.

334. Pan, G., et al., *Bright Blue Light Emission of Ni^{2+} ions doped CsPbCl$_x$Br$_{3-x}$ Perovskite Quantum Dots Enabling Efficient Light-Emitting Devices.* ACS Appl. Mater. Interfaces, 2020. **12**(12): p. 14195-14202.

335. De, A., et al., *Highly Luminescent Violet- and Blue-Emitting Stable Perovskite Nanocrystals.* ACS Materials Lett., 2019. **1**: p. 116-122.

336. Mondal, N., A. De, and A. Samanta, *Achieving Near-Unity Photoluminescence Efficiency for Blue-Violet-Emitting Perovskite Nanocrystals.* ACS Energy Lett., 2019. **4**: p. 32-39.

337. Bi, C., et al., *Thermally Stable Copper(II)-Doped Cesium Lead Halide Perovskite Quantum Dots with Strong Blue Emission.* J. Phys. Chem. Lett., 2019. **10**: p. 943-952.

338. Chen, Y.-C., et al., *Enhanced Luminescence and Stability of Cesium Lead Halide Perovskite CsPbX$_3$ Nanocrystals by Cu^{2+}-Assisted Anion Exchange Reactions.* J. Phys. Chem. C, 2019. **123**: p. 2353-2360.

339. Qiao, G., et al., *An efficient route to assemble novel organometal halide perovskites and emission evolution performance.* Journal of Alloys and Compounds, 2019. **771**: p. 418-423.

340. Shen, X., et al., *Zn-Alloyed CsPbI$_3$ Nanocrystals for Highly Efficient Perovskite Light-Emitting Devices.* Nano Lett., 2019. **19**: p. 1552-1559.

341. Ding, H., et al., *Transition metal halide-doped, highly stable all-inorganic perovskite nanocrystals for fabrication of white light-emitting diodes.* J. Mater. Chem. C, 2019. **7**: p. 1690-1695.

342. Shen, Z., et al., *The luminescence properties of CsPb$_x$M$_{1-x}$Br$_3$ perovskite nanocrystals transformed from Cs$_4$PbBr$_6$ mediated by various divalent bromide MBr$_2$ salts.* Nanoscale, 2019. **11**: p. 4008-4014.

343. Akkerman, Q.A., et al., *Nearly Monodisperse Insulator Cs_4PbX_6 (X = Cl, Br, I) Nanocrystals, Their Mixed Halide Compositions, and Their Transformation into $CsPbX_3$ Nanocrystals.* Nano Lett. , 2017. **17**: p. 1924-1930.
344. Begum, R., et al., *Engineering Interfacial Charge Transfer in $CsPbBr_3$ Perovskite Nanocrystals by Heterovalent Doping.* J. Am. Chem. Soc., 2017. **139**: p. 731-737.
345. Miao, X., et al., *Air-stable $CsPb_{1-x}Bi_xBr_3$ (0 < x << 1) perovskite crystals: optoelectronic and photostriction properties.* J. Mater. Chem. C, 2017. **5**: p. 4931-4939.
346. Abdelhady, A.L., et al., *Heterovalent Dopant Incorporation for Bandgap and Type Engineering of Perovskite Crystals.* J. Phys. Chem. Lett., 2016. **7**: p. 295-301.
347. Zhang, Z., et al., *Bandgap Narrowing in Bi-Doped $CH_3NH_3PbCl_3$ Perovskite Single Crystals and Thin Films.* J. Phys. Chem. C, 2017. **121**: p. 17436-17441.
348. Nayak, P.K., et al., *Impact of Bi^{3+} Heterovalent Doping in Organic-Inorganic Metal Halide Perovskite Crystals.* J. Am. Chem. Soc. , 2018. **140**: p. 574-577.
349. Yin, J., et al., *Unlocking the Effect of Trivalent Metal Doping in All-Inorganic $CsPbBr_3$ Perovskite.* ACS Energy Lett., 2019. **4**: p. 789-795.
350. Zhang, X., et al., *Strong Blue Emission from Sb^{3+}-Doped Super Small $CsPbBr_3$ Nanocrystals.* J. Phys. Chem. Lett., 2019. **10**: p. 1750-1756.
351. Liu, M., et al., *Aluminum-Doped Cesium Lead Bromide Perovskite Nanocrystals with Stable Blue Photoluminescence Used for Display Backlight.* Adv.Sci., 2017. **4**: p. 1700335.
352. Dong, X., et al., *Trivalent ion mediated abnormal growth of allinorganic perovskite nanocrystals and their divergent emission properties.* Nanoscale, 2019. **11**: p. 7903-7912.
353. Rana, P.J.S., et al., *Energy Transfer Dynamics of Highly Stable Fe^{3+} Doped $CsPbCl_3$ Perovskite Nanocrystals with Dual-Color Emission.* J. Phys. Chem. C, 2019. **123**: p. 17026-17034.
354. Guvenc, C.M., et al., *Gd^{3+}-Doped α-$CsPbI_3$ Nanocrystals with Better Phase Stability and Optical Properties.* J. Phys. Chem. C, 2019. **123**: p. 24865-24872.
355. Leng, M., et al., *Lead-Free, Blue Emitting Bismuth Halide Perovskite Quantum Dots.* Angew. Chem. Int. Ed. , 2016. **55**: p. 15012-15016.
356. Zhang, J., et al., *High Quantum Yield Blue Emission from Lead-Free Inorganic Antimony Halide Perovskite Colloidal Quantum Dots.* ACS Nano, 2017. **11**: p. 9294-9302.
357. Creutz, S.E., et al., *Colloidal Nanocrystals of Lead-Free Double-Perovskite (Elpasolite) Semiconductors: Synthesis and Anion Exchange To Access New Materials.* Nano Lett., 2018. **18**: p. 1118-1123.
358. Bekenstein, Y., et al., *The Making and Breaking of Lead-Free Double Perovskite Nanocrystals of Cesium Silver-Bismuth Halide Compositions.* Nano Lett., 2018. **18**: p. 3502-3508.
359. Volonakis, G., et al., *$Cs_2InAgCl_6$: A New Lead-Free Halide Double Perovskite with Direct Band Gap.* J. Phys. Chem. Lett. , 2017: p. 772-778.
360. Lee, W., S. Hong, and S. Kim, *Colloidal Synthesis of Lead-Free Silver-Indium Double-Perovskite $Cs_2AgInCl_6$ Nanocrystals and Their Doping with Lanthanide Ions.* J. Phys. Chem. C, 2019. **123**: p. 2665-2672.
361. Luo, J., et al., *Efficient and stable emission of warm-white light from lead-free halide double perovskites.* Nature, 2018. **563**: p. 541–545.
362. Li, X., et al., *$CsPbX_3$ Quantum Dots for Lighting and Displays: Room-Temperature Synthesis, Photoluminescence Superiorities, Underlying Origins and White Light-Emitting Diodes.* Adv. Funct. Mater., 2016. **26**: p. 2435-2445.
363. Lou, Y., et al., *Formation of highly luminescent cesium bismuth halide perovskite quantum dots tuned by anion exchange.* Chem. Commun., 2018. **54**: p. 3779-3782.

364. Leng, M., et al., *Surface Passivation of Bismuth-Based Perovskite Variant Quantum Dots To Achieve Efficient Blue Emission.* Nano Lett. , 2018. **18**: p. 6076-6083.
365. Yang, B., et al., *Lead-Free, Air-Stable All-Inorganic Cesium Bismuth Halide Perovskite Nanocrystals.* Angew. Chem. Int. Ed., 2017. **56**: p. 12471-12475.
366. Zhang, Y., et al., *Direct-Indirect Nature of the Bandgap in Lead-Free Perovskite Nanocrystals.* J. Phys. Chem. Lett. , 2017. **8**: p. 3173-3177.
367. Pal, J., et al., *Synthesis and Optical Properties of Colloidal $M_3Bi_2I_9$ (M = Cs, Rb) Perovskite Nanocrystals.* J. Phys. Chem. C, 2018. **122**: p. 10643-10649.
368. Volonakis, G., et al., *Lead-Free Halide Double Perovskites via Heterovalent Substitution of Noble Metals.* J. Phys. Chem. Lett., 2016. **7**: p. 1254-1259.
369. Ravi, V.K., N. Singhal, and A. Nag, *Initiation and future prospects of colloidal metal halide double-perovskite nanocrystals: Cs_2AgBiX_6 (X = Cl, Br, I).* J. Mater. Chem. A, 2018. **6**: p. 21666-21675.
370. Han, P., et al., *Lead-Free Sodium-Indium Double Perovskite Nanocrystals through Doping Silver Cations for Bright Yellow Emission.* Angew. Chem. Int. Ed., 2019. **58**: p. 17231-17235.
371. Lamba, R.S., et al., *Band Gap Engineering in $Cs_2(Na_xAg_{1-x})BiCl_6$ Double Perovskite Nanocrystals.* J. Phys. Chem. Lett., 2019. **10**: p. 5173-5181.
372. Locardi, F., et al., *Emissive Bi-Doped Double Perovskite $Cs_2Ag_{1-x}Na_xInCl_6$ Nanocrystals.* ACS Energy Lett., 2019. **4**: p. 1976-1982.
373. Hu, Q., et al., *Tunable Color Temperatures and Efficient White Emission from $Cs_2Ag_{1-x}Na_xIn_{1-y}Bi_yCl_6$ Double Perovskite Nanocrystals.* Small, 2019. **15**: p. 1903496.
374. Xiao, Z., et al., *Intrinsic Instability of $Cs_2In(I)M(III)X_6$ (M = Bi, Sb; X = Halogen) Double Perovskites: A Combined Density Functional Theory and Experimental Study.* J. Am. Chem. Soc., 2017. **139**: p. 6054-6057.
375. Yang, B., et al., *Lead-Free Silver-Bismuth Halide Double Perovskite Nanocrystals.* Angew. Chem. Int. Ed., 2018. **57**: p. 5359-5363.
376. Shai, X., et al., *Efficient planar perovskite solar cells using halide Sr-substituted Pb perovskite.* Nano Energy, 2017. **36**: p. 213-222.
377. Phung, N., et al., *The doping mechanism of halide perovskite unveiled by alkaline earth metals.* J. Am. Chem. Soc., 2020. **142**(5): p. 2364-2374.
378. Zou, S., et al., *Stabilizing Cesium Lead Halide Perovskite Lattice through Mn(II) Substitution for Air-Stable Light-Emitting Diodes.* J. Am. Chem. Soc. , 2017. **139**: p. 11443-11450.
379. Sichert, J.A., et al., *Quantum Size Effect in Organometal Halide Perovskite Nanoplatelets.* Nano Lett. , 2015. **15**: p. 6521-6527.
380. Butkus, J., et al., *The Evolution of Quantum Confinement in $CsPbBr_3$ Perovskite Nanocrystals.* Chem. Mater. , 2017. **29**: p. 3644-3652.
381. Levchuk, I., et al., *Ligand-assisted thickness tailoring of highly luminescent colloidal $CH_3NH_3PbX_3$ (X = Br and I) perovskite nanoplatelets.* Chem. Commun., 2017. **53**: p. 244-247.
382. Kumar, S., et al., *Efficient Blue Electroluminescence Using Quantum-Confined Two-Dimensional Perovskites.* ACS Nano, 2016. **10**: p. 9720-9729.
383. Huang, J., et al., *Control of oleylamine to perovskite ratio in synthesis of $MAPbBr_3$ nanoparticles.* Chemical Physics Letters, 2018. **702**: p. 21-25.
384. Dutta, A., et al., *Tuning the Size of $CsPbBr_3$ Nanocrystals: All at One Constant Temperature.* ACS Energy Lett. , 2018. **3**: p. 329-334.
385. Dong, Y., et al., *Precise Control of Quantum Confinement in Cesium Lead Halide Perovskite Quantum Dots via Thermodynamic Equilibrium.* Nano Lett., 2018. **18**: p. 3716-3722.

386. Akkerman, Q.A., et al., *Tuning the Optical Properties of Cesium Lead Halide Perovskite Nanocrystals by Anion Exchange Reactions.* J. Am. Chem. Soc., 2015. **137**: p. 10276-10281.
387. Nedelcu, G., et al., *Fast Anion-Exchange in Highly Luminescent Nanocrystals of Cesium Lead Halide Perovskites ($CsPbX_3$, X = Cl, Br, I).* Nano Lett., 2015. **15**(8): p. 5635-5640.
388. Li, M., et al., *Phase transformation, morphology control, and luminescence evolution of cesium lead halide nanocrystals in the anion exchange process.* RSC Adv., 2016. **6**: p. 103382-103389
389. Chiba, T., et al., *Anion-exchange red perovskite quantum dots with ammonium iodine salts for highly efficient light-emitting devices.* Nature Photonics, 2018. **12**: p. 681-687.
390. Zhang, D., et al., *Synthesis of Composition Tunable and Highly Luminescent Cesium Lead Halide Nanowires through Anion-Exchange Reactions.* J. Am. Chem. Soc., 2016. **138**: p. 7236-7239.
391. Dou, L., et al., *Spatially resolved multicolor $CsPbX_3$ nanowire heterojunctions via anion exchange.* PNAS, 2017. **114**(28): p. 7216-7221.
392. Koscher, B.A., et al., *Surface- vs Diffusion-Limited Mechanisms of Anion Exchange in $CsPbBr_3$ Nanocrystal Cubes Revealed through Kinetic Studies.* J. Am. Chem. Soc., 2016. **138**: p. 12065-12068.
393. Cottingham, P. and R.L. Brutchey, *Compositionally Dependent Phase Identity of Colloidal $CsPbBr_{3-x}I_x$ Quantum Dots.* Chem. Mater., 2016. **28**(21): p. 7574-7577.
394. Butler, K.T., J.M. Frost, and A. Walsh, *Band alignment of the hybrid halide perovskites $CH_3NH_3PbCl_3$, $CH_3NH_3PbBr_3$ and $CH_3NH_3PbI_3$.* Mater. Horiz., 2015. **2**: p. 228-231.
395. Wang, B., X. Xiao, and T. Chen, *Perovskite photovoltaics: a high-efficiency newcomer to the solar cell family.* Nanoscale, 2014. **6**: p. 12287-12297.
396. Guhrenz, C., et al., *Solid-State Anion Exchange Reactions for Color Tuning of $CsPbX_3$ Perovskite Nanocrystals.* Chem. Mater. , 2016. **28**: p. 9033-9040.
397. Parobek, D., et al., *Photoinduced Anion Exchange in Cesium Lead Halide Perovskite Nanocrystals.* J. Am. Chem. Soc., 2017. **139**: p. 4358-4361.
398. Jiang, Q., et al., *Pseudohalide-Induced Moisture Tolerance in Perovskite $CH_3NH_3Pb(SCN)_2I$ Thin Films.* Angew. Chem. Int. Ed. , 2015. **54**: p. 7617-7620.
399. Chen, Y., et al., *Efficient and reproducible $CH_3NH_3PbI_{3-x}(SCN)_x$ perovskite based planar solar cells.* Chem. Commun., 2015. **51**: p. 11997-11999.
400. Tai, Q., et al., *Efficient and stable perovskite solar cells prepared in ambient air irrespective of the humidity.* Nature Communications, 2016. **7**: p. 11105.
401. Liu, J., et al., *Molecular design and photovoltaic performance of a novel thiocyanate-based layered organometal perovskite material.* Synthetic Metals, 2016. **215**: p. 56-63.
402. Ke, W., et al., *Employing Lead Thiocyanate Additive to Reduce the Hysteresis and Boost the Fill Factor of Planar Perovskite Solar Cells.* Adv. Mater., 2016. **28**: p. 5214-5221.
403. Halder, A., et al., *Pseudohalide (SCN-)-Doped $MAPbI_3$ Perovskites: A Few Surprises.* J. Phys. Chem. Lett. , 2015. **6**: p. 3483-3489.
404. Daub, M. and H. Hillebrecht, *Synthesis, Single-Crystal Structure and Characterization of $(CH_3NH_3)_2Pb(SCN)_2I_2$.* Angew. Chem. Int. Ed. , 2015. **54**: p. 11016-11017.
405. Ganose, A.M., C.N. Savory, and D.O. Scanlon, *$(CH_3NH_3)_2Pb(SCN)_2I_2$: A More Stable Structural Motif for Hybrid Halide Photovoltaics?* J. Phys. Chem. Lett., 2015. **6**: p. 4594-4598.
406. Umeyama, D., Y. Lin, and H.I. Karunadasa, *Red-to-Black Piezochromism in a Compressible Pb-I-SCN Layered Perovskite.* Chem. Mater., 2016. **28**: p. 3241-3244.

407. Numata, Y., et al., *Thiocyanate Containing Two-Dimensional Cesium Lead Iodide Perovskite, $Cs_2PbI_2(SCN)_2$: Characterization, Photovoltaic Application, and Degradation Mechanism.* ACS Appl. Mater. Interfaces, 2018. **10**: p. 42363-42371.
408. Nie, R., et al., *Mixed Sulfur and Iodide-Based Lead-Free Perovskite Solar Cells.* J. Am. Chem. Soc. , 2018. **140**: p. 872-875.
409. Zhang, C., et al., *Development of a Novel Mixed Sulfide-Iodide Lead-Free Bismuth Perovskite.* SPIE Proceedings, Physical Chemistry of Semiconductor Materials and Interfaces XVII. **10724**(107240A): p. https://doi.org/10.1117/12.2502721.
410. Sun, Y.-Y., et al., *Discovering lead-free perovskite solar materials with a split-anion approach.* Nanoscale, 2016. **8**: p. 6284-6289.
411. Hong, F., et al., *Viability of Lead-Free Perovskites with Mixed Chalcogen and Halogen Anions for Photovoltaic Applications.* J. Phys. Chem. C, 2016. **120**: p. 6435-6441.
412. Dong, H., et al., *Materials chemistry and engineering in metal halide perovskite lasers.* Chem. Soc. Rev., 2020. **49**: p. 951-982.
413. Brenner, P., et al., *Continuous wave amplified spontaneous emission in phase-stable lead halide perovskites.* Nat. Commun., 2019. **10**: p. 988-994.
414. Tang, B., et al., *Single-Mode Lasers Based on Cesium Lead Halide Perovskite Submicron Spheres.* ACS Nano, 2017. **11**: p. 10681-10688.
415. Boyd, C.C., et al., *Understanding Degradation Mechanisms and Improving Stability of Perovskite Photovoltaics.* Chem. Rev., 2019. **119**(5): p. 3418-3451.
416. Jena, A.K., A. Kulkarni, and T. Miyasaka, *Halide Perovskite Photovoltaics: Background, Status, and Future Prospects.* Chem. Rev., 2019. **119**(5): p. 3036-3103.
417. Hazarika, A., et al., *Perovskite Quantum Dot Photovoltaic Materials beyond the Reach of Thin Films: Full-Range Tuning of A-Site Cation Composition.* ACS Nano, 2018. **12**(10): p. 10327-10337.
418. Liu, F., et al., *GeI_2 Additive for High Optoelectronic Quality $CsPbI_3$ Quantum Dots and Their Application in Photovoltaic Devices.* Chem. Mater., 2019. **31**: p. 798-807.
419. Chen, D., et al., *Full-Spectral Fine-Tuning Visible Emissions from Cation Hybrid $Cs_{1-m}FA_mPbX_3$ (X = Cl, Br, and I, $0 \le m \le 1$) Quantum Dots.* ACS Appl. Mater. Interfaces, 2017. **9**: p. 20671-20678.
420. Ghosh, J., M. Hossain, and P.K. Giri, *Origin and Tunability of Dual Color Emission in Highly Stable Mn Doped $CsPbCl_3$ Nanocrystals Grown by a Solid-State Process.* J. Colloid Interf. Sci., 2020. **564**: p. 357-370.
421. Li, F., et al., *High Br- Content $CsPb(Cl_yBr_{1-y})_3$ Perovskite Nanocrystals with Strong Mn^{2+} Emission through Diverse Cation/Anion Exchange Engineering.* ACS Appl. Mater. Interfaces, 2018. **10**: p. 11739-11746.
422. Li, L., et al., *Interfacial electronic structures of MoO_x/mixed perovskite photodetector.* Organic Electronics, 2019. **65**: p. 162-169.
423. Seth, S., et al., *Tackling the Defects, Stability, and Photoluminescence of $CsPbX_3$ Perovskite Nanocrystals.* ACS Energy Lett., 2019. **4**: p. 1610-1618.
424. Sun, J., et al., *Lead-Free Perovskite Nanocrystals for Light-Emitting Devices.* J. Phys. Chem. Lett., 2018. **9**: p. 1573-1583.
425. Kubicki, D.J., et al., *Phase Segregation in Cs-, Rb- and K-Doped Mixed-Cation $(MA)_x(FA)_{1-x}PbI_3$ Hybrid Perovskites from Solid-State NMR.* J. Am. Chem. Soc., 2017. **139**: p. 14173-14180.
426. Brennan, M.C., et al., *Origin of the Size-Dependent Stokes Shift in $CsPbBr_3$ Perovskite Nanocrystals.* Am. Chem. Soc., 2017. **139**(35): p. 12201-12208.

427. Jung, J., et al., *Crafting Core/Graded Shell-Shell Quantum Dots with Suppressed Re-absorption and Tunable Stokes Shift as High Optical Gain Materials.* Angew. Chem. Int. Ed., 2016. **55**: p. 5071-5075.
428. Lou, S., T. Xuan, and J. Wang, *(INVITED) Stability: A desiderated problem for the lead halide perovskites.* Optical Materials: X, 2019. **1**: p. 100023.
429. Liu, M., et al., *Advances in the Stability of Halide Perovskite Nanocrystals.* Materials, 2019. **12**: p. 3733.
430. Lv, W., et al., *Improving the Stability of Metal Halide Perovskite Quantum Dots by Encapsulation.* Adv. Mater., 2019. **31**: p. 1900682.
431. Pan, J., et al., *Bidentate Ligand-Passivated $CsPbI_3$ Perovskite Nanocrystals for Stable Near-Unity Photoluminescence Quantum Yield and Efficient Red Light-Emitting Diodes.* J. Am. Chem. Soc., 2018. **140**: p. 562-565.
432. Dutta, A., et al., *Near-Unity Photoluminescence Quantum Efficiency for All $CsPbX_3$ (X=Cl, Br, and I) Perovskite Nanocrystals: A Generic Synthesis Approach.* Angew. Chem. Int. Ed., 2019. **58**: p. 5552-5556.
433. Behera, R.K., et al., *Blue-Emitting $CsPbCl_3$ Nanocrystals: Impact of Surface Passivation for Unprecedented Enhancement and Loss of Optical Emission.* J. Phys. Chem. Lett., 2018. **9**: p. 6884-6891.
434. Almeida, G., I. Infante, and L. Manna, *Resurfacing halide perovskite nanocrystals.* Science 2019. **364**(6443): p. 833-834.
435. Tong, J., et al., *Direct Hot-Injection Synthesis of Lead Halide Perovskite Nanocubes in Acrylic Monomers for Ultrastable and Bright Nanocrystal-Polymer Composite Films.* ACS Appl. Mater. Interfaces, 2019. **11**: p. 9317-9325.
436. Eperon, G.E., et al., *Perovskite-perovskite tandem photovoltaics with optimized band gaps.* Science, 2016. **354**(6314): p. 861-865.
437. Yang, Z., et al., *Stable Low-Bandgap Pb-Sn Binary Perovskites for Tandem Solar Cells.* Adv. Mater., 2016. **28**: p. 8990-8997.
438. Liao, W., et al., *Fabrication of Efficient Low-Bandgap Perovskite Solar Cells by Combining Formamidinium Tin Iodide with Methylammonium Lead Iodide.* J. Am. Chem. Soc., 2016. **138**: p. 12360-12363.
439. Wang, Z., et al., *Efficient and Air-Stable Mixed-Cation Lead Mixed-Halide Perovskite Solar Cells with n-Doped Organic Electron Extraction Layers.* Adv. Mater., 2017. **29**: p. 1604186.
440. Jeon, N.J., et al., *Compositional engineering of perovskite materials for high-performance solar cells.* Nature, 2015. **517**: p. 476-480.
441. Yang, W.S., et al., *High-performance photovoltaic perovskite layers fabricated through intramolecular exchange.* Science, 2015. **348**(6240): p. 1234-1237.
442. Jiang, Q., et al., *Enhanced electron extraction using SnO_2 for high-efficiency planar-structure $HC(NH_2)_2PbI_3$-based perovskite solar cells.* Nature Energy, 2016. **2**: p. 16177.
443. Yang, Z., et al., *Stabilized Wide Bandgap Perovskite Solar Cells by Tin Substitution.* Nano Lett., 2016. **16**: p. 7739-7747.
444. Zuo, F., et al., *Binary-Metal Perovskites Toward High-Performance Planar-Heterojunction Hybrid Solar Cells.* Adv. Mater. , 2014. **26**: p. 6454-6460.
445. Muscarella, L.A., et al., *Air-Stable and Oriented Mixed Lead Halide Perovskite (FA/MA) by the One-Step Deposition Method Using Zinc Iodide and an Alkylammonium Additive.* ACS Appl. Mater. Interfaces, 2019. **11**: p. 17555-17562.
446. Saliba, M., et al., *Cesium-containing triple cation perovskite solar cells: improved stability, reproducibility and high efficiency.* Energy Environ. Sci., 2016. **9**: p. 1989-1997.

447. Albadri, A., et al., *Unraveling the Impact of Rubidium Incorporation on the Transport-Recombination Mechanisms in Highly Efficient Perovskite Solar Cells by Small-Perturbation Techniques.* J. Phys. Chem. C, 2017. **121**: p. 24903-24908.
448. Yadav, P., et al., *The Role of Rubidium in Multiple-Cation-Based High-Efficiency Perovskite Solar Cells.* Adv. Mater. , 2017. **29**: p. 1701077.
449. Tang, Z., et al., *Hysteresis-free perovskite solar cells made of potassium-doped organometal halide perovskite.* Scientific Reports, 2017. **7**: p. 12183.
450. Bu, T., et al., *A novel quadruple-cation absorber for universal hysteresis elimination for high efficiency and stable perovskite solar cells.* Energy Environ. Sci., 2017. **10**: p. 2509-2515.
451. Wang, Z., et al., *Efficient ambient-air-stable solar cells with 2D-3D heterostructured butylammonium-caesium-formamidinium lead halide perovskites.* Nature Energy, 2017. **2**: p. 17135.
452. Pering, S.R., et al., *Azetidinium lead iodide for perovskite solar cells.* J. Mater. Chem. A, 2017. **5**: p. 20658-20665.
453. Chen, Z., et al., *Methylammonium, formamidinium and ethylenediamine mixed triple-cation perovskite solar cells with high efficiency and remarkable stability.* J. Mater. Chem. A, 2018. **6**: p. 17625-17632.
454. Jodlowski, A.D., et al., *Large guanidinium cation mixed with methylammonium in lead iodide perovskites for 19% efficient solar cells.* Nature Energy, 2017. **2**: p. 972-979.
455. Hamaguchi, R., et al., *Formamidine and cesium-based quasi-twodimensional perovskites as photovoltaic absorbers.* Chem. Commun., 2017. **53**: p. 4366-4369.
456. Jiang, X., et al., *Ultra-high open-circuit voltage of tin perovskite solar cells via an electron transporting layer design.* Nature Communications, 2020. **11**: p. 1245.
457. Patil, J.V., S.S. Mali, and C.K. Hong, *A thiourea additive-based quadruple cation lead halide perovskite with an ultra-large grain size for efficient perovskite solar cells.* Nanoscale, 2019. **11**: p. 21824-21833.
458. Yang, F., et al., *Addition Effect of Pyreneammonium Iodide to Methylammonium Lead Halide Perovskite-2D/3D Heterostructured Perovskite with Enhanced Stability.* Adv. Funct. Mater., 2018. **28**: p. 1804856.
459. Passarelli, J.V., et al., *Enhanced Out-of-Plane Conductivity and Photovoltaic Performance in n = 1 Layered Perovskites through Organic Cation Design.* J. Am. Chem. Soc. , 2018. **140**: p. 7313-7323.
460. Garcı´a-Espejo, G., et al., *Mechanochemical synthesis of one-dimensional (1D) hybrid perovskites incorporating polycyclic aromatic spacers: highly fluorescent cation-based materials.* J. Mater. Chem. C, 2018. **6**: p. 7677-7682.
461. Koscher, B.A., et al., *Essentially Trap-Free $CsPbBr_3$ Colloidal Nanocrystals by Postsynthetic Thiocyanate Surface Treatment.* J. Am. Chem. Soc., 2017. **139**: p. 6566-6569.
462. Yang, M., et al., *Energy Transport in $CsPbBr_3$ Perovskite Nanocrystal Solids.* ACS Photonics, 2019: p. https://dx.doi.org/10.1021/acsphotonics.9b01316.
463. Ding, R., X. Zhang, and X.W. Sun, *Organometal Trihalide Perovskites with Intriguing Ferroelectric and Piezoelectric Properties.* Adv. Funct. Mater., 2017. **27**: p. 1702207.
464. DiMaio, J.R., et al., *Controlling energy transfer between multiple dopants within a single nanoparticle.* PNAS, 2008. **105**(6): p. 1809-1813.
465. Su, H., et al., *Janus particles: design, preparation, and biomedical applications.* Materials Today Bio, 2019. **4**: p. 100033.

Table of Contents (TOC) Graphic

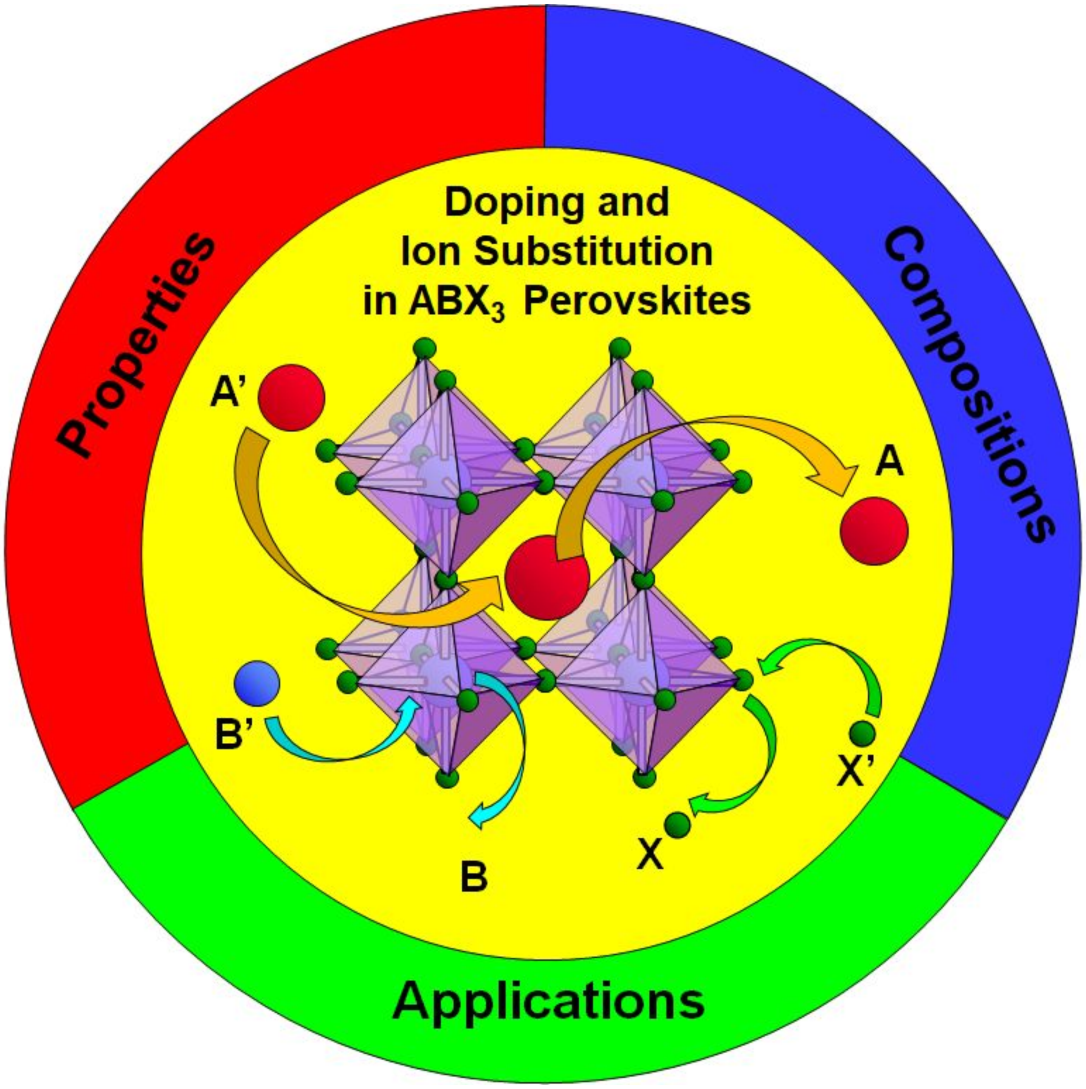

The effects of doping and ion substitution in colloidal metal halide perovskite nanocrystals on their compositions, properties, and applications.